ABSTRACT

Title of dissertation: MAJORANA ZERO MODES IN
SOLID STATE SYSTEMS

Hoi Yin Hui, Doctor of Philosophy, 2015

Dissertation directed by: Professor Sankar Das Sarma
Department of Physics

Majorana zero modes are zero-energy excitations that are their own anti-particles, and obey non-Abelian statistics which could be harnessed for topological quantum computation. There are many theoretical proposals to realize them in solid state systems, but experimental realizations are confronted by a number of non-idealities. In this thesis, we theoretically investigate such complications, thereby suggesting improvement and directions that could be pursued. We first develop a theoretical framework to analyze the effect of ensemble-averaged disorder on the Majorana zero modes, generalizing the Eilenberger theory to handle 1D systems while retaining short-distance fluctuations. We then consider disordered topological insulator-based heterostructures, showing that extra subgap states are potentially induced, obscuring the density-of-states signature of the Majorana zero mode. We also analyze in depth the experimentally observed soft gap feature, suggesting that a cleaner interface in the semiconductor-based proposal can harden the gap.

In view of some of the limitations of the proposals based on semiconductors or topological insulators, we look into a new class of systems in which a ferromagnetic atomic chain is put on the surface of a bulk spin-orbit-coupled superconductor. This system is analyzed in two limits, corresponding to weak or strong inter-atomic hop-

ping on the chain. In each of these cases, the topological criteria are obtained. We also find that in the limit of strong chain-superconductor coupling, the length scales of the effective Hamiltonian of the chain are significantly suppressed, potentially explaining some of the recent observations in experiments.

MAJORANA ZERO MODES IN SOLID STATE SYSTEMS

by

Hoi Yin Hui

Dissertation submitted to the Faculty of the Graduate School of the
University of Maryland, College Park in partial fulfillment
of the requirements for the degree of
Doctor of Philosophy
2015

Advisory Committee:
Professor Sankar Das Sarma, Chair/Advisor
Assistant Professor Jay Deep Sau
Professor James Robert Anderson
Professor Theodore L. Einstein
Professor Christopher Jarzynski

Acknowledgments

During my five years of being a research assistant in the Condensed Matter Theory Center, I had the honor to work with many collaborators, from whom I benefited a lot. First and foremost, I would like to thank my advisor, Professor Sankar Das Sarma, for his support and guidance of my research. I must also thank Jay Sau and Ryan Barnett, who were former postdoctoral researchers in my research group and both are now faculty members. I am indebted to their patience and kindness during my incipient stage of research, which had helped me get started in their fields. They have all provided valuable advice on my studies and my job application.

I benefited a lot from the discussion with and courses offered by other faculty members in this university, including but not limited to Professor Victor Galitski, Professor Michael Levin, Professor Christopher Jarzynski and Professor James Porto. I would also like to thank my dissertation committee. The time and effort they spent into reading and commenting on this thesis has greatly improved its quality.

This thesis would not have been possible without the support from the NSF-funded Physics Frontier Center at the Joint Quantum Institute (PFC@JQI). In particular, I would like to thank Professor Luis Orozco and Professor William Philips who have supported my research activities through PFC@JQI.

I have enjoyed my experience of collaboration with many other postdoctoral researchers, including Rajdeep Sensarma, So Takei, Benjamin Fregoso, Alejandro

Table of Contents

List of Figures

List of Abbreviations

MZM	Majorana Zero Mode
nD	n-dimension(al)
ZB(C)P	Zero-Bias (Conductance) Peak
SMC	Semiconductor
TI	Topological Insulator
FI	Ferromagnetic Insulator
SC	Superconductor / Superconductivity
SOC	Spin-orbit coupling / Spin-orbit-coupled
LDOS	Local Density of States
STM	Scanning Tunneling Microscope
SCBA	Self-Consistent Born Approximation
TRS	Time-reversal symmetry / Time-reversal-symmetric
BdG	Bogoliubov de-Gennes

Chapter 1

Introduction

The theoretical endeavor to realize non-Abelian Majorana zero modes (MZMs) in solid state systems has a long history of nearly two decades, with the earlier works focusing on fractional quantum Hall states [1, 2] and p-wave superconductors [3, 4]. However, experimental progress on such exotic systems has been quite slow, partly due to the stringent experimental conditions required. The recent development of topological superconductivity involving only conventional s-wave superconductors, culminating in the nanowire proposal [5, 6], was therefore a welcome surprise: for the first time, we saw the hope of generating MZM using only conventional super-conductivity, spin-orbit coupling (SOC), and Zeeman terms.

The experimental implementation of this proposal, however, was not without obstacles. The price we pay for avoiding the use of fractional quantum Hall states and p-wave superconductors was the need to interface multiple materials, like su-perconductors (SCs), semiconductors (SMCs) and even topological insulators (TIs). The quality of each of these materials, and of the interfaces between them, both play a role in the quality of the MZM thus obtained. The initial implementations of the proposal [7], while being very encouraging as signatures of MZMs were found, all suffered from non-idealities in the experiments that prevented the generation of pris-

tine MZMs. It is therefore important to understand the origin of these non-idealities so that further experiments could be improved.

This thesis is an attempt to develop such an understanding. Specifically, we shall try to:

1. Develop a theoretical understanding of realistic experiments on MZMs, and

2. Explore a new alternative platform for realizing MZMs.

We now start with the background of the subject. In the first section of this chapter, the definition of MZMs is given, and the importance of their non-Abelian statistics is stressed. We then review the minimal models that host MZMs – the chiral topological superconductors. Since these unconventional superconductors are hard to find in nature, we next discuss the recently proposed heterostructures which can also realize MZMs. While the constituent materials are not uncommon, the fabrication of the heterostructures pose unique problems, which we shall briefly discuss.

1.1 Majorana Zero Modes and their Importance

The name "Majorana" originated from particle physics. In 1937, Ettore Majorana [8] found a real solution to Dirac equation, which represents Fermionic particles that are their own antiparticles. In operator languages, the annihilation operator γ of the Majorana Fermion satisfies

$$\{\gamma_i, \gamma_j\} = 2\delta_{ij}, \gamma_i^\dagger = \gamma_i, \tag{1.1}$$

where $\{\ldots,\ldots\}$ is the anticommutator. This is quite unusual as the self-conjugacy condition is normally only satisfied by Bosonic particles like photons and π^0-mesons. Neutrinos have been proposed to satisfy (1.1) but controversy remains.

The connection of our MZMs to the Majorana Fermions in particle physics ends at (1.1). In addition to them we further require the MZMs to commute with the Hamiltonian H:

$$[H, \gamma_i] = 0, \tag{1.2}$$

where $[\ldots,\ldots]$ is the commutator. This relation indicates that MZMs lead to ground state degeneracies, as (1.2) implies that the ground state $|\mathrm{GS}\rangle$ and the excited states $\gamma_i |\mathrm{GS}\rangle$ have the same energy.

To see the exact degree of ground state degeneracy in a system with $2N$ MZMs $\gamma_1, \gamma_2, \ldots, \gamma_{2N}$ [all satisfying (1.1) and (1.2)], we observe that the operators constructed from them by

$$a_i = \frac{1}{2}\left(\gamma_{2i-1} + i\gamma_{2i}\right) \tag{1.3}$$

are regular Fermionic operators which satisfy

$$\left\{a_i, a_j^\dagger\right\} = \delta_{ij} \tag{1.4}$$

$$\{a_i, a_j\} = 0. \tag{1.5}$$

Therefore, the number operators $a_i^\dagger a_i = \frac{1}{2}\left(i\gamma_{2i-1}\gamma_{2i} + 1\right)$ are allowed to take on the values 0 or 1 in the system, and the system has 2^N degenerate ground states. There is however a superselection rule that the total Fermion parity of an isolated system

must be conserved, and the matrix elements of any physical operators between states with opposite superselection sectors must vanish. The ground state degeneracy *accessible* by any operations (e.g., braiding) within a system with $2N$ MZMs is therefore 2^{N-1}, and they are labeled by the eigenvalues ± 1 of the operators $i\gamma_{2i-1}\gamma_{2i}$.

We now discuss the braiding property of *localized* MZMs. Consider $2N$ MZMs localized at different positions $\{x_i\}_{i=1}^N$. When we exchange the positions of γ_1 and γ_2 while maintaining the locations of other MZMs, an opposite sign is picked up by γ_1 and γ_2:

$$\gamma_1 \to \gamma_2 \quad , \quad \gamma_2 \to -\gamma_1, \tag{1.6}$$

such that the quantum number $i\gamma_1\gamma_2$ is unchanged after this relabeling. Note that there could be an overall sign in (1.6), which is just a gauge choice. This transformation is effected by the unitary operator $U_{12} = \frac{e^{i\theta}}{\sqrt{2}}(1 + \gamma_2\gamma_1) = e^{i\theta}e^{\frac{\pi}{4}\gamma_2\gamma_1}$, such that

$$U_{12}\gamma_1 U_{12}^\dagger = \gamma_2, \ U_{12}\gamma_2 U_{12}^\dagger = -\gamma_1. \tag{1.7}$$

With the rule (1.6), one can prove directly that braiding MZMs in a system with four MZMs results in a non-Abelian transformation in the degenerate ground

state, given as [9]

$$U_{12} \left| 00 \right\rangle \;=\; \frac{1}{\sqrt{2}} \left(1 + i \right) \left| 00 \right\rangle \tag{1.8}$$

$$U_{23} \left| 00 \right\rangle \;=\; \frac{1}{\sqrt{2}} \left(\left| 00 \right\rangle + i \left| 11 \right\rangle \right) \tag{1.9}$$

$$U_{34} \left| 00 \right\rangle \;=\; \frac{1}{\sqrt{2}} \left(1 + i \right) \left| 00 \right\rangle \tag{1.10}$$

where U_{ij} describes the process where i^{th} and j^{th} MZMs are interchanged. This transformation is *topological*, since it only depends on the topology of the braiding operations performed. If all excited states above the degenerate ground states have energy greater than Δ, then (1.2) and hence (1.6) and (1.8)-(1.10) is ensured if the strength of perturbation is less than Δ and terms like $i\gamma_i\gamma_j$ are absent. But these can always be avoided by separating MZMs far enough, since physical Hamiltonians always act locally. These underlie the topological protection of the system.

Although braiding of MZMs alone cannot perform sufficient unitary operations necessary for quantum computation, they could still be useful for quantum memory. It is therefore of great interest to realize MZMs experimentally, a topic which we will turn to in subsequent sections.

1.2   Topological Superconductors

In the previous section we have defined MZMs and explored their physical properties, without addressing the question of whether *any* physical system would support them at all (we shall call such systems *topological*, and the phase in which

MZMs exist *topological phase*). One can actually predict the necessary ingredients based on the discussion in the previous section. First, the relation $\gamma^\dagger = \gamma$ (1.1) in the context of condensed matter system represents a quasiparticle with equal weights of particle and hole, which suggests the need for superconductivity; Second, since non-Abelian statistics is manifest only for braiding of single MZMs, the system must either be spinless, or spinful but with broken time-reversal symmetry.

In this section we shall discuss three systems which satisfy the above criteria and host MZMs. We first consider a one-dimensional (1D) spinless p-wave superconductor as a prototypical topological system. Although historically it was not the first model found to host MZMs (preceded for example by fractional quantum Hall states), it is arguably the simplest of all MZM-carrying models, comprising of only non-interacting Fermions with an unconventional pairing term. As such, it provides valuable intuition and has guided the subsequent search for topological heterostructures, which we shall also cover in this section.

1.2.1   1D Spinless p-wave Superconductors

We now start our discussion on a 1D spinless p-wave superconductor, the lattice model of which was first proposed by Alexei Kitaev in 2001 [4] as a toy model to realize MZMs. The Hamiltonian is given by

$$H = -\mu \sum_{i=1}^{N} a_i^\dagger a_i - \sum_{i=1}^{N-1} \left(t a_i^\dagger a_{i+1} + \Delta e^{i\phi} a_i a_{i+1} + \text{h.c.} \right), \qquad (1.11)$$
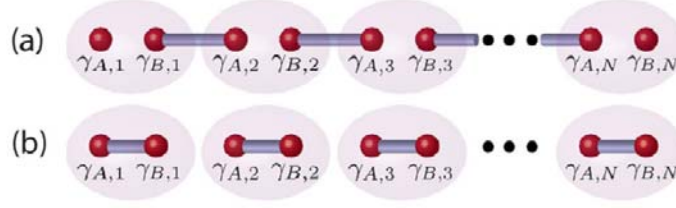
Figure 1.1: Schematic illustration of the Kitaev Model Eq. (1.11) in the limits of (a) $\mu = 0$, $t = \Delta \neq 0$ (b) $\mu \neq 0$, $t = \Delta = 0$. Adapted from Ref. [10].

where h.c. stands for Hermitian conjugation, a_i annihilate the electron on site i, μ is the chemical potential, $t \geq 0$ is the nearest-neighbor hopping, and $\Delta e^{i\phi}$ is the p-wave pairing between adjacent sites.

We express (1.11) in the Majorana operators, which are given by the transformation

$$a_i = \frac{e^{-i\phi/2}}{2} \left(\gamma_{i,A} + i\gamma_{i,B} \right), \tag{1.12}$$

where $\gamma_{i,A/B}$ are two species of Majorana operators defined at the ith site. In this basis,

$$H = -\frac{\mu}{2} \sum_{i=1}^{N} \left(1 + i\gamma_{i,A}\gamma_{i,B} \right) - \frac{i}{2} \sum_{i=1}^{N-1} \left[(\Delta + t)\, \gamma_{i,A}\gamma_{i+1,B} + (\Delta - t)\, \gamma_{i,B}\gamma_{i+1,A} \right]. \tag{1.13}$$

The Majorana physics of this Hamiltonian is easy to extract in two special limits. When $\mu = 0$ and $t = \Delta \neq 0$ [see Fig. 1.1(a)], the Hamiltonian simplifies to

$$H = -it \sum_{i=1}^{N-1} \gamma_{i,A}\gamma_{i+1,B}. \tag{1.14}$$

The salient feature is that the Majorana operators $\gamma_{1,B}$ and $\gamma_{N,A}$ are absent from the Hamiltonian, and therefore satisfy (1.2). They are the MZMs of the system at this

particular choice of parameters. To extract the regime of parameters in which the system is in the topological phase, we make the following observation: quasiparticles and their particle-hole counterparts have energies $\pm E$, while the energies of the MZMs, being their own antiparticles, are pinned at zero. Therefore, for a wire long enough that direct coupling between the MZMs at the two ends are avoided, the MZMs must persist provided that the bulk gap does not close. Since the bulk excitation energies of (1.11) are given by

$$E_{\text{bulk}}(k) = \sqrt{(2t \cos k + \mu)^2 + \Delta^2 \sin^2 k}, \quad -\pi < k \leq \pi, \tag{1.15}$$

we see that the bulk gap only closes at $\mu = \pm 2t$. As we have shown that at a special point within the regime $-2t < \mu < 2t$ MZMs exist, we can conclude that this model is in the topological phase for $-2t < \mu < 2t$.

At another special choice of parameters with $\mu \neq 0$ and $t = \Delta = 0$ [see Fig. 1.1(b)], the Hamiltonian simplifies to $H = -\mu \sum_{i=1}^{N} a_i^\dagger a_i$, which is topologically trivial (since all modes have an energy of $-\mu$). With this we can then conclude that the system is topologically trivial for $|\mu| > 2t$. In summary we have thus proven that the system is topological (and hosts MZMs) if and only if μ lies within the bandwidth (i.e. $|\mu| < 2t$). This fact will be useful in the discussion below.

1.2.2 Bogoliubov de-Gennes Hamiltonian and Pfaffian invariant

We have mapped out the topological phase diagram of the Kitaev model via explicit demonstration of (non-)existence MZMs on a finite wire. There is, how-

ever, an alternative approach to computing the phase diagram that relies on the bulk Hamiltonian only, and we shall state the result here. With a general Hamiltonian H involving spin-1/2 Fermions $a_\sigma^{(\dagger)}$, its quasiparticles wavefunction and energy could be found from the equation $[H, \gamma^\dagger] = E\gamma^\dagger$, which, upon substituting $\gamma^\dagger = \sum_\sigma \int d\boldsymbol{x} \left(ua_\sigma^\dagger + va_\sigma\right)$, gives an equation

$$H_{\text{BdG}}\left(\boldsymbol{x}\right)\Psi = E\Psi \tag{1.16}$$

where $\Psi\left(\boldsymbol{x}\right) = \begin{pmatrix} u_\uparrow\left(\boldsymbol{x}\right) & u_\downarrow\left(\boldsymbol{x}\right) & v_\downarrow\left(\boldsymbol{x}\right) & -u_\uparrow\left(\boldsymbol{x}\right) \end{pmatrix}^T$ and the Bogoliubov de-Gennes (BdG) Hamiltonian H_{BdG} satisfies $\{H_{\text{BdG}}, \Xi\} = 0$ (where $\Xi = \sigma_y \tau_y K$ and K is the conjugation operator) for its particle-hole symmetry. In an infinite 1D system, the 4×4 Hamiltonian could be Fourier-transformed to H_k, from which a topological index could be computed by

$$Q = \text{sgn} \prod_{k \in \{0, \pi\}} \text{Pf}\left(H_k \Xi\right), \tag{1.17}$$

where sgn is the sign function and Pf is the Pfaffian of a matrix, defined recursively for a $2n \times 2n$ skew-symmetric matrix M as

$$\text{Pf}(M) = \sum_{j=2}^{2n} (-1)^j m_{1j} \text{Pf}(M_{\hat{1}\hat{j}}), \tag{1.18}$$

where m_{1j} is j^{th} element in the first row of M, and $M_{\hat{1}\hat{j}}$ denotes a matrix with the first and the jth rows and columns removed. The Pfaffian of the 0×0 matrix is defined to be one.
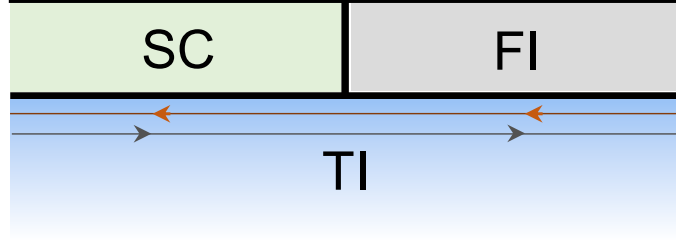
Figure 1.2: Schematic illustration of the topological insulator-based heterostructure. A SC and FI is put in proximity with the edge of a 2D TI.

When $Q = -1$, the system would be in its topological phase supporting odd number of MZMs at each end of the system, while for $Q = 1$ the system would be topologically trivial.

1.2.3 Topological Insulator / Superconductor / Ferromagnetic Insulator Heterostructure

While the p-wave superconducting chain is mathematically simple, it is hard to find in nature. The vast majority of superconductors found are spin-singlet, and s-wave superconductors are the most common. In 2008 Fu and Kane [11] pointed out that a topological phase can be constructed by inducing s-wave superconductivity on the surface of a TI. We now present a modification of their proposed model, in which the TI is 2D instead of 3D, and its edge with induced superconductivity and Zeeman term is described by the Hamiltonian (see Fig. 1.2)

$$H = \int dx \left[\sum_\sigma a_\sigma^\dagger \left(-i v_F \sigma \partial_x - \mu \right) a_\sigma + \left(\Delta a_\uparrow a_\downarrow + \text{h.c.} \right) + V_Z \left(a_\uparrow^\dagger a_\downarrow + a_\downarrow^\dagger a_\uparrow \right) \right],$$

$$(1.19)$$

where $\sigma = \uparrow/\downarrow = \pm 1$ represents spin, v_F is the Fermi velocity of the edge channel, μ is the chemical potential, Δ is the induced s-wave SC pairing, and V_Z is a Zeeman term induced either by a magnetic field or a ferromagnetic insulator (FI).

To explore the topological properties of this Hamiltonian, we shall try to draw a connection to the Kitaev model presented in Sec. 1.2.1. To this end, we consider a uniform edge for which the Hamiltonian in k-space reads

$$
\begin{aligned}
H \;=\; & \sum_k \Big[v_F k \left(a_{k\uparrow}^{\dagger} a_{k\uparrow} - a_{k\downarrow}^{\dagger} a_{k\downarrow} \right) - \mu \left(a_{k\uparrow}^{\dagger} a_{k\uparrow} + a_{k\downarrow}^{\dagger} a_{k\downarrow} \right) \\
& + \left(\Delta a_{k\uparrow} a_{-k\downarrow} + \text{h.c.} \right) + V_z \left(a_{k\uparrow}^{\dagger} a_{k\downarrow} + a_{k\downarrow}^{\dagger} a_{k\uparrow} \right) \Big].
\end{aligned}
\tag{1.20}
$$

Since the pairing term couples the two (spin) species at opposite values of k, we follow Ref. [12] and redefine the species by

$$
c_k \;=\; \begin{cases} a_{k\uparrow}, & k > 0 \\[4pt] a_{k\downarrow}, & k < 0 \end{cases} , \qquad d_k = \begin{cases} a_{k\uparrow}, & k < 0 \\[4pt] a_{k\downarrow}, & k > 0 \end{cases} ,
\tag{1.21}
$$

with which the Hamiltonian becomes

$$
H \;=\; \sum_k \Big\{ v_F \, |k| \left(c_k^{\dagger} c_k - d_k^{\dagger} d_k \right) - \mu \left(c_k^{\dagger} c_k + d_k^{\dagger} d_k \right)
\tag{1.22}
$$

$$
+ \left[\frac{\Delta \mathrm{sgn} k}{2} \left(c_k c_{-k} + d_k d_{-k} \right) + \text{h.c.} \right] + V_z \left(d_k^{\dagger} c_k + c_k^{\dagger} d_k \right) \Big\},
\tag{1.23}
$$

where sgn is the sign function. This Hamiltonian describes two species of Fermions with odd-parity (p-wave) pairing terms proportional to $\Delta \mathrm{sgn} k$. When $V_z = 0$,

the two species becomes independent, with the $c\,(d)$-species Fermions having a(n) "(inverted-)V"-shaped dispersion with the tip at the origin. Therefore, with any choice of μ, exactly one of the two species of Fermions would be in its topological phase (with μ lying within its bandwidth).

We have therefore proven that the system is always in its topological phase if $V_Z = 0$. Turning on V_Z introduces inter-species hopping and gap out the Dirac dispersion and for small values of μ it will fail to lie within the bandwidth of either species of Fermions, making the system non-topological. The exact point of phase transition is found by solving for the gap-closure point, which gives the condition for topological phase as

$$|V_Z| < \sqrt{|\Delta|^2 + \mu^2}. \qquad (1.24)$$

It might seems unnecessary to introduce the Zeeman term, and MZMs would be present at the "end" of the system. There is a catch, however – due to the Fermion-doubling theorem the form of kinetic term in (1.19) can only be realized on the edge of a 2D system, and as such cannot have a termination joining the vacuum. The minimal way to induce localized MZMs would then be to assemble a SC/FI interface on the TI edge (Fig. 1.2), or to apply a magnetic field weak enough such that the edge is topological in the portion in proximity with the superconductor.

1.2.4 Nanowire / Superconductor Heterostructure

The TI-base heterostructure proposal had been an important step, since the need for unconventional superconductivity was circumvented. The drawback is the
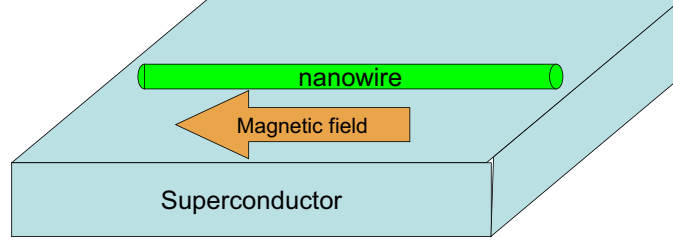
Figure 1.3: Schematic illustration of the nanowire-based heterostructure. A nanowire with strong SOC is put on the surface of a superconductor. A magnetic field is applied in parallel to the wire. Adapted from Ref. [13].

need for TI, since its fabrication is experimentally challenging. In 2009 Sau et al. [14, 13] proposed a 2D heterostructure that generate MZMs with only conventional SMCs and SCs. This was later simplified to 1D SMC nanowire proposals [5, 6], which we discuss here.

Consider a SOC nanowire deposited on the surface of an s-wave superconductor, and a magnetic field is applied parallel to the wire (see Fig. 1.3). The Hamiltonian describing the electronic modes on the nanowire is

$$H = \int dx a^\dagger \left(-\frac{\partial_x^2}{2m} - \mu - i\alpha\sigma_y\partial_x + V_Z\sigma_z \right) a + \int dx \left(\Delta a_\uparrow a_\downarrow + \text{h.c.} \right), \qquad (1.25)$$

where $a = \begin{pmatrix} a_\uparrow & a_\downarrow \end{pmatrix}^T$ is the vector of annihilation operators in spin space, m is the effective mass of electrons, μ is the chemical potential, α is the strength of SOC, $V_Z = g\mu_B B$ is the strength of spin splitting due to magnetic field B, Δ is the s-wave pairing induced from the superconductor, and h.c. denotes Hermitian conjugation.

We consider the limit $|V_Z| \gg m\alpha^2$, $\mu = 0$ and $\alpha \neq 0$, such that in the normal state ($|\Delta| = 0$) the Fermi level crosses only a single band at $\pm k_F$. We can project

the Hamiltonian in the lower, occupied band, which yields [9], with finite Δ,

$$H = \int dx \left[a_-^\dagger \left(-\frac{\partial_x^2}{2m} - |V_Z| \right) a_- + \frac{\alpha}{2|V_Z|} \left(\Delta a_- \partial_x a_- + \text{h.c.} \right) \right], \qquad (1.26)$$

where a_- annihilates the mode on the lower band. This Hamiltonian is just the continuum version of the Kitaev chain (1.2.1) where now the bandwidth is infinite and it is in the topological phase. As before, the topological phase boundary can be obtained by solving for the gap closure point as $|V_Z|$ is varied. For finite values of α, we therefore have a topological phase for

$$|V_Z| > \sqrt{|\Delta|^2 + \mu^2}. \qquad (1.27)$$

At this point it should be pointed out that $|V_Z|$ can be greater than $|\Delta|$ without destroying superconductivity, because it is induced from a bulk superconductor, which does not experience a strong magnetic field provided that the Lande g-factor of the nanowire is large. Also, we have chosen the direction of Zeeman term (proportional to σ_a) to be perpendicular to the SOC term (proportional to σ_y) in Eq. (1.25). If they were parallel the system is non-topological and MZMs are absent. Since experimentally the direction of the Zeeman term can be tuned, the emergence (disappearance) of MZMs as the Zeeman term is oriented perpendicular (parallel) to the SOC term provides another experimental verification of the theory.

1.2.5 Helical Zeeman Proposal

An important class of proposals closely related to the nanowire proposal (1.25) has spatially rotating Zeeman terms in place of the SOC. The connection can be made clear [10] by making the unitary transformation $a \to e^{-im\alpha\sigma_y x}\tilde{a}$ on (1.25), yielding

$$
\begin{aligned}
H &= \int dx \left\{ \tilde{a}^\dagger \left[-\frac{\partial_x^2}{2m} - \left(\mu + \frac{1}{2}m\alpha^2 \right) + \boldsymbol{B}_{\text{eff}}(x) \cdot \boldsymbol{\sigma} \right] \tilde{a} \right. \\
&\quad \left. + (\Delta\tilde{a}_\uparrow\tilde{a}_\downarrow + \text{h.c.}) \right\}
\end{aligned}
\tag{1.28}
$$

where $\boldsymbol{B}_{\text{eff}}(x) = -\sin(2m\alpha x)\,\hat{\boldsymbol{x}} + \cos(2m\alpha x)\,\hat{\boldsymbol{z}}$. This Hamiltonian describes a nanowire subject to a Zeeman field with a helical arrangement induced by, for example, magnets of sub-micrometer sizes [15, 16].

1.2.6 Proposals based on Shiba States

In recent years, a class of proposals that are based on Yu-Shiba-Rusinov states [17, 18, 19] (we shall use the term "Shiba" states instead) have drawn the attention of many researchers [20, 21, 22, 23, 24, 25, 26, 27]. These states appear when ferromagnetic elements are deposited on the surface of s-wave SCs. Due to TRS-breaking subgap localized are induced. When multiple Shiba states aligned along a line, they could hybridize and form an effective 1D system. With (effective) SOC in the system, the 1D system could be in a topological phase with MZMs. We shall describe this class of proposals, and in particular its relation to a recent

experiment [28] in chapters 5-7 in this thesis.

1.2.7   Other

We have presented the Hamiltonians of 1D topological systems, with MZMs realized at the ends of the topological regions. Corresponding 2D versions of the chiral p-wave superconductor, TI heterostructure and the SMC nanowire proposals are straightforward to construct, yielding respectively 2D $p + ip$ superconductor [3], 3D TI heterostructure [11] and 2D SOC SMC heterostructure [14]. In these systems, the MZMs are located at the vortex cores of the pairing potential Δ. If the system has an odd number of vortices, a delocalized MZM would be present along the boundary of the 2D plane so that the total number of MZMs of the whole system is even.

Another direction is to consider the continuum/discretized limits of the various models (with the exception of TI-based systems since the edge dispersion cannot be discretized). The discretization of the nanowier proposal and the helical Zeeman proposal is more than a step to numerical modeling; it can also bring useful insight with which new proposals are constructed. For example, proposals based on quantum dot arrays [29, 30] can be considered as based on the discretized version of the nanowire, while proposals based on magnetic adatoms with spatially varying polarization [15, 31, 32, 20, 33] can be considered as based on the discretization of the helical Zeeman proposal.

1.3 Experimental Signatures of Majorana Zero Modes

Since the ultimate goal is to utilize MZMs in topological quantum computation, an ideal demonstration of MZMs would be a direct measurement of their braiding statistics. The current fabrication techniques, however, is still too primitive to carry out such experiments. Therefore, we shall instead look into two indirect probes for MZMs – the fractional Josephson effects and the zero-bias conductance peak.

1.3.1 Fractional Josephson Effects

Consider two topological 1D systems placed next to each other, so that the MZMs from each of their ends hybridize. The Hamiltonian describing the junction is

$$H_J = -t \left(a_{LN}^\dagger a_{R1} + \text{h.c.} \right), \tag{1.29}$$

where a_{LN} (a_{R1}) is the regular Fermion operator at the rightmost (leftmost) site of the left (right) system, and $t > 0$ is the strength of tunneling between them. Using (1.12) to project this onto the subspace that comprises of the MZMs, we have the low-energy effective Hamiltonian

$$
\begin{aligned}
H_{\text{eff}} &= -\frac{t}{2} \cos\left(\frac{\phi_L - \phi_R}{2} \right) i\gamma_1 \gamma_2 && \text{(1.30)} \\
&= -t \cos\left(\frac{\phi_L - \phi_R}{2} \right) \left(c^\dagger c - \frac{1}{2} \right) && \text{(1.31)}
\end{aligned}
$$

where γ_1 and γ_2 are the localized MZMs at the ends near the junction, and $c = \gamma_1 + i\gamma_2$ is the Fermion operator constructed from them. $\phi_{L/R}$ are the phases of the superconductivity at the left/right systems respectively. The other MZMs that are located at the far outer ends of the two systems do not participate in the tunneling and are therefore not present in the Hamiltonian.

We therefore see that the effective Hamiltonian (1.31) is 4π-periodic in $\delta\phi = \phi_L - \phi_R$, the phase difference between the two superconductors. This leads to the measurable quantity, the Josephson current given by [10]

$$I_J = \frac{2e}{\hbar} \frac{d \langle H_{\text{eff}} \rangle}{d (\delta\phi)} = \frac{et}{2\hbar} \sin \frac{\delta\phi}{2} (2n - 1), \tag{1.32}$$

which is also 4π-periodic in $\delta\phi$.

The purpose of measuring this current is two-fold. First, since the occupation number n in (1.32) determines the sign of I_J, the readout of the qubit can also be performed by measuring the junction current. Moreover, the detection of this periodicity constitutes a signature of MZMs because, for a junction made of conventional s-wave superconductors, the Andreev bound states are 2π-periodic in $\delta\phi$ [34],

$$E_J = \Delta \left(1 - T \sin^2 \frac{\delta\phi}{2} \right)^{1/2} \text{(doubly degenerate)}, \tag{1.33}$$

where T is the transmission coefficient of the junction in the normal state. Hence the effective Hamiltonian and the Josephson current are also both 2π-periodic in $\delta\phi$. However, it has been pointed out that [35] under certain conditions even junctions

18

made of conventional superconductors can display fractional Josephson effects.

1.3.2 Zero-Bias Conductance Peak

An obvious experiment to probe MZMs is that of tunneling. Consider a lead in tunneling contact with a MZM [36]. The Hamiltonian of the lead is

$$H_{\text{lead}} = \sum_\sigma \int_{-\infty}^0 \left(-iv_F a_{R\sigma}^\dagger \partial_x a_{R\sigma} + iv_F a_{L\sigma}^\dagger \partial_x a_{L\sigma} \right), \qquad (1.34)$$

$$= -iv_F \sum_\sigma \int_{-\infty}^\infty a_\sigma^\dagger \partial_x a_\sigma, \qquad (1.35)$$

where $a_{R/L\sigma}(x)$ describes right/left-moving excitations in the wire with spin σ and Fermi velocity v_F. In the second line we have used the mapping $a_\sigma(x > 0) = a_{L\sigma}(-x)$ and $a_\sigma(x < 0) = a_{R\sigma}(x)$ to cast the semi-infinite lead Hamiltonian into a chiral Fermion operator in the entire space. The most general coupling between this Fermion field and the MZM γ at $x = 0$ is

$$H_{\text{tun}} = -i\frac{t}{\sqrt{2}} \sum_\sigma \gamma \left[\xi_\sigma a_\sigma(0) + \xi_\sigma^* a_\sigma^\dagger(0) \right], \qquad (1.36)$$

with $|\xi_\sigma| = 1$. By redefining spins as $\psi_\lambda = \frac{1}{\sqrt{2}}(\xi_\uparrow a_\uparrow + \lambda \xi_\downarrow a_\downarrow)$, where $\lambda = \pm$, the system's Hamiltonian is

$$H = -iv_F \sum_\lambda \int_{-\infty}^\infty dx \psi_\lambda^\dagger \partial_x \psi_\lambda - it\gamma \left(\psi_+ + \psi_+^\dagger \right). \qquad (1.37)$$

19

Therefore, the field ψ_- drops out of the scattering problem. The scattering states are found by the equation of motion method, which gives:

$$E\psi_+ = -iv_F \partial_x \psi_+ - it\gamma \tag{1.38}$$

$$E\gamma = -2it \left[\psi_+ (0) + \psi_+^\dagger (0) \right]. \tag{1.39}$$

From this, one can solve for the scattering matrix $S(E) = \begin{pmatrix} S_{pp} & S_{ph} \\ S_{hp} & S_{hh} \end{pmatrix}$ which relates the incoming and outgoing modes by $\begin{pmatrix} \psi_+ (0^+) \\ \psi_+^\dagger (0^+) \end{pmatrix} = S \begin{pmatrix} \psi_+ (0^-) \\ \psi_+^\dagger (0^-) \end{pmatrix}$. Non-zero S_{ph} contributes to the tunneling conductance because it represents the amplitude of the process in which an incoming electron is reflected as an outgoing hole, contributing a Cooper pair of charge-$2e$ to the superconductor. Therefore, the differential tunneling conductance is given by

$$G(E) = \frac{dI}{dV} = \frac{2e^2}{h} |S_{ph}(E)|^2. \tag{1.40}$$

In particular, at $E = 0$ it is straightforward to show that $S(0) = \begin{pmatrix} 0 & -1 \\ -1 & 0 \end{pmatrix}$, describing a *resonant Andreev reflection* process in which perfect Andreev reflection always occur. Therefore, a tunneling experiment would show a zero-bias conductance peak (ZBCP) of height $\frac{2e^2}{h}$ if a MZM is present.

Several remarks are in order. First, the above analysis implicitly assumed zero temperature. At finite temperature, the ZBCP broadens and the height is

20

suppressed. Second, while we have focused on the tunneling from a spinful lead to a MZM, the conclusion that ZBCP is of height $\frac{2e^2}{h}$ (at $T = 0$) holds more generally for a spinful or spinless lead, and has been discussed from many perspectives in the literature [36, 37, 38, 39, 40, 41, 42, 43]. Last, measuring a ZBCP alone may hardly give conclusive evidence for MZM, since similar peaks could arise from some other physical mechanisms, like Kondo effects or weak antilocalization [44, 45]. However, observing the ZBCP to come and go as a parameter in the Hamiltonian as the system is tuned across (non-)topological regimes is arguably a strong evidence for the validity of the theory.

1.3.3   Experimental Progress

We here review the experimental data of an important work by Mourik et al. [7], which attempted to implement the nanowire proposal.

In this experiment [see Fig. 1.4(a)], SMC wires with strong SOC are put on a superconductor. An external magnetic field, whose direction and magnitude can be controlled, is applied parallel to the superconductor surface. A normal lead is attached to the end of the wire. A tunnel junction is formed between the super-conducting part and the part in contact with the lead by applying a gate near the interface, and the tunneling current is measured.

Fig. 1.4(b) shows the variation of differential conductance as the magnetic field is varied. We see that a ZBCP emerges as the strength of the magnetic field is increased beyond a certain point. A further piece of evidence is provided in
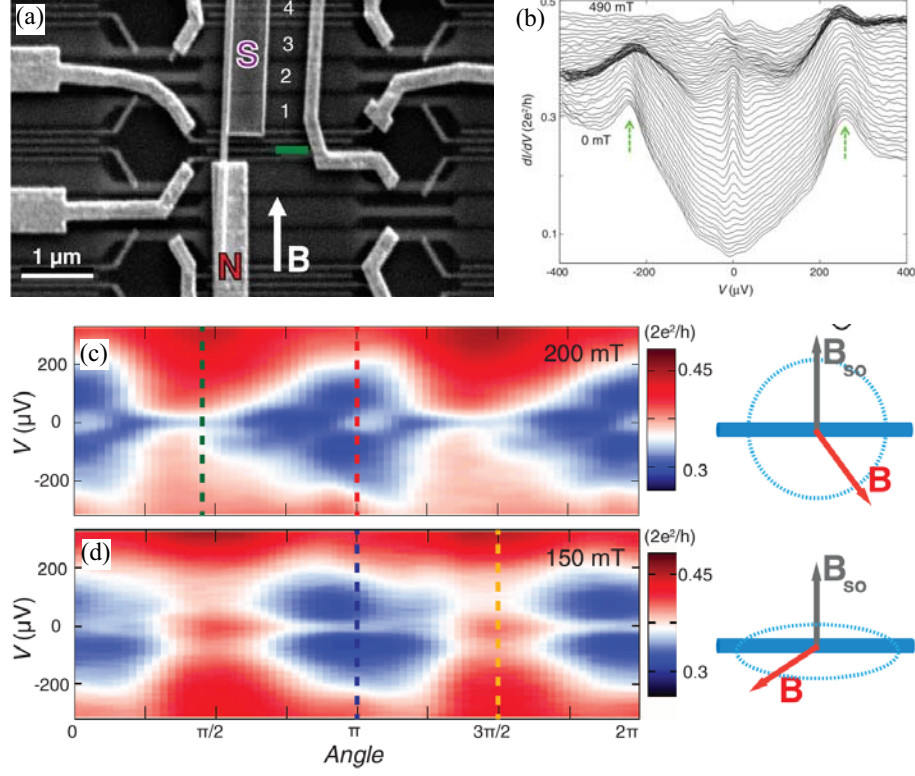
Figure 1.4: The experiment on the nanowire proposal. (a) The scanning electron microscope image of the setup. An InSb nanowire is put in contact with normal (N) and superconducting (S) contacts. The underlying gates (numbered 1-4) are used to tune the chemical potential of the wire. A gate (colored green) is used to form a tunnel barrier between the N and S contacts. (b) Differential conductance (dI/dV) versus bias voltage (V) for magnetic fields ranging from 0 to 490 mT (in steps of 10 mT). For clarity, traces are offset. (c) dI/dV versus V and the angle of the magnetic field, where the magnetic field is perpendicular to the SOC direction when Angle=0, π, and parallel to the SOC direction when Angle=$\frac{\pi}{2}$, $\frac{3\pi}{2}$. (c) dI/dV versus V and the angle of the magnetic field, where the magnetic field is always perpendicular to the SOC direction. Adapted from Ref. [7].

Fig. 1.4(c,d), in which the direction of the magnetic field is varied. When its direction is parallel to the SOC [i.e. at angle= $\frac{\pi}{2}, \frac{3\pi}{2}$ in Fig. 1.4(c)], the ZBCP is absent, while when they are perpendicular [i.e. at angle= $0, \pi$ in Fig. 1.4(c) and for all angles in Fig. 1.4(d)] the ZBCP is most pronounced. All of these signatures are consistent with the theory, and provide evidence that the ZBCP is indeed due to a MZM.

1.4 Experimental Complications

Experimental implementation of the nanowire proposal of Sec. 1.2.4 was confronted by a number of problems, some of which are described briefly in this section. Their theoretical treatment is given in the main part of this thesis.

1.4.1 Disorder

It is natural to ask how robust is the superconducting gap against (non-magnetic) disorder. Anderson's theorem states that if a Hamiltonian (with an s-wave pairing term) has time-reversal symmetry, then any amount of disorder cannot degrade the superconductivity gap of the system. This has implications for the nanowire proposal and the TI-based proposal, which we describe separately below.

1.4.1.1 Nanowire Heterostructure

For the nanowire proposal in the topological phase, since a Zeeman field must be present according to (1.27), time-reversal symmetry is absent and disorder can have an effect on the gap. Refs. [45, 46, 47, 48] showed that disorder can pro-
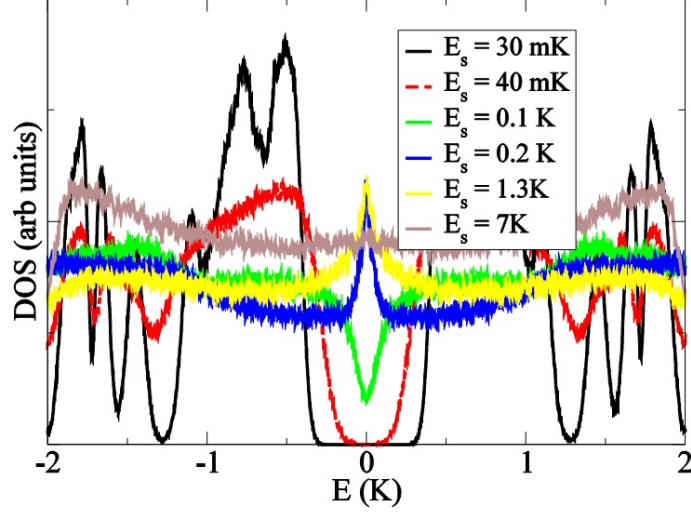
Figure 1.5: The disorder-averaged density of states for the nanowire model in its topological phase, where the parameters are chosen as $\mu = V_Z = 5K$ and $\Delta = 3K$. $E_s = \hbar/\tau$ characterizes the strength of disorder where τ is the mean scattering time. Adapted from Ref. [45].

duce subgap states that cluster around zero energy, producing signatures similar to MZMs. This effect is due to the symmetry of the system and weak antilocalization. For example Fig. 1.5 is the results of of Ref. [45], which shows that for the nanowire in its non-topological phase, strong disorder can induce a zero-bias peak.

Another question that could be asked about disorder is its effect on the topological phase diagram. Ref. [49] computed the phase diagram with ensemble-averaged disorder. Fig. 1.6 shows its result, in which γ is the scattering length of the system. We see that increasing disorder shrinks the topological region. Interestingly, Ref. [50] showed that for a single realization of disorder it is possible to drive a non-topological system to topological (see Fig. 1.7).
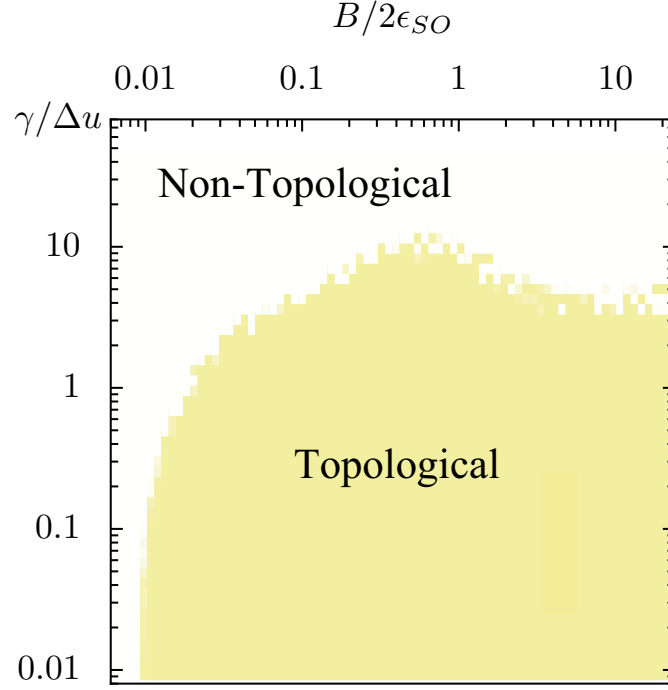
Figure 1.6: The topological phase diagram for the nanowire proposal as a function of γ and B, where the parameters are chosen as $\mu = 0$ and $\Delta = \epsilon_{\text{SO}} = m\alpha^2/2$. Here disorder is introduced via static Gaussian white noise potential $V(x)$ with $\langle V(x) \rangle = 0$ and $\langle V(x) V(x') \rangle = \gamma \delta(x - x')$. Adapted from Ref. [49].
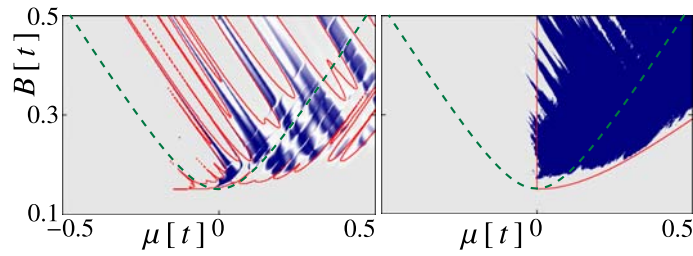
Figure 1.7: The topological phase diagram for a tight-binding model of the nanowire proposal as a function of B and μ, where the other parameters are chosen as $\Delta = 0.15t$ and $\alpha = 0.05/a$, where t is the nearest-neighbor hopping and a the lattice constant. Here disorder is introduced via static Gaussian white noise potential $V(x)$ with $\langle V(x) \rangle = 0$ and $\langle V(x) V(x') \rangle = 0.06t^2 \delta(x - x')$. The green dotted (red) line is the phase boundary computed without (with) disorder. The left (right) panel corresponds a nanowire with length $L = 100a\,(4000a)$. Adapted from Ref. [50].

1.4.1.2 Topological Insulator Heterostructure

According to (1.24), the TI-based heterostructure does not require a Zeeman field to drive the system into a topological phase. It is therefore widely believed [12] that the TI-based heterostructure is totally immune to disorder and thus ideal for hosting MZMs. However, as we have noted in Fig. 1.2, it is necessary to put an FI in order to localize MZMs at the end of the topological region. It is of interest to ask when such local time-reversal breaking could have an noticeable effect on the SC gap protecting the MZM. This question is addressed in Chapter 3.

1.4.2 "Soft gap" Problem

We have alluded to this problem in previous section. Fig. 1.8 demonstrates that all initial attempts to implement the nanowire proposal faced similar issues, that is, there is a finite density of subgap states making the induced "gap" V-shaped. It should be remembered that the topological protection depends on the size of the superconducting gap in the topological system. Therefore, one must get a clean gap in order to perform any meaningful braiding operations.

Disorder in the wire cannot be the cause, since this problem persists even at zero magnetic field, at which point the system is time-reversal-symmetric, and Anderson's theorem guarantees that disorder alone cannot degrade the gap. Therefore, the cause of this problem was not obvious, and a number of theoretical works were devoted to explain this observation. For example, Ref. [55] suggested that the hybridization between the SMC nanowire and the metallic lead is the cause. In
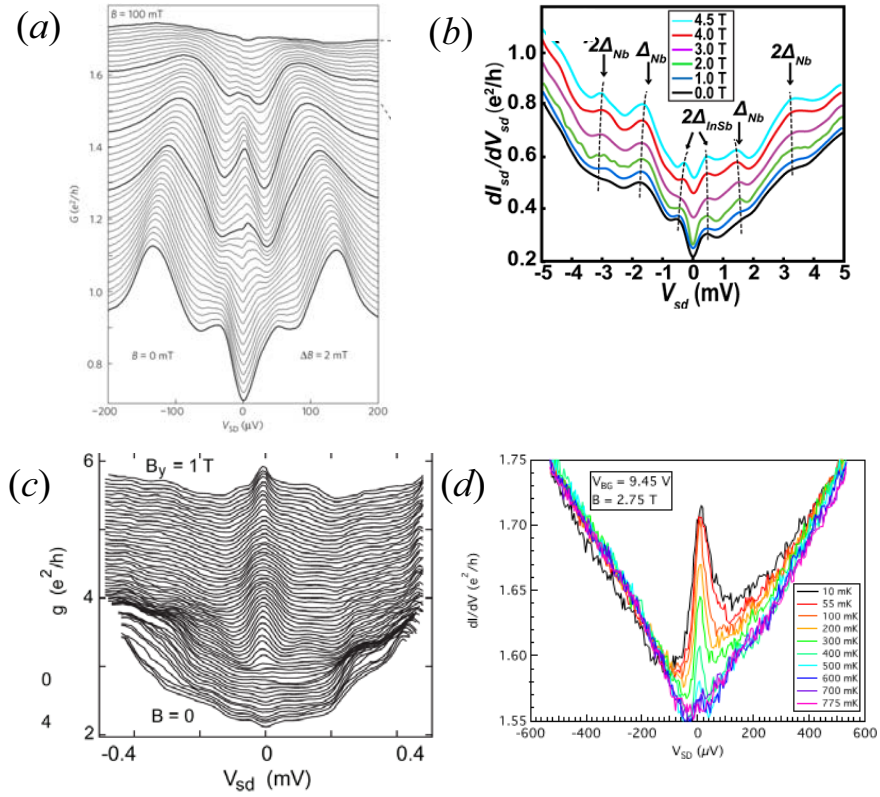
Figure 1.8: Experimental results from four independent experimental groups that could be directly compared with Fig. 1.4(b). Adapted respectively from (a) Ref. [51], (b) Ref. [52], (c) Ref. [53] and (d) Ref. [54].
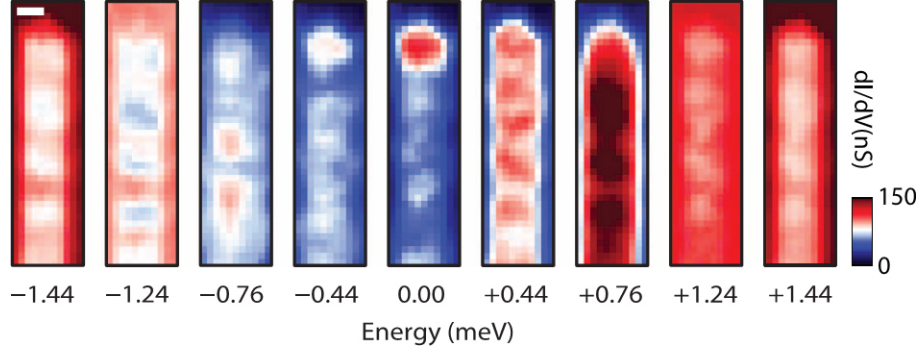
Figure 1.9: Experimental results adapted from Ref. [28]. Different panels show the contour plot of conductance as a function of position for various values of bias voltage. The salient feature is that at zero-bias, a peak that is highly localized at the edge of the wire emerges.

Chapter 4 we shall discuss another possible mechanism.

1.4.3   Measurement of Local Density of States

The current implementations of the nanowire proposal are capable of measuring the tunneling conductance at the end of the nanowire only. To a very good approximation, the conductance measured is proportional to the local density of states (LDOS) at the end of the wire. To verify that the zero mode is indeed localized at the end (thus consistent with the MZM picture), it is important to measure the LDOS in the middle of the topological system. Chapters 5 and 6 discuss new platforms in which such measurement are possible with STM.

1.4.4   Short Localization Length

In experimental setups similar to what is described in Chapters 5 and 6 of this thesis, zero-energy end states, purportedly MZMs, were observed [28]. However, a

strange feature of the result needs a theoretical explanation, namely the extremely short localization of the MZMs. Since the the localization length of a MZM should be roughly the coherence length of the system, and the induced gap is very small, it is natural to expect a long localization length. Instead, the observed MZMs are localized to within a few lattice units at the end of the system (see Fig. 1.9). In Chapter 7 we shall explore a possible explanation of this phenomenon.

1.5 Outline of the Thesis

In this thesis, we critically examine the experimental aspects of realization of MZMs in solid state systems. In Chapters 2-4, we first discuss a number of theoretical works pertinent to the issues we discussed in this introduction. Then in Chapters 5-7 we explore and discuss in depth a new proposal to realize MZMs.

In Chapter 2 we first consider the effects of disorder on the MZM at the end of a 1D topological p-wave SC. The theoretical treatment will generalize the Eilenberger theory of SC, with short-ranged variations fully captured in our formalism. The work in this chapter has led to the publication of Ref. [56].

In Chapter 3, we investigate the effects of local time-reversal-symmetry breaking, together with disorder, on the MZM induced in the TI-based heterostructure . We shall find that, while the MZM on a single-channel TI edge is immune to disorder, for a multi-channel edge subgap states could appear. The work in this chapter has led to the publication of Ref. [57].

In Chapter 4 we revisit and investigate into the soft gap problem, which is

present in virtually all implementations of the nanowire proposal. We numerically consider the effects of finite temperature, magnetic/non-magnetic disorder, quasiparticle broadening, and SC/nanowire interface inhomogeneity, and conclude that the last one is the most probable cause of the soft gap. We also present a simple theoretical model to treat the interface inhomogeneity, and discussed the effort of a recent experimental group that improved the interface quality, leading to a harder induced gap. The work in this chapter has led to the publication of Ref. [58].

In Chapters 5 and 6 we propose and discuss new platforms to realize MZMs. In particular, we consider depositing magnetic adatoms on the surface of a SOC SC. The advantage of this system is that the LDOS at the middle of the system can be directly probed with STM, which was not possible in the nanowire systems. The work in this chapter has led to the publication of Ref. [27, 59].

In Chapter 7 we discuss an issue that came up in an experimental setup similar to what is described in Chapters 5 and 6. It was found that the zero-energy mode at the ends of the chain has very short localization length. This may seem contradictory to the Majorana picture since the induced gap is so small and the localization length is inversely proportional to the induced gap. We shall point out that the substrate (the 3D SC) can induce a renormalization of the length scale of the chain, leading to a short localization length of the MZM. The work in this chapter has led to the publication of Ref. [60].

In Chapter 8 we present our conclusions and discuss possible future research directions and open problems.

Chapter 2

Disorder in effective p-wave nanowires

The effects of disorder in 1D topological systems have been previously investigated [61, 62, 63, 64, 49, 46, 65, 47, 66, 67, 45, 48, 68, 50] from a number of different perspectives. One approach to the problem consists of introducing many realizations of disorder and ensemble-averaging at the end to extract universal properties [46, 47, 67, 68, 45, 50]. While this approach is more akin to the experimental situation (where there is only a single realization of disorder at each setup), the end result of the posterior disorder averaging is mostly numerical and few analytical statements can be made. On the other hand, previous attempts of anterior disorder averaging were mostly concerned with the properties in the bulk [61, 62, 64, 49, 63, 65, 66]. The effects of ensemble-averaged disorder on the end MZMs were not fully investigated.

In this chapter, we undertake the task of analyzing the effects of ensemble-averaged disorder on a topological 1D system, the idealized spinless p-wave superconducting wire. In particular, we treat the disorder in the self-consistent Born approximation (SCBA) and investigate its effects on the spectral properties of the whole system, with an emphasis on its boundary where the MZMs reside. To this end, it is convenient to adopt a formalism similar to the Eilenberger equations [69], but including pair-breaking effects of disorder in the theory. Our formalism differs

from the conventional quasiclassical treatment of disordered superconductors in two ways. First, unlike the conventional approach, we consider only weak disorder and do not take the diffusive limit to derive the Usadel equations [70], as this would wipe out the spectral gap in the topological system. Second, we do not start by integrating out the fast-oscillating parts of the Green function, but instead consider the Green function in a chiral basis and keep all its spatial dependence. This is possible only for 1D problems, and is essential to extract the exact spatial dependence of the MZM.

We emphasize that the focus of this chapter is on the SM heterostructures in the presence of SOC and spin splitting [11, 71, 14, 13, 5, 6] proposed to realize MZMs, all of which have s-wave pairing terms induced by proximity effect through Cooper pairs tunneling from nearby superconductors. By projecting the Hamiltonians of these systems to their low-energy subspaces [5, 12, 10], one universally obtains effective p-wave superconductors but with model-specific pairings and scattering strengths [see Eq. (3.1) below]. The crucial difference of this SM Majorana nanowire from an intrinsic p-wave superconducting wire is that, since now the pairing term is proximity-induced, it is both unnecessary and inappropriate to perform self-consistent theoretical calculations because there is no intrinsic pairing interaction in the wire itself [72]. We shall thus take the pairing strength as a fixed parameter without solving the self-consistent gap equation following all earlier theoretical works in the literature on this problem.

2.1   Formalism

We consider a semi-infinite wire at $x > 0$ described by the linearized Hamiltonian

$$H = \sum_{C=R/L} \int_0^\infty dx \left(-iv_F s_C \psi_C^\dagger \partial_x \psi_C + \Delta s_C \psi_C \psi_{\bar{C}} + V_f \psi_C^\dagger \psi_C + V_b \psi_C^\dagger \psi_{\bar{C}} \right) \quad (2.1)$$

Here v_F is the Fermi velocity, Δ is the p-wave superconducting order parameter, and $s_C = \pm 1$ for $C = R/L$, where R/L denotes right/left moving electrons. $V_{f/b}$ is the forward/backward scatterings due to static quenched disorder, assumed to be short ranged here. Coulomb disorder, which might be present in real SM nanowire systems of experimental interest, will typically be screened by the surrounding gates, the normal leads, the superconductor, and by the electrons in the wire themselves leading presumably to short-ranged elastic disorder. The linearized form of disorder in Eq. (3.1) is related to the full disorder potential U by

$$V_f(x) = \sum_{q \sim 0} U_q e^{iqx}, \quad (2.2)$$

$$V_b(x) = \sum_{q \sim 0} U_{q-2k_F} e^{iqx}, \quad (2.3)$$

where k_F is the Fermi momentum and U_q are the Fourier components of U.

The spectral properties of the system are encoded in the Nambu-Gorkov Green function $G(x, t, x', t') = -i \langle \mathcal{T} \Psi(x, t) \Psi^\dagger(x', t') \rangle$, where $\Psi = \left(\psi_R, \psi_L, \psi_L^\dagger, \psi_R^\dagger \right)^T$. We are interested, following the spirit of the Eilenberger theory which is being

generalized in this chapter, in the Green function defined as

$$g(x, \omega) = v_F i \lim_{\epsilon \to 0^+} \left[G(x, x - \epsilon) + G(x, x + \epsilon) \right] \sigma_3 \tau_3 \qquad (2.4)$$

where σ and τ are Pauli matrices acting on the R/L space and particle-hole space, respectively. To extract the LDOS from g, we note that since the fermion operator is linearized in the form of $\psi(x) \simeq \psi_R e^{ik_F x} + \psi_L e^{-ik_F x}$, the Green function of $\psi(x)$ is related to the Green function in the chiral basis via

$$
\begin{aligned}
G^{(0)}(x, x') \simeq \ & G_{RR} e^{ik_F(x-x')} + G_{RL} e^{ik_F(x+x')} \\
& + G_{LR} e^{-ik_F(x+x')} + G_{LL} e^{-ik_F(x-x')}.
\end{aligned}
\qquad (2.5)
$$

Therefore, the LDOS is given by

$$
\begin{aligned}
\nu(x, \omega) \ = \ & \frac{\nu_0}{4} \left[\mathrm{TrRe}\,(g\sigma_3\tau_3) - \mathrm{TrRe}\,(g\sigma_-\tau_3)\, e^{2ik_F x} \right. \\
& \left. + \mathrm{TrRe}\,(g\sigma_+\tau_3)\, e^{-2ik_F x} \right], \\
= \ & \frac{\nu_0}{4} \mathrm{TrRe}\,(g\sigma_3\tau_3 + 2g\sigma_+\tau_3 \cos 2k_F x),
\end{aligned}
$$

$$(2.6)$$

$$(2.7)$$

where $\nu_0 = \frac{1}{\pi v_F}$ is the LDOS in the normal state and $\sigma_\pm = \frac{1}{2}(\sigma_1 \pm i\sigma_2)$. In Eq. (2.7), the first(second) term contains the slowly (fast) -oscillating part of the LDOS. Conventional derivation of Eilenberger equations [69, 73] effectively ignores the second term. One key aspect of our generalization is keeping these oscillatory terms which can be done completely analytically (at least for the 1D problem of current interest).

34

The equation of motion of g can be derived from the Dyson's equations of G. As both spatial arguments of G are set to x, we must use the two conjugate Dyson's equations:

$$(\omega - H_{\text{BdG}} - \Sigma) G(x, y) = \delta(x - y), \tag{2.8a}$$

$$G(y, x)(\omega - H_{\text{BdG}} - \Sigma) = \delta(x - y), \tag{2.8b}$$

where $H_{\text{BdG}} = -iv_F\sigma_3\tau_3\partial_x + \Delta\sigma_3\tau_1$ and Σ is the self-energy due to ensemble-averaged disorder V_f and V_b in Eq. (3.1). Here the derivative acting on the right is understood as $G(y, x) i\overleftarrow{\partial_x} = -i\partial_x G(y, x)$. By collecting the terms $\partial_x G(x, y)$ and $\partial_x G(y, x)$, we have

$$v_F\partial_x g = i\left[\omega\sigma_3\tau_3 - i\Delta\tau_2 - \sigma_3\tau_3\Sigma, g\right]. \tag{2.9}$$

The self-energy Σ due to ensemble-averaged disorder is

$$\Sigma(x, x') = \delta(x - x')\left\langle V(x) V(x') G^{(0)}(x, x')\right\rangle, \tag{2.10}$$

where $G^{(0)}$ is the Green function of the unlinearized fermion operator. With the

linearization $\psi(x) \simeq \psi_R e^{ik_F x} + \psi_L e^{-ik_F x}$, V and $G^{(0)}$ becomes

$$
\begin{aligned}
G(x, x') &\simeq G_{RR} e^{ik_F(x-x')} + G_{RL} e^{ik_F(x+x')} \\
&\quad + G_{LR} e^{-ik_F(x+x')} + G_{LL} e^{-ik_F(x-x')}, && (2.11) \\
V(x) &\simeq V_f(x) + V_b(x) e^{2ik_F x} \\
&\quad + V_b^*(x) e^{-2ik_F x}. && (2.12)
\end{aligned}
$$

Define strengths of disorder by

$$
\begin{aligned}
\langle V_f(x) V_f(x') \rangle &= D_f \delta(x - x'), && (2.13a) \\
\langle V_b(x) V_b(x') \rangle &= 0, && (2.13b) \\
\langle V_b(x) V_b^*(x') \rangle &= D_b \delta(x - x'), && (2.13c)
\end{aligned}
$$

where $D_{f/b}$ denotes forward/backward scattering strengths, the self-energy becomes

$$
\begin{aligned}
\Sigma(x, x') &= \delta(x - x') \{ D_f G(x, x') \\
&\quad + D_b \Big[G_{RR} e^{ik_F(3x-3x')} + G_{RR} e^{ik_F(-x+x')} + G_{RL} e^{ik_F(3x-x')} \\
&\quad + G_{RL} e^{ik_F(-x+3x')} + G_{LR} e^{-ik_F(3x-x')} + G_{LR} e^{-ik_F(-x+3x')} \\
&\quad + G_{LL} e^{-ik_F(3x-3x')} + G_{LL} e^{-ik_F(-x+x')} \Big] \}, && (2.14) \\
&\simeq \delta(x - x') \Big\{ D_f G(x, x') + D_b \Big[G_{RR} e^{-ik_F(x-x')} + G_{LL} e^{ik_F(x-x')} \Big] \Big\} && (2.15)
\end{aligned}
$$

where in the last step only terms proportional to $e^{\pm ik_F x}$ are retained. The linearized

36

same-point self-energy is therefore

$$\Sigma_{RR} = D_f G_{RR} + D_b G_{LL}, \tag{2.16a}$$

$$\Sigma_{RL} = D_f G_{RL}, \tag{2.16b}$$

$$\Sigma_{LR} = D_f G_{LR}, \tag{2.16c}$$

$$\Sigma_{LL} = D_f G_{LL} + D_b G_{RR}. \tag{2.16d}$$

When expressed in the chiral Nambu-Gorkov basis $\left(\psi_R, \psi_L, \psi_L^\dagger, \psi_R^\dagger \right)$, we have

$$\Sigma = D_f \tau_3 G \tau_3 + \frac{D_b}{2} \tau_3 \left(\sigma_1 G \sigma_1 + \sigma_2 G \sigma_2 \right) \tau_3. \tag{2.17}$$

With this form of Σ in Eq. (2.9), we now resolve Eq. (2.9) into components with the observation that in the bulk of a clean system g is exactly known to be

$$g_{\text{bulk}} = \frac{-i\omega}{\sqrt{\Delta^2 - \omega^2}} \sigma_3 \tau_3 - \frac{\Delta}{\sqrt{\Delta^2 - \omega^2}} \sigma_0 \tau_2. \tag{2.18}$$

Consider now a situation where $D_{f/b}$ are adiabatically tuned away from zero in the bulk of the wire. By substituting Eq. (2.18) in Eq. (2.9), it can be shown that g can only have six non-zero components:

$$g = g_{31} \sigma_3 \tau_1 + g_{02} \sigma_0 \tau_2 + g_{33} \sigma_3 \tau_3$$

$$+ g_{10} \sigma_1 \tau_0 + g_{21} \sigma_2 \tau_1 + g_{23} \sigma_2 \tau_3, \tag{2.19}$$

and their equations of motions are

$$v_F \partial_x g_{31} = 2\omega g_{02} + 2i\Delta g_{33} + \frac{2i}{\tau} g_{02} g_{33}, \tag{2.20a}$$

$$v_F \partial_x g_{02} = -2\omega g_{31}, \tag{2.20b}$$

$$v_F \partial_x g_{33} = -2i\Delta g_{31} - \frac{2i}{\tau} g_{31} g_{02}, \tag{2.20c}$$

$$v_F \partial_x g_{10} = 2\omega g_{23} - \left(\frac{i}{\tau} - \frac{4i}{\tilde{\tau}}\right)(g_{21} g_{31} + g_{23} g_{33}), \tag{2.20d}$$

$$v_F \partial_x g_{21} = 2i\Delta g_{23} + \left(\frac{3i}{\tau} - \frac{4i}{\tilde{\tau}}\right) g_{02} g_{23} + \left(\frac{i}{\tau} - \frac{4i}{\tilde{\tau}}\right) g_{10} g_{31}, \tag{2.20e}$$

$$v_F \partial_x g_{23} = -2\omega g_{10} - 2i\Delta g_{21} - \left(\frac{3i}{\tau} - \frac{4i}{\tilde{\tau}}\right) g_{02} g_{21} + \left(\frac{i}{\tau} - \frac{4i}{\tilde{\tau}}\right) g_{10} g_{33}, \tag{2.20f}$$

where we have defined $\tau^{-1} = \pi\nu_0 D_b$ and $\tilde{\tau}^{-1} = \pi\nu_0 \frac{1}{2}(D_f + D_b)$. Substituting Eq, (2.19) in Eq. (2.7), we have for the LDOS

$$\nu(x, \omega) = \nu_0 \left(\mathrm{Re} g_{33} - \mathrm{Im} g_{23} \cos 2k_F x\right). \tag{2.21}$$

To completely formulate the problem, Eqs. (2.20) must be supplemented with boundary conditions. In the bulk of the wire ($x \to \infty$), since the BdG Hamiltonian is diagonal in the σ space, the resultant Green function must also be diagonal in the σ-space. This implies that $g_{10} = g_{21} = g_{23} = 0$ at $x \to \infty$. By setting the spatial derivatives of Eq. (2.20) to zero, we also obtain

$$\omega g_{02} + i\Delta g_{33} + \frac{i}{\tau} g_{02} g_{33} = 0, \qquad (2.22\text{a})$$

$$g_{31} = 0, \qquad (2.22\text{b})$$

$$-i\Delta g_{31} - \frac{i}{\tau} g_{31} g_{02} = 0 \qquad (2.22\text{c})$$

at $x \to \infty$.

To derive the boundary conditions at the end of the wire $(x = 0)$, we note that since the fermion operator is linearized as $\psi(x) = \psi_R(x) e^{ik_F x} + \psi_L(x) e^{-ik_F x}$, at the end of wire we have $0 = \psi(0) = \psi_R(0) + \psi_L(0)$. This translates to the requirement that

$$\begin{pmatrix} 1 & 1 & 0 & 0 \\ & & & \\ 0 & 0 & 1 & 1 \end{pmatrix} G(0, \epsilon) = \begin{pmatrix} 0 & 0 & 0 & 0 \\ & & & \\ 0 & 0 & 0 & 0 \end{pmatrix}. \qquad (2.23)$$

Since it follows from the definition of g [Eq. (2.4)] and the Dyson's equation for G [Eq. (2.8)] that $\lim_{\epsilon \to 0^+} G(0, \epsilon) = \frac{1}{2iv_F} g(0) \sigma_3 \tau_3 + \frac{i}{2v_F} \sigma_3 \tau_3$, we have

$$g_{02} = 0, \qquad (2.24\text{a})$$

$$g_{10} = 1, \qquad (2.24\text{b})$$

$$g_{21} = ig_{31}, \qquad (2.24\text{c})$$

$$g_{23} = ig_{33} \qquad (2.24\text{d})$$

at $x = 0$. The last condition is also consistent with the requirement that $\nu(0, \omega) = 0$

[c.f. Eq. (2.21)].

Finally we add that since $g^2 = 1$ in the bulk of a clean system [c.f. Eq. (2.18)] and from Eq. (2.9) we have $\partial_x g^2 = 0$, the normalization $g^2 = 1$ is valid throughout the whole system. Written in its components,

$$g_{31}^2 + g_{02}^2 + g_{33}^2 + g_{10}^2 + g_{21}^2 + g_{23}^2 = 1. \tag{2.25}$$

We make two remarks before closing the discussion on the formalism. First, note that Eqs. (2.20a)-(2.20c) do not contain the variables g_{10}, g_{21}, and g_{23}. Together with the boundary conditions Eqs. (2.22) and Eq. (2.24a), g_{31}, g_{02}, and g_{33} can thus be solved without reference to the other three variables. These equations have been previously derived [69, 74] by first integrating out the fast-oscillating degrees of freedom in the problem, or equivalently [see Eq. (2.5)] by assuming that G is always diagonal in σ-space. We have seen from Eqs. (2.24) that this cannot hold true near the boundary, where the reflection from the end of the wire induces correlations between left- and right-moving modes. Keeping these oscillatory terms, which are always neglected in the usual Eilenberger theory, is crucial since our interest is in figuring out the effect of disorder on the MZMs which reside at the boundaries (i.e., at the wire ends of the 1D system).

It can be seen from Eq. (2.21) that computation of LDOS using g_{33} alone would miss spatially rapid oscillations near the end of the wire. Indeed, it has been pointed out in Ref. [73] that with the reduced set of variables $\{g_{31}, g_{02}, g_{33}\}$, an oscillatory factor ($\propto \cos 2k_F x$) of the LDOS near the end of the wire is not captured. It is

therefore necessary to solve the whole set of equations (2.20) if a spatial resolution of the LDOS under the Fermi wavelength is desired. However, in the following sections in this chapter, we shall only focus on $\{g_{31}, g_{02}, g_{33}\}$ for simplicity.

Lastly we adopt this formalism to the case of conventional s-wave superconductivity, with the linearized Hamiltonian

$$
\begin{aligned}
H_0 \;=\; & \sum_{C,\sigma} \int_0^\infty dx \left[-iv_F s_C \psi_{C\sigma}^\dagger \partial_x \psi_{C\sigma} + \Delta_s \psi_{C\sigma} \psi_{\bar C,\bar\sigma} \right. \\
& \left. + V_f \psi_{C\sigma}^\dagger \psi_{C\sigma} + V_b \psi_{C\sigma}^\dagger \psi_{\bar C,\sigma} \right],
\end{aligned}
\tag{2.26}
$$

where only non-magnetic disorder $V_{f/b}$ is considered here. Repeating the above procedures in solving for $\partial_x g^{(s)}$ and then decomposing $g_s^{(s)}$ as

$$
\begin{aligned}
g^{(s)} \;=\; & g_{01}^{(s)} \sigma_0 \tau_1 + g_{32}^{(s)} \sigma_3 \tau_2 + g_{33}^{(s)} \sigma_3 \tau_3 \\
& + g_{10}^{(s)} \sigma_1 \tau_0 + g_{22}^{(s)} \sigma_2 \tau_2 + g_{23}^{(s)} \sigma_2 \tau_3,
\end{aligned}
\tag{2.27}
$$

we reach the following set of differential equations:

$$v_F \partial_x g_{01}^{(s)} \;=\; 2\omega g_{32}^{(s)} + 2i\Delta_s g_{33}^{(s)}, \tag{2.28a}$$

$$v_F \partial_x g_{32}^{(s)} \;=\; -2\omega g_{01}^{(s)} - \frac{2i}{\tau} g_{01}^{(s)} g_{33}^{(s)}, \tag{2.28b}$$

$$v_F \partial_x g_{33}^{(s)} \;=\; -2i\Delta_s g_{01}^{(s)} + \frac{2i}{\tau} g_{01}^{(s)} g_{32}^{(s)}, \tag{2.28c}$$

$$v_F \partial_x g_{10}^{(s)} \;=\; 2\omega g_{23}^{(s)} - 2i\Delta_s g_{22}^{(s)} - \left(\frac{i}{\tau} - \frac{4i}{\tilde{\tau}}\right)\left(g_{22}^{(s)} g_{32}^{(s)} + g_{23}^{(s)} g_{33}^{(s)}\right), \tag{2.28d}$$

$$v_F \partial_x g_{22}^{(s)} \;=\; 2i\Delta_s g_{10}^{(s)} - \left(\frac{3i}{\tau} - \frac{4i}{\tilde{\tau}}\right) g_{01}^{(s)} g_{23}^{(s)} + \left(\frac{i}{\tau} - \frac{4i}{\tilde{\tau}}\right) g_{10}^{(s)} g_{32}^{(s)}, \tag{2.28e}$$

$$v_F \partial_x g_{23}^{(s)} \;=\; -2\omega g_{10}^{(s)} + \left(\frac{3i}{\tau} - \frac{4i}{\tilde{\tau}}\right) g_{01}^{(s)} g_{22}^{(s)} + \left(\frac{i}{\tau} - \frac{4i}{\tilde{\tau}}\right) g_{10}^{(s)} g_{33}^{(s)}, \tag{2.28f}$$

and the boundary conditions that

$$g_{10}^{(s)} = g_{22}^{(s)} = g_{23}^{(s)} \;=\; 0, \tag{2.29a}$$

$$\omega g_{32}^{(s)} + i\Delta_s g_{33}^{(s)} \;=\; 0, \tag{2.29b}$$

$$-\omega g_{01}^{(s)} - \frac{i}{\tau} g_{01}^{(s)} g_{33}^{(s)} \;=\; 0, \tag{2.29c}$$

$$-i\Delta_s g_{01}^{(s)} + \frac{i}{\tau} g_{01}^{(s)} g_{32}^{(s)} \;=\; 0 \tag{2.29d}$$

at $x \to \infty$ and

$$g_{01}^{(s)} = 0, \tag{2.30a}$$

$$g_{10}^{(s)} = 1, \tag{2.30b}$$

$$g_{22}^{(s)} = ig_{32}^{(s)}, \tag{2.30c}$$

$$g_{23}^{(s)} = ig_{33}^{(s)} \tag{2.30d}$$

at $x = 0$. A normalization condition similar to Eq. (2.25) also holds:

$$\left(g_{01}^{(s)}\right)^2 + \left(g_{32}^{(s)}\right)^2 + \left(g_{33}^{(s)}\right)^2 + \left(g_{10}^{(s)}\right)^2 + \left(g_{22}^{(s)}\right)^2 + \left(g_{23}^{(s)}\right)^2 = 1. \tag{2.31}$$

We observe that $g_{01}^{(s)}$, $g_{32}^{(s)}$, and $g_{33}^{(s)}$ can be solved from Eqs. (2.28a)-(2.28c), Eqs. (2.29b)-(2.29d) and Eq. (2.30a) independent of the remaining components.

2.2   LDOS in the Bulk

Equations (2.20) can be understood as a generalization of the SCBA to spatially inhomogeneous structures. Before we utilize it to investigate into such structures, however, it is instructive to show that our formalism in the bulk indeed reduces to the SCBA result obtained earlier [66].

We first consider the simpler case of an s-wave superconducting wire, for which Eqs. (2.29) and Eq. (2.31) are solved by
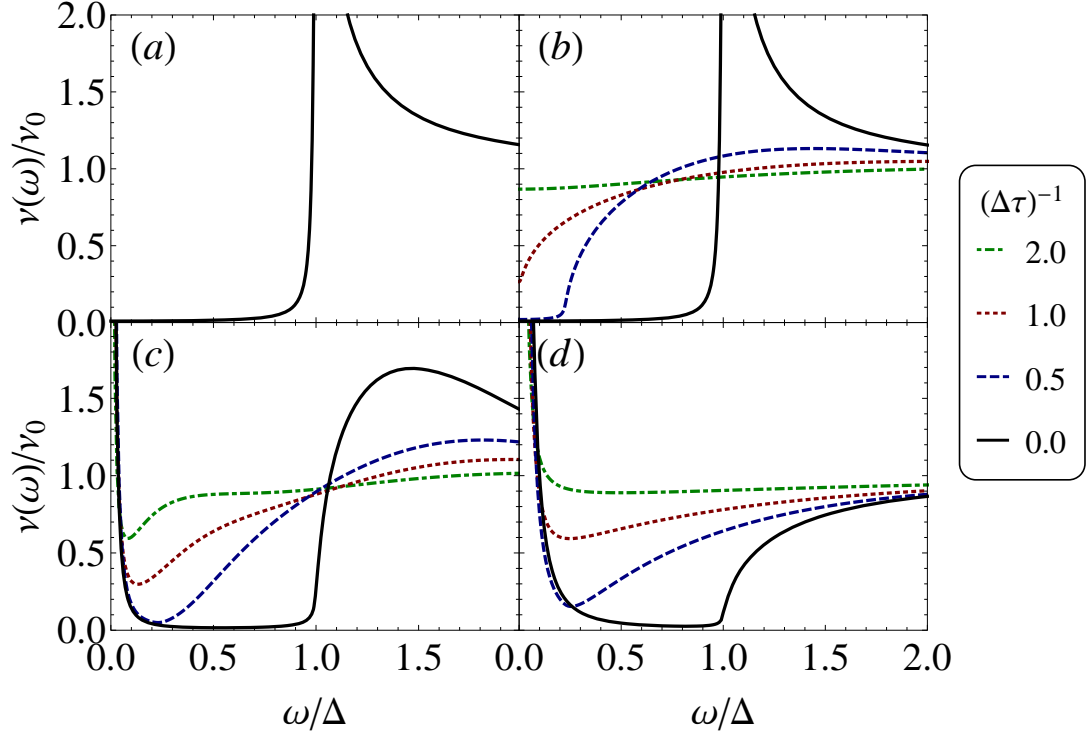
Figure 2.1: (a) LDOS for a semi-infinite s-wave superconducting wire. Note the result is position-independent, and is not affected by disorder. (b)-(d) The LDOS of a semi-infinite p-wave superconducting wire, from the clean limit $\tau^{-1} = 0$ to a heavily disordered case $\tau^{-1} = 2\Delta$ at (b) $x \to \infty$ (in the bulk), (c) $x = \xi_0$, and (d) $x = 0$, respectively. For all plots, the energy spectra are broadened by $\eta = 0.01\Delta$.

$$g_{01}^{(s)} = 0, \tag{2.32a}$$

$$g_{32}^{(s)} = \frac{-\Delta_s}{\sqrt{\Delta_s^2 - \omega^2}}, \tag{2.32b}$$

$$g_{33}^{(s)} = \frac{-i\omega}{\sqrt{\Delta_s^2 - \omega^2}}, \tag{2.32c}$$

independent of the disorder parameter τ. Therefore, in the s-wave case, the LDOS in the bulk is

$$\nu_s(\omega) = \nu_0 \mathrm{Re}\left[g_{33}^{(s)}(\omega)\right] = \nu_0 \frac{\omega}{\sqrt{\omega^2 - \Delta_s^2}} \theta\left(\omega - \Delta_s\right), \tag{2.33}$$

plotted in Fig. 2.1(a), and is unaffected by disorder as required by Anderson's theorem [75].

For the case of p-wave superconducting wire in which Anderson's theorem is not applicable, a suppression of the gap by disorder is expected. To show this, note that Eqs. (2.22) and Eq. (2.25) are solved by

$$g_{31} = 0, \tag{2.34a}$$

$$g_{02} = \frac{-\Delta}{\sqrt{\Delta^2 - \tilde{\omega}^2}}, \tag{2.34b}$$

$$g_{33} = \frac{-i\tilde{\omega}}{\sqrt{\Delta^2 - \tilde{\omega}^2}}, \tag{2.34c}$$

where $\tilde{\omega}$ satisfies $\tilde{\omega} = \omega + \frac{i\tilde{\omega}}{\tau\sqrt{\tilde{\omega}^2 - \Delta^2}}$. This is seen to be identical to the SCBA result of

45

$\tilde{\omega} = \omega + (D_f + D_b) \pi \nu_0 \frac{i\tilde{\omega}}{\sqrt{\tilde{\omega}^2 - \Delta^2}}$, by noting that for point scatterers $D_f = D_b$. Figure 2.1(b) is a plot of the LDOS evaluated by Eq. (2.21), for a number of disorder strengths. The bulk gap is seen to close at about $(\Delta\tau)^{-1} = 1$. In fact, it can be shown that Eq. (2.34) results in a degradation of the spectral gap in the form of [75] $E_{\text{gap}} = \Delta \left[1 - (\Delta\tau)^{-2/3} \right]^{3/2}$, and eventually destroys the gap for $\tau^{-1} > \Delta$. The influence of this effect on the MZM located at the boundary of the wire is the focus of the following sections.

2.3   LDOS Near the End of the Wire

We now investigate the effect of ensemble-averaged disorder on the LDOS near the boundary $x = 0$. Before considering the case of p-wave superconducting wire in which a MZM is present, for the sake of comparison and illustration, we first review the case of a conventional s-wave superconducting wire in the current formalism. We note that the solution in the bulk given by Eq. (2.32) already satisfies the boundary conditions at the end of the wire [Eq. (2.30)]. Therefore, the LDOS is uniform throughout the whole wire, and Fig. 2.1(a) is independent of the distance from the boundary. Thus, as expected, the boundaries of the 1D system or the wire ends do not produce any nontrivial effects for s-wave superconducting wires.

In the more nontrivial case of p-wave superconductor, the solution in the bulk Eq. (2.34) cannot satisfy the boundary condition at the end [Eq. (2.24a)] and thus
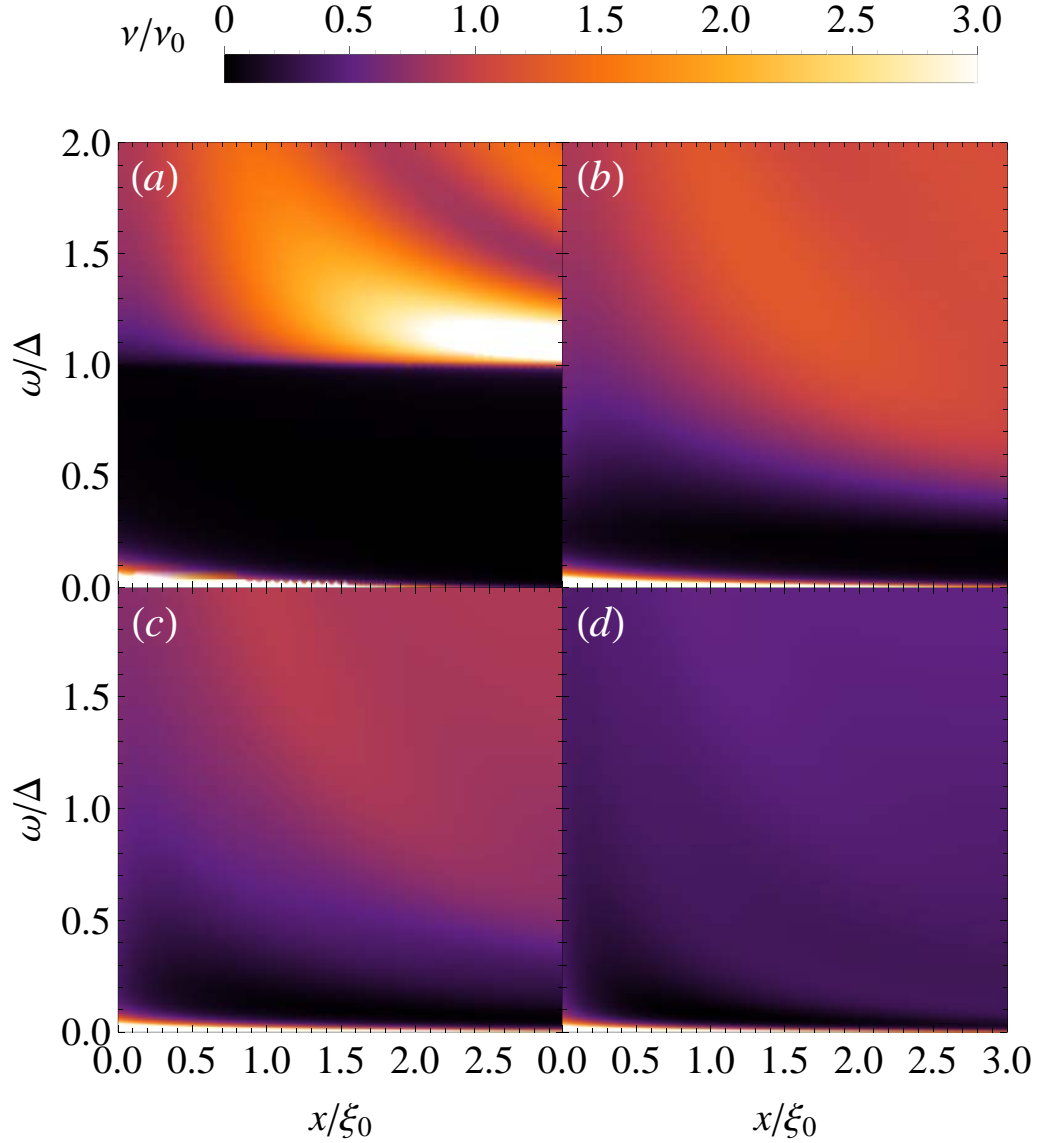
Figure 2.2: The LDOS $\nu(x, \omega, \eta) = \nu_0 \text{Re}\,[g_{33}(x, \omega + i\eta)]$ plotted as a function of position x (in units of $\xi_0 = v_F/\Delta$) and energy ω (in units of Δ), where x is measured from the end of the wire and $\eta = 0.01\Delta$ is the broadening parameter. The four panels correspond to disorder strengths (a) $\tau^{-1} = 0$, (b) $\tau^{-1} = 0.5\Delta$, (c) $\tau^{-1} = \Delta$, and (d) $\tau^{-1} = 2\Delta$. When the system is clean, the salient features are the zero-energy peak localized at the end and a pristine bulk gap. As disorder is introduced, the bulk gap shrinks and the singularity is smeared out, homogenizing the LDOS of the whole system, but the zero-energy peak at the end of the wire is still visible even at strong disorder.

Eqs. (2.20) must be solved directly. Without disorder, the solution is[73]

$$g_{31} = \frac{\Delta e^{-2x\sqrt{\Delta^2-\omega^2}/v_F}}{\omega}, \tag{2.35}$$

$$g_{02} = \frac{\Delta\left(e^{-2x\sqrt{\Delta^2-\omega^2}/v_F} - 1\right)}{\sqrt{\Delta^2 - \omega^2}}, \tag{2.36}$$

$$g_{33} = i\frac{\Delta^2 e^{-2x\sqrt{\Delta^2-\omega^2}/v_F} - \omega^2}{\omega\sqrt{\Delta^2 - \omega^2}}, \tag{2.37}$$

and the other components of g can also be solved analytically but we shall not state them here as we are ignoring variations in the length scale of k_F^{-1}. Note that g_{31} is odd in frequency, indicating an odd-frequency s-wave pairing present near the boundary [73]. The close relation between the odd-frequency pairing and MZMs has been emphasized in the literature [76, 77].

With nonzero disorder, the problem must be solved numerically. Figures 2.1(b)-2.1(d) show the LDOS given by Eq. (2.21), evaluated in the bulk, at $x = \xi_0$ and $x = 0$ for a number of disorder strengths. For the same choice of disorder strengths, the contour plots of the LDOS are shown in Fig. 2.2. In a clean wire, a singularity in LDOS is present at the gap edge ($\omega = \Delta$). This singularity is absent at the end of the wire, where instead a single zero-energy MZM is present. As disorder is introduced, the LDOS throughout the system is homogenized, with the LDOS singularity smoothened and the bulk gap suppressed. As the disorder strength is increased beyond the bulk-gap closing point of $\tau^{-1} = \Delta$, the continuum states begin to hybridize with the MZM, but the zero-bias peak (ZBP) is distinctly visible even under strong disorder of $\tau^{-1} = 2\Delta$, where in the bulk the LDOS becomes almost

flat. It might be of interest to note that at strong disorder a suppression of the LDOS at $\omega \gtrsim 0$ is present only at $x \sim \xi_0$, but is absent either in the bulk or at the end of the wire. This can be understood as the MZM is centered at the end, its hybridization with the continuum states is the strongest there too.

We point out as an aside that the somewhat surprising continued survival of the zero mode even beyond the disorder-induced gap closing point obtained in our current formal semiclassical theory has also been seen in the direct numerical simulations recently [45]. This indicates that the end MZMs are very robust and exist even in the gapless p-wave superconducting phase, which might be consistent with the experimental observations where the ZBP exists even when there is no obvious gap signature in the tunneling spectrum.

2.4 Change of Majorana Localization Length Under Disorder

In a clean system the MZM is exponentially localized with a decay length equal to the coherence length $l_{\mathrm{loc}} = \xi_0 = v_F/\Delta$. One expects disorder to modify this localization length, which should diverge as disorder destroys the topological phase[61]. On the one hand, the suppression of the spectral gap seems to suggest a longer decay length if it is substituted into the formula $l_{\mathrm{loc}} = v_F/E_{\mathrm{gap}}$. On the other hand, in the case of s-wave superconductors, the coherence length of a strongly disordered system is shortened to $\xi_{\mathrm{dis}} \approx v_F\sqrt{\tau/\Delta}$, which suggests a shorter decay length if the formula $l_{\mathrm{loc}} = \xi_{\mathrm{dis}}$ is to be trusted. Equations (2.20) allow for a
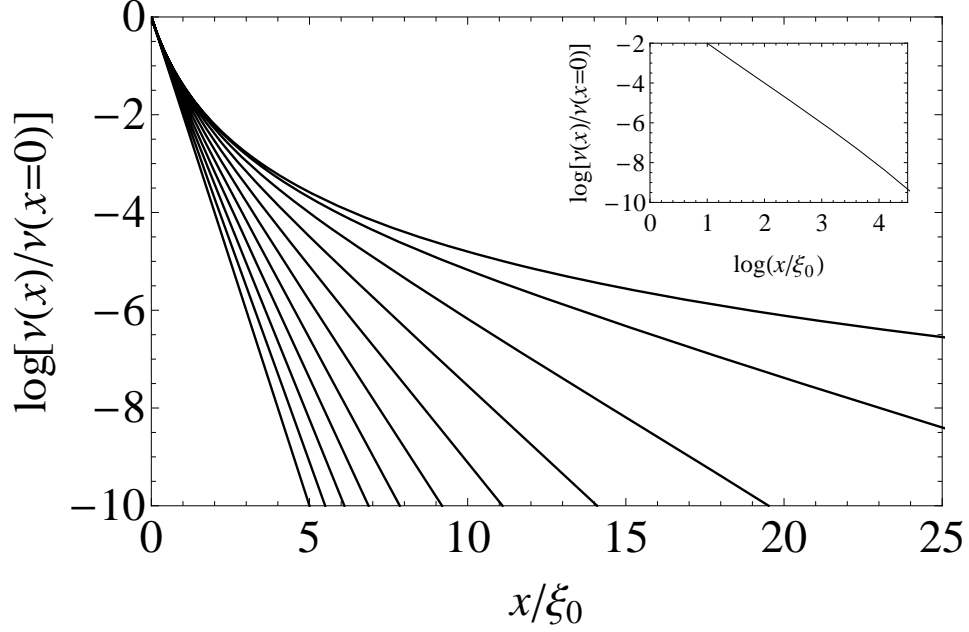
Figure 2.3: Log-linear plot of zero-energy LDOS $\nu\left(x, \omega = 0\right)$ as a function of distance x measured from the end of a p-wave superconducting wire, with oscillations of length scale k_F^{-1} ignored. The steepest line corresponds to clean case $\tau^{-1} = 0$ where the MZM is most localized. The least steep line corresponds to the critical disorder strength $\tau^{-1} = \Delta$ where the bulk gap closes. The intermediate lines are sampled at equally spaced τ^{-1} with a step size of $\delta\left(\tau^{-1}\right) = 0.1\Delta$. The inset shows the last curve corresponding to $\tau^{-1} = \Delta$ in log-log scale. Its slope is approximately -2.

quantitative investigation of the problem.

The decay length is extracted in the following way. The LDOS is related to the Green function by $\nu\left(x, \omega\right) \propto \sum_n \frac{\psi_n(x)\psi_n^*(x)}{\omega - E_n + i\delta}$ where the summation is over all eigenmodes with energies E_n. Therefore, a localized zero-energy MZM with wave function of the form $\sim e^{-x/\xi}$ will result in a decay of the LDOS as $\nu\left(x, \omega = 0\right) \sim e^{-2x/\xi}$, provided that the bulk gap is finite. Note that it is convenient to ignore the fast-oscillating LDOS contributed by g_{23} in Eq. (2.21).

In Fig. 2.3 we plot the the zero-energy LDOS $\nu\left(x, \omega = 0\right)$ in log scale, for a range of disorder strength τ^{-1} up to the critical strength where the bulk gap closes.
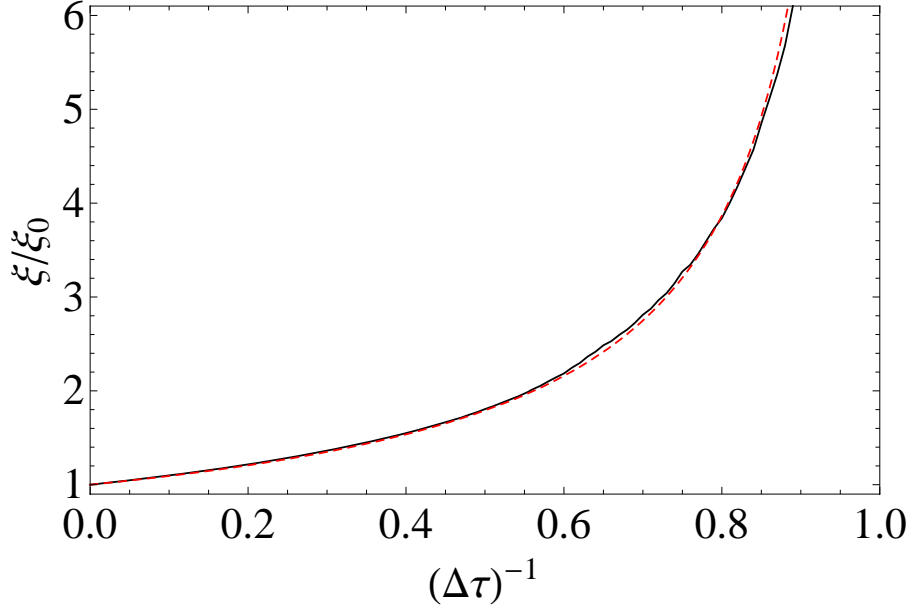
Figure 2.4: Plot of the localization length of the MZM as a function of disorder strength. The black solid line shows the numerical values extracted from Fig. 2.3 by fitting the tails of the curves (at $\log \frac{\nu(x)}{\nu(x=0)} < -6$) with straight lines. Note that the result is meaningful only for weak disorder ($\tau^{-1} \lesssim \Delta$) where the corresponding the curve in Fig. 2.3 is approximately linear. The red dashed line is the best-fit line of a power-law form of $\frac{\xi}{\xi_0} = \left[1 - (\Delta\tau)^{-1}\right]^{-0.84}$.

For the clean limit $\tau^{-1} = 0$, the plot is linear with a slope of $\frac{-2}{\xi_0}$, as expected since the MZM is localized with a decay length of ξ_0. When disorder is increased, the slope decreases in magnitude and the curve deviates from a linear behavior. As the strength is increased to the critical gap-closing value ($\tau^{-1} = \Delta$), the decay ceases to be exponential and becomes power-law in nature, as is clear from the linearity of the curve in the log-log plot shown in the inset of Fig. 2.3. A linear fit through the log-log plot shows that the decay of the ZBP is a power law with a behavior of x^{-1}.

To be more quantitative, the decay length ξ of the MZM could be crudely estimated from Fig. 2.3, in the weak disorder limit (roughly when $\tau^{-1} \lesssim \Delta$) where the curves are approximately linear, by fitting the curves with straight lines. We

compute the slope m of the best-fit line of the tail of each curve in Fig. 2.3 and extract the estimated decay length ξ of the MZM by $\xi \sim \frac{-2}{m}$, with the results shown in Fig. 2.4. For the purpose of completeness, Fig. 2.4 is presented with disorder ranging from zero to the gap-closure limit $(\tau^{-1} = \Delta)$, but it should be cautioned that near the gap-closure limit the notion of "decay length" is meaningless as the decay behavior shows a crossover from exponential to power-law. To understand the nature of the divergence at $\tau^{-1} = \Delta$, we fit the curve with a power-law function and obtain $\frac{\xi}{\xi_0} \simeq \left[1 - (\Delta\tau)^{-1}\right]^{-0.84}$. Figure 2.4 shows that this empirical form captures the variations of decay length very well.

2.5   Leakage of the Majorana Mode

The zero-energy MZM appears to persist even after the gap closes within our formalism. More precisely, the LDOS at the boundary $\nu(x=0,\omega)$ has a pole at $\omega = 0$ for any finite values of Δ and τ. This fact could be derived directly from Eqs. (2.20a)-(2.20c) with a perturbative treatment in Δ in the following way: in the limit $\Delta \ll \tau^{-1}$, we treat Δ as a small perimeter and expand the solution to Eq. (2.20) perturbatively in Δ. For simplicity we shall consider only Eq. (2.20a-c) supplemented with the boundary conditions Eqs. (2.22) and Eq. (2.24a), since the other equations are decoupled and does not affect g_{33} which determines the LDOS.

At $\Delta = 0$ the problem is trivially solved with

$$g_{33}^{(0)} = 1, \tag{2.38a}$$

$$g_{31}^{(0)} = g_{02}^{(0)} = 0. \tag{2.38b}$$

With small Δ, we write $g_J = \sum_{n=0}^{\infty} g_J^{(n)} \Delta^n$ (for $J = \{33, 31, 02\}$) and expand Eq. (2.20) to successive orders in Δ. To the first order in Δ, the system of differential equations is

$$v_F \partial_x g_{31}^{(1)} = 2\omega g_{02}^{(1)} + 2i + \frac{2i}{\tau} g_{02}^{(1)}, \tag{2.39a}$$

$$v_F \partial_x g_{02}^{(1)} = -2\omega g_{31}^{(1)}, \tag{2.39b}$$

$$v_F \partial_x g_{33}^{(1)} = 0, \tag{2.39c}$$

subjected to the boundary conditions of $g_{02}^{(1)}(0) = 0$ and $\lim_{x \to \infty} g_{31}^{(1)}(x) = 0$. This is solved with

$$g_{31}^{(1)}(x) = -\frac{e^{-2xi\sqrt{\omega(\omega+i\tau^{-1})}/v_F}}{\sqrt{\omega(\omega+i\tau^{-1})}}, \tag{2.40a}$$

$$g_{02}^{(1)}(x) = \frac{ie^{-2xi\sqrt{\omega(\omega+i\tau^{-1})}/v_F}}{\omega+i\tau^{-1}} - \frac{i}{\omega+i\tau^{-1}}, \tag{2.40b}$$

$$g_{33}^{(1)}(x) = 0, \tag{2.40c}$$

which has no effect on the LDOS. We must therefore go to the second order which gives

$$v_F \partial_x g_{33}^{(2)} = -2i g_{31}^{(1)} - \frac{2i}{\tau} g_{31}^{(1)} g_{02}^{(1)}, \tag{2.41a}$$

where only the equation for $g_{33}^{(2)}$ is given as it is relevant to the evaluation to LDOS. Requiring $\lim_{x\to\infty} g_{33}^{(2)}(x) = \frac{1}{2(\omega+i\tau^{-1})^2}$ which follows from the expansion of Eq. (2.34c), we have

$$g_{33}^{(2)}(x) = -\frac{ie^{-4ix\sqrt{\omega(\omega+i\tau^{-1})}/v_F}}{2\omega\tau\left(\omega+i\tau^{-1}\right)^2} - \frac{e^{-2ix\sqrt{\omega(\omega+i\tau^{-1})}/v_F}}{\left(\omega+i\tau^{-1}\right)}$$
$$+\frac{1}{2\left(\omega+i\tau^{-1}\right)^2}, \tag{2.42}$$

$$g_{33}^{(2)}(0) \approx \frac{i\tau}{2\omega} - \frac{\tau^2}{2} - \frac{i\omega\tau^3}{2}, \tag{2.43}$$

in which an expansion in ω is performed. We therefore see that the pole at zero energy is present even for $\Delta\tau \ll 1$.

To see clearly the effects of gap closure on the MZM, we perform the following procedure: as we know from the case of the clean wire that the divergence at zero-energy comes from a single MZM, we fit the LDOS near the end of the wire and near zero energy with a Lorentzian form:

$$\nu_\tau(x,\omega,\eta) \sim \frac{1}{2\pi} Z_\tau(x) \frac{\eta}{\omega^2+\eta^2} + \nu_{\text{reg}}, \tag{2.44}$$

where $Z_\tau(x)$ is a the fitting parameter and the subscript τ indicates the dependence on disorder strength. η is an artificial broadening parameter and ν_{reg} is the part of the LDOS that remains non-divergent as $\eta, \omega \to 0$, contributed from the other delocalized modes in the system.

On the other hand, we know that if the LDOS is contributed by a single mode
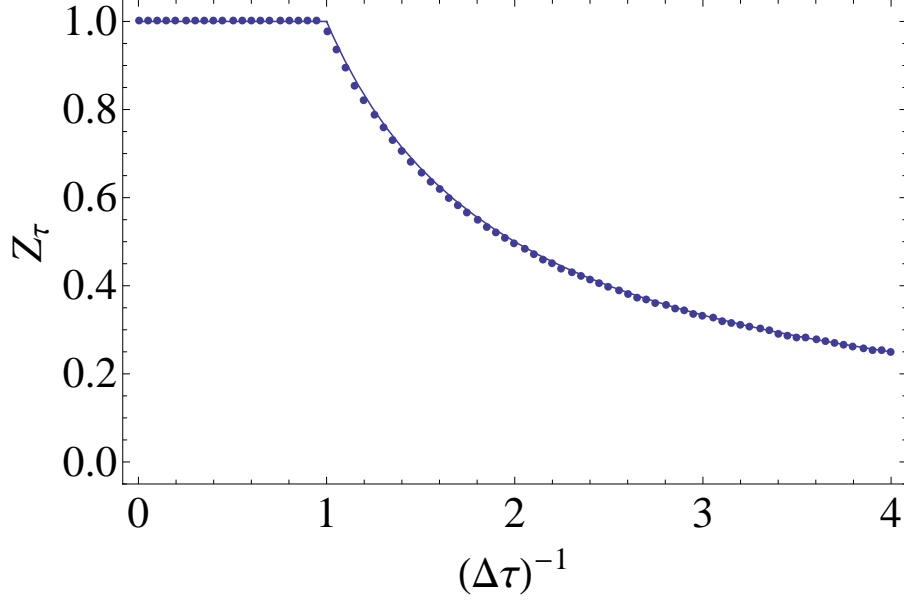
Figure 2.5: Spectral weight Z_τ (defined in the text) of the zero-energy end mode against disorder strength. The dots show the values obtained from the numerical solution of Eqs. (2.20) for a range of disorder strengths. The solid line plots the empirical formula Eq. (2.46).

ψ_0, its exact form is

$$\nu^{(0)}(x,\omega,\eta) = \frac{1}{2\pi} \sum_\lambda |\psi_{0\lambda}(x)|^2 \frac{\eta}{\omega^2 + \eta^2}, \tag{2.45}$$

where the summation Σ_λ is over the four-component BdG spinor. Comparing Eqs. (2.44) and (2.45), it is seen that the spectral weight defined as $Z_\tau = \int_0^\infty Z_\tau(x)\,dx$ is normalized to unity provided that the MZM is not hybridized with other modes.

Figure 2.5 shows the variations of Z_τ as the strength of disorder is changed. For $\Delta\tau \geq 1$, Z_τ remains around unity, which is expected as the bulk gap is not closed and the zero-energy MZM remains exponentially localized and protected by the spectral gap (and therefore of unit spectral weight). As disorder is increased beyond the strength where the bulk gap closes, Z_τ starts to decrease below unity.

This reduction in the spectral weight can be understood as a consequence of the hybridization between the continuum modes in the bulk and the MZM. Interestingly, the dependence of Z_τ on disorder can be captured almost perfectly with the empirical formula

$$Z_\tau = \begin{cases} 1, & \Delta\tau \geq 1 \\ \\ \Delta\tau, & \Delta\tau < 1. \end{cases} \tag{2.46}$$

We note that Eq. (2.46) indicates a continuous decrease of the MZM spectral weight from unity in the topologically gapped situation to a small, but not necessarily vanishingly small, value in the gapless phase. This robustness of the MZM spectral weight even in the presence of fairly strong disorder (which completely closers the bulk topological gap) may be the reason for the existence of the ZBP in nanowires which do not necessarily have very high mobilities or obvious superconducting gaps.

2.6 Conclusion

In this chapter we have derived a theory for a disordered p-wave superconductor in 1D, with the effects of disorder incorporated by SCBA. Our theory is thus the p-wave generalization of the Eilenberger theory to 1D systems with the explicit inclusion of disorder. A brief comparison with previous works is in order. Reference [48] applied the Eilenberger equations to a SOC wire with proximity-induced Zeeman term and superconductivity, but the disorder was introduced *after* the Eilenberger equations were obtained and explicit disorder-averaging was performed numerically.

Ref. [73] adopted the Eilenberger equations to the same system investigated by us, but the emphasis was put on the analysis of the proximity effect, and *no* disorder was introduced. Moreover, short-length-scale fluctuations in the LDOS were explicitly ignored in Reference [73]. Our study differs from these works in that disorder is incorporated by SCBA in the Eilenberger equations, and spatial fluctuations of the LDOS of the order of Fermi wavelength is retained. In fact, the inclusion of both disorder and spatial fluctuations are the main features of our theory distinguishing it from earlier works in the literature.

We applied our formalism to a semi-infinite p-wave superconducting wire, and found that the gap of the system in the bulk is suppressed by disorder in a way consistent with previous studies. We then focused on the MZM located at the end of the wire. We found that with the bulk gap being suppressed, the localization length of the MZM increases, and diverges when the gap vanishes. In this process, the localization behavior of the MZM changes from exponential to a power-law decay. We also pointed out an unusual feature of the MZM under disorder in this formalism: the LDOS shows a divergence at zero-energy at the end of wire even at strong disorder. This is contradictory to the fact that the MZM should hybridize with the continuum modes and its spectrum should broaden. However, we can still extract certain manifestations of this hybridization within this formalism– the spectral weight of the MZM decreases after the bulk gap is closed, showing a "leakage" of the MZM to the continuum. It is interesting that we find that some vestiges ("Majorana ghosts") of the MZMs survive strong disorder and continue showing up in the zero-energy LDOS even when the p-wave system has become

essentially a gapless system due to disorder.

The results from SCBA appear qualitatively consistent with numerical solutions of the LDOS [45] near the end. In these studies the ZBP, which starts as a sharp Majorana peak, decreases in height and broadens out into a peak resulting from Griffiths singularities [61] that is consistent with the class-D symmetry of the system [48]. In contrast to the more exact results where the ZBP is found to broaden into a power-law singularity, we find that the ZBP stays sharp near zero energy while reducing in spectral weight. This discrepancy is not unexpected since the SCBA is a mean-field theory and cannot possibly describe critical fluctuations. Furthermore, we cannot expect to determine a sharp phase transition based on SCBA since SCBA does not describe the localized phase of 1D metals. The disorder-induced topological superconducting phase transition in spinless p-wave superconductors occurs when the superconducting coherence length becomes comparable to the localization length. In summary, SCBA is found to describe qualitatively the suppression of the Majorana ZBP despite the fact that it smears out the phase transition into a crossover from a topological superconducting to a diffusive metallic phase.

Chapter 3

Disorder in Multiband Topological

Insulator-based Heterostructures

One substantive advantage of the TI-based MZM proposals [11, 71, 78] over the SMC-based proposals [5, 13, 6] is that the explicit presence of time-reversal symmetry (TRS). By contrast, the SMC/SC hybrid topological structures hosting MZMs do not have such symmetries and therefore are unprotected from non-magnetic disorder in the environment [see Fig. 3.2(a) for an illustrative example in which the MZM is destroyed by strong disorder]. There has been little theoretical analysis of disorder effects in the TI/SC hybrid structures. One example is Ref. [12] which concluded that TI/SC topological systems are completely protected from *all* elastic disorder effects by virtue of Anderson's theorem [79] due to TRS. A recent study, however, concluded that the induced p-wave superconductivity may in general be suppressed by disorder in a 3D TI/SC structure [80].

In this chapter, we consider the experimental TI/SC structure for the existence of bound MZMs where a FI must be deposited in order to localize the MZMs at the system edge. The realistic structure [Fig. 6.1(a)], first proposed by Fu and Kane in this context [11], involves the 2D TI with SC and FI layers deposited on top of it. The FI layer in the structure breaks TRS which is essential for localizing spatially
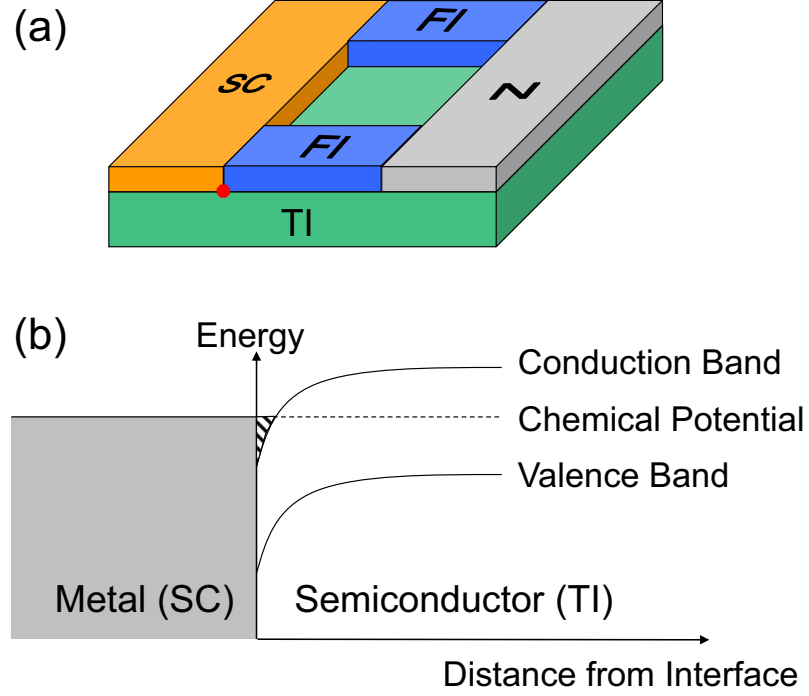
Figure 3.1: (a) Schematic picture of the devices: a TI in contact with SCs and an FI . The position of MZM is marked with a red dot. The normal metal N acts as an external lead and the FI acts as a tunnel barrier. The MZM is then detected as a ZBCP. (b) At the interface between the metallic SC and the narrow-gap SMC (i.e. the TI), in general band-bending at the interface leads to extra edge channels (hashed region).

separated topologically non-Abelian MZMs. The absolute necessity of TRS breaking for creating isolated defect-bound MZMs is a well-established theorem [9].

In this scenario, the immunity of the local SC gap in the TI/SC/FI structure against disorder is subtle. Although Anderson's theorem guarantees that no impurities can degrade the gap deep in the SC region where TRS applies, there is no corresponding argument near the SC/FI interface, where the FI provides an explicit TRS-breaking mechanism that makes the theorem inapplicable. This means that although the MZMs separated by the SC do not hybridize, extra fermionic sub-gap states could potentially appear locally at the SC/FI interface in the TI/SC/FI hybrid structure.

In spite of this, we find that disorder in the SC region of the TI edge is unable to generate any extra localized fermionic subgap states (i.e. in addition to the zero-energy MZM itself) near the SC/FI interface [see Fig. 3.2(d)], provided that we limit our attention only to single-channel TI edges. Thus, the TI/SC/FI hybrid system is indeed immune to all disorder provided there is only a single active edge channel in the system. However, disorder-induced potential fluctuations near the edge are expected to produce bound states in addition to the 1D edge state. Such extra states or puddles, which have been proposed to explain the temperature dependence of the TI edge conductance [81], can be modeled using a multi-channel TI edge. In fact, in realistic structures, we expect multi-channel 1D edges in the generic 2D TI system due to, for example, band-bending effects which are ubiquitous near SMC surfaces.

3.1 Model

We investigate a broad class of TI Hamiltonians by considering a multi-channel TI edge. In addition to disorder, the extra 1D edge channels could be induced from an intrinsically higher chemical potential near the surface [82, 83]. Also, since the 2D TI is commonly constructed from SMC with small band gaps (e.g. HgCdTe or InAs/GaSb) [84, 85], a proximate metallic SC would unavoidably induce extra edge channels due to band-bending [86] [see Fig. 6.1(b)].

We consider the following Hamiltonian which models a multi-channel TI edge in proximity to SC/FI:

$$
\begin{aligned}
H = \int dx \bigg\{ &v \sum_{\alpha s s'} (\boldsymbol{p}_\alpha \cdot \boldsymbol{\sigma}_{ss'}) \, \psi_{\alpha s}^\dagger(x) \, (-i\partial_x) \, \psi_{\alpha s'}(x) \\
&- \sum_{\alpha \beta s} \mu_{\alpha\beta}(x) \psi_{\alpha s}^\dagger(x) \psi_{\beta s}(x) \\
&- \sum_{\alpha \beta i s s'} \tilde{\mu}_{\alpha\beta}^j(x) \imath \sigma_{ss'}^j \psi_{\alpha s}^\dagger(x) \psi_{\beta s'}(x) \\
&+ \sum_{\alpha} \Delta_\alpha(x) \left[\psi_{\alpha\uparrow}(x) \psi_{\alpha\downarrow}(x) + \mathrm{hc} \right] \\
&+ \sum_{\alpha s s'} B_\alpha(x) \sigma_{ss'}^x \psi_{\alpha s}^\dagger(x) \psi_{\alpha s'}(x) \bigg\}
\end{aligned}
\tag{3.1}
$$

Here, $\psi_{\alpha s}^\dagger(x)$ creates an electron in the αth channel with spin $s = \uparrow, \downarrow$ at position x, where each "channel" has a Kramers pair of bands. Note that the nature of TI edge requires the number of channels N_{ch} to be odd. $\boldsymbol{\sigma} = (\sigma^x, \sigma^y, \sigma^z)$ are the three Pauli spin matrices, and $\boldsymbol{p}_\alpha$ is the polarization of the αth channel. The $N_{\mathrm{ch}} \times N_{\mathrm{ch}}$

real symmetric matrix $\mu_{\alpha\beta}(x)$ contains both the chemical potential of each channel (diagonal entries) and inter-channel elastic scattering (off-diagonal entries), while the anti-symmetric matrix $\tilde{\mu}_{\alpha\beta}^{j}(x)$ are the coefficients for inter-channel spin-orbit scatterings, which still respect TRS. The proximate SC and FI induce the local pairing potential $\Delta(x)$ and the Zeeman term $B(x)$ respectively. To model an SC/FI interface, we choose $\Delta(x) = \Delta\theta(x)$ and $B(x) = B\theta(-x)$ where $B = 3\Delta$, restricting the analysis to an idealized case where there are no spatial fluctuations of Δ and B on the edge [58] and no penetration of Δ and B to the FI and SC side, respectively, since this would degrade the spectral gap at the SC/FI interface in a trivial way and obscure our main findings. We also assume that there are no inter-channel pairings or Zeeman gaps.

Static charge impurities and spin-orbit impurities are included through spatial variations in $\mu(x)$ and $\tilde{\mu}(x)$, respectively. For the results below in which disorder is included, the mean free path l is estimated to be $k_F l \approx 3$. If the disorder in either μ or $\tilde{\mu}$ is removed, the phase space of scattering is reduced, but similar results would still apply provided that the mean free path remains the same by tuning up $\tilde{\mu}$ or μ respectively. Note that disorder is introduced in the SC region only since its effect on the FI region can in principle be offset by a sufficiently strong Zeeman term.

3.2   Scattering Matrix Approach

Before presenting the results based on numerical simulations, we first analyze the problem with a scattering matrix approach [62, 42]. We treat the SC/FI interface

as an SC-N-FI system where the N region has a finite but vanishingly small width.
A solution in N is

$$\psi^\dagger = u_+ \psi_+^\dagger + u_- \psi_-^\dagger + v_- \psi_- + v_+ \psi_+, \qquad (3.2)$$

in which the multi-component $\psi_\pm$ are Kramer's pairs and the subscripts $\pm$ represents right/left moving modes. The corresponding particle-hole-conjugated and time-reversed solutions are:

$$\mathcal{C}\psi^\dagger\mathcal{C}^{-1} \;=\; v_+^* \psi_+^\dagger + v_-^* \psi_-^\dagger + u_-^* \psi_- + u_+^* \psi_+ \qquad (3.3)$$

$$\mathcal{T}\psi^\dagger\mathcal{T}^{-1} \;=\; -u_-^* \psi_+^\dagger + u_+^* \psi_-^\dagger + v_+^* \psi_- - v_-^* \psi_+ \qquad (3.4)$$

Reflection matrices R relates the coefficients of $\left(\psi_+^\dagger, \psi_+\right)$ to those of $\left(\psi_-^\dagger, \psi_-\right)$. At the left (SC/N) interface, the particle-hole symmetry and time-reversal symmetry are both respected, giving three equations for R:

$$\begin{pmatrix} u_+ \\ v_+ \end{pmatrix} \;=\; R \begin{pmatrix} u_- \\ v_- \end{pmatrix} \qquad (3.5)$$

$$\begin{pmatrix} v_+^* \\ u_+^* \end{pmatrix} \;=\; R \begin{pmatrix} v_-^* \\ u_-^* \end{pmatrix} \qquad (3.6)$$

$$\begin{pmatrix} -u_-^* \\ -v_-^* \end{pmatrix} \;=\; R \begin{pmatrix} u_+^* \\ v_+^* \end{pmatrix}, \qquad (3.7)$$

from which one can derive

64

$$R = \tau_x R^* \tau_x = -R^T. \tag{3.8}$$

Together with the unitarity condition $R^\dagger R = 1$, the value of $\det R$ could be computed. First note that the constraint $R = \tau_x R^* \tau_x$ requires R to take the form

$R = \begin{pmatrix} r_{ee} & r_{eh} \\ r_{eh}^* & r_{ee}^* \end{pmatrix}$, while the condition $R = -R^T$ implies that r_{ee} is antisymmetric,

and, since its dimension is odd, it is singular. Since R itself is non-singular (by the unitarity condition), this implies that r_{eh} is invertible. The remaining conditions $R^\dagger R = 1$ implies

$$r_{eh}^\dagger r_{ee} + r_{ee}^T r_{eh}^* = 0 \quad \Rightarrow \quad r_{ee} r_{eh}^{*-1} = -r_{eh}^{\dagger -1} r_{ee}^T \tag{3.9}$$

$$r_{eh}^\dagger r_{eh} + r_{ee}^T r_{ee}^* = 1 \quad \Rightarrow \quad r_{ee}^T r_{ee}^* = 1 - r_{eh}^\dagger r_{eh} \tag{3.10}$$

$$\tag{3.11}$$

Now we evaluate $\det R$:

$$
\begin{aligned}
\det R &= (-1)^{N_{\rm ch}} \det \begin{pmatrix} r_{eh} & r_{ee} \\ r_{ee}^* & r_{eh}^* \end{pmatrix} \\
&= (-1)^{N_{\rm ch}} \det \left(r_{eh}^* r_{eh} - r_{eh}^* r_{ee} r_{eh}^{*-1} r_{ee}^* \right) \\
&= -\det \left(r_{eh}^* r_{eh}^{\dagger -1} \right) \tag{3.12} \\
&= -1 \tag{3.13}
\end{aligned}
$$

where we have utilized the fact that r_{eh} is invertible and Eqs. (3.9, 3.10) are consec-

65

utively used in the intermediate steps. $N_{\text{ch}} = \dim R/2$ is the number of channels in the model, which is restricted to be odd due to the nature of the TI edge.

At the right (N/FI) interface we have no Andreev reflection or time-reversal symmetry, constraining the form of $\tilde{R}$ to be $\tilde{R} = \begin{pmatrix} \tilde{r}_{ee} & 0 \\ 0 & \tilde{r}_{ee}^* \end{pmatrix}$. By the unitarity of $\tilde{R}$, we have $\det \tilde{R} = 1$.

The zero-energy modes are found by solving $\det \left(1 - \tilde{R}R \right) = 0$, which implies that the multiplicity of the eigenvalue -1 of $-\tilde{R}R$ gives the number of zero-energy modes. We now prove that $-\tilde{R}R$ must have at least one eigenvalue being -1. To this end we rotate R to the Majorana basis via $\Omega = \frac{1}{\sqrt{2}} \begin{pmatrix} 1 & 1 \\ -i & i \end{pmatrix}$:

$$\Omega R \Omega^\dagger = 2 \begin{bmatrix} \text{Re}\,(r_{ee} + r_{eh}) & -\text{Im}\,(r_{ee} - r_{eh}) \\ \text{Im}\,(r_{ee} - r_{eh}) & \text{Re}\,(r_{ee} - r_{eh}) \end{bmatrix} \tag{3.14}$$

This matrix is real and, because it is unitary, it is also orthogonal. Similarly for $\tilde{R}$ and hence $-\tilde{R}R$. The eigenvalues of an orthogonal matrix can only be 1, -1, or pairs of conjugate $e^{\pm i\phi}$. Since $\det \left(-\tilde{R}R \right) = -1$, $-\tilde{R}R$ must have *at least* one eigenvalue being -1. On the other hand, because there are no other constraints on the problem, there could be *at most* N_{ch} eigenvalues being -1, and hence, at most N_{ch} zero modes. In summary, $1 \leq N_0 \leq N_{\text{ch}}$, where N_0 is the number of localized zero-energy modes.

The exact value of N_0 depends on the details of the Hamiltonian, but one can always fine-tune the Hamiltonian near the SC/FI interface by local disorder

respecting the symmetries, such that all energies of the localized modes reach zero. Therefore the constraint derived above implies that the number of localized states is equal to the number of channels in the TI edge, and among them there is always a zero-energy mode, which is the MZM.

We have therefore shown that the gap protecting the MZM is indeed robust in the single-channel case. This is not a consequence of Anderson's theorem as commonly believed, but is due to the various symmetries present in the system as elucidated by the above scattering matrix argument. Note that in the multi-channel case, although subgap states exist, the MZM is still pinned at zero energy.

3.3 Numerical Results

In the following we numerically study how the number of subgap states N_0 depends on the number of channels and other details of the interface. We start by considering the simplest case of a TI/SC/FI interface where the TI has a single channel. The LDOS [87, 88] at the SC/FI interface with or without disorder is plotted respectively in Fig. 3.2(c,d). It shows that the LDOS in the subgap regime $(E < \Delta)$ is not affected by disorder in the single-channel case. Fig. 3.2(b) shows that the gap deep in the SC region is also completely unaffected. This is consistent with previous results [12] and our scattering matrix analysis for the single-channel case. This simplification, however, disappears as soon as the system has multichannel edge states as is likely in realistic samples (Fig. 3.3).

To understand the interplay of disorder and multiple channels, we consider
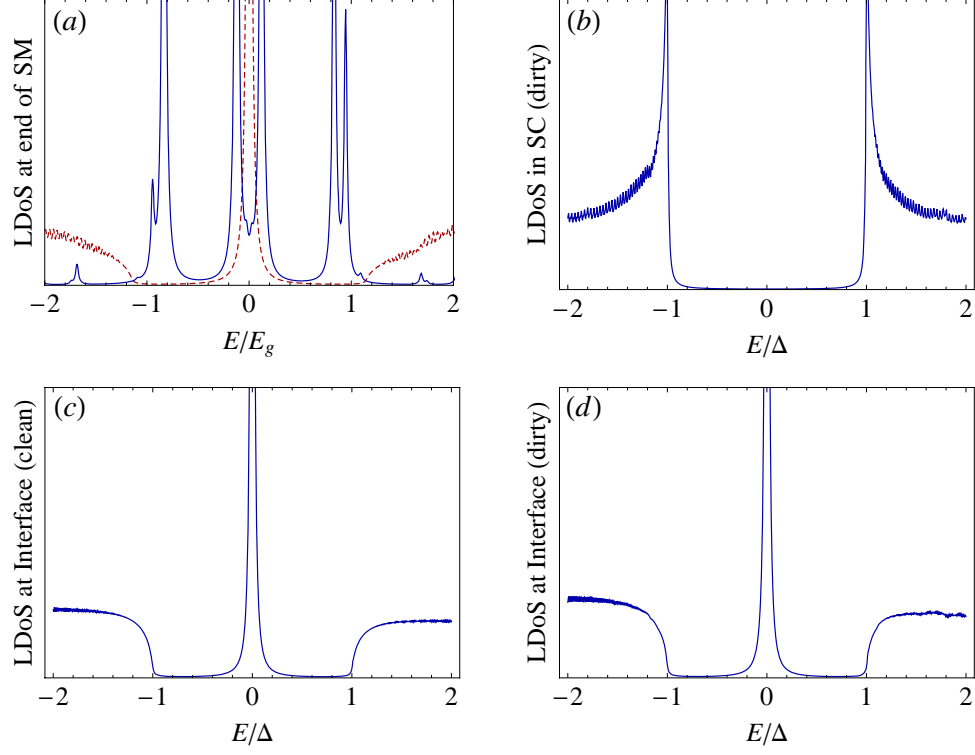
Figure 3.2: (a) LDOS at the end of a SMC nanowire, where the dashed red line shows the result for a clean wire while the solid blue line is for a disordered wire. The parameters used for the BdG Hamiltonian $H = (\frac{p^2}{2m} + \alpha p \sigma_y - \mu)\tau_z + B\sigma_z + \Delta\tau_x$ are: $\mu = 0$, $B = 2\Delta$, $m\alpha^2 = 2\Delta$. (b) LDOS deep in the SC region of the TI edge, with disorder in SC region. (c) LDOS at the SC/FI interface on a clean TI. (d) LDOS at the SC/FI interface on a TI edge with disorder in SC region.
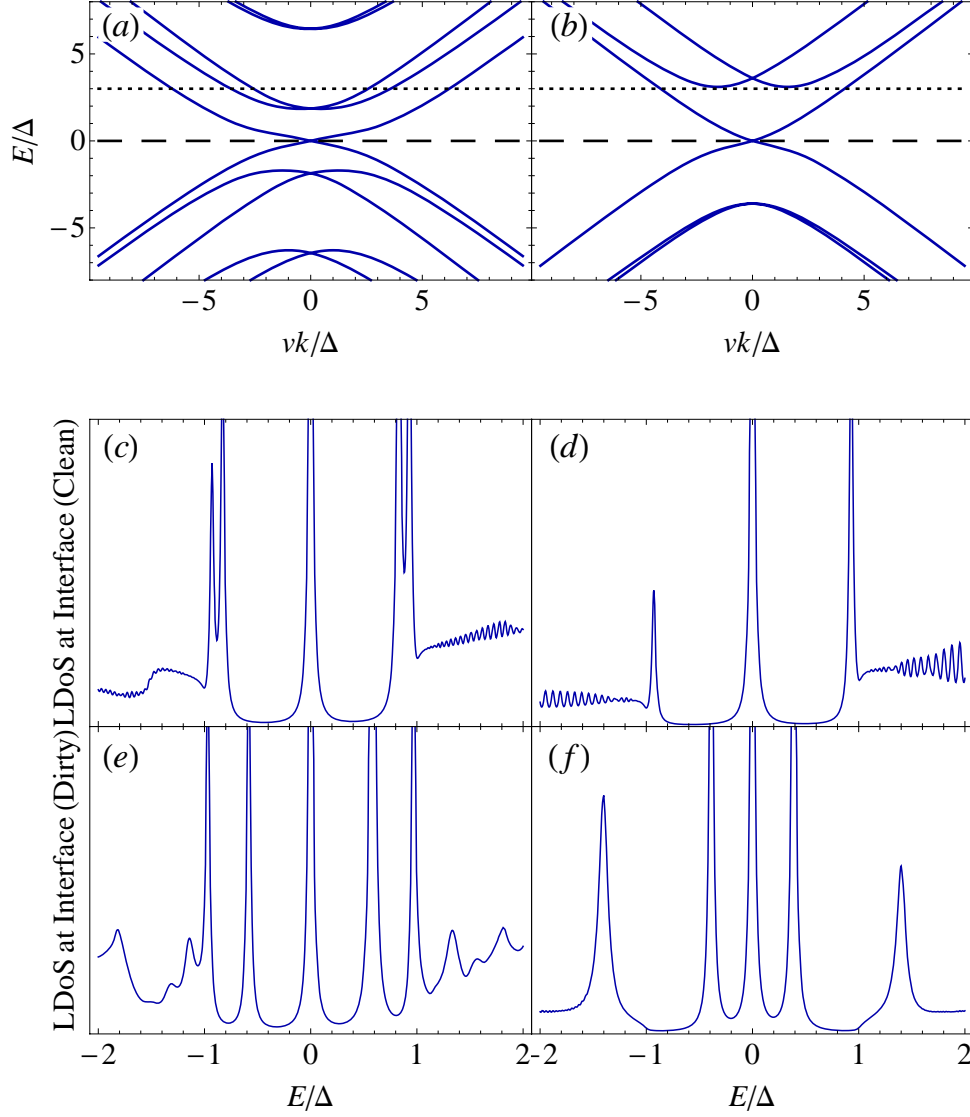
Figure 3.3: (a,b) Band structures of respectively a 5-channel and 3-channel TI edge. Here the parameters of Eq. (3.1) is chosen as: $\mu = \mathrm{diag}\,(2, -2, 1, -1, 0)\,\Delta$, $\tilde{\mu}^x = \tilde{\mu}^y = 0$, $\tilde{\mu}^z_{\alpha \gtrless \beta} = \pm 2\Delta$, $\boldsymbol{p}_\alpha = (+, -, +, -, +)\,\hat{z}$. The Fermi level in the FI region ($E_F = 0$) is shown in dashed line, while that in the SC region ($E_F = 3\Delta$) is shown in dotted line. (c,d) Their corresponding LDOS of at the SC/FI interface, without disorder. (e,f) Their corresponding LDOS at the SC/FI interface, with a single realization of non-magnetic disorder.

5-channel and 3-channel TI edge models. The parameters of Eq. (3.1) are so chosen so that the additional channels cross the Fermi level in the SC region. It is assumed that the FI region is gated so as to place the chemical potential in the gap of the additional bands as well [see Fig. 3.3(a,b)]. This is necessary to obtain localized MZMs at the interface. The LDOS at the interface for several cases are plotted in Fig. 3.3(c,d,e,f). We typically find that each channel leads to a subgap state. The LDOS in Figs. 3.3(c,d) show that for the interface parameters chosen, the interface states are close to the edge of the gap away from the interface. On the other hand, introducing disorder leads to the results in Figs. 3.3(e,f), where one sees interface states that are bound deep inside the bulk gap. The details of the SC/FI interface, such as the chemical potential change at the interface, can lead to scattering very similar to disorder effects. Therefore, depending on the details of the interface it is possible even for an interface without any explicit quenched disorder to have subgap states in the middle of the gap. The results plotted in Figs. 3.3(c,d) correspond to a smooth interface where such scattering is absent and therefore do not contain deep subgap states. In contrast to the interface LDOS, the LDOS in the SC region, away from the SC/FI interface, does not show any subgap states similar to the single channel case. This could be understood as a consequence of TRS, by which the application of Anderson's theorem forbids such subgap states.

Comparing the results of the disordered SC/FI interface in the single channel case (Fig. 3.2) and the multi-channel case (Fig 3.3) it is clear that the absence of subgap states in the single channel case is not simply a result of Anderson's theorem (i.e. TRS). As mentioned in the introduction, since TRS is locally broken at the

interface, it only protects the bulk, i.e. the region away from the SC/FI interface, from subgap states. On the other hand, the scattering-matrix interpretation implies that the presence of a single subgap state in the single channel case is a result of the properties of the scattering matrix near zero energies. Time-reversal invariance does of course play a role in determining the properties of the scattering matrix. The scattering matrix picture also allows for the presence of extra subgap states in the multi-channel case as seen in Fig. 3.3.

The results in Fig. 3.3 are for a typical (rather than fine-tuned) structure of the interface (which is determined by the potentials in the various channels) and also for typical disorder configurations and should thus be regarded as typical results which should be qualitatively valid generically. While these results clearly establish the generic existence of fermionic subgap states in a multi-channel TI with disorder, the experimentally relevant question might be the likelihood of the occurrence of these subgap states with a random disorder potential. To address this question we calculate the disorder-averaged LDOS at the interface (Fig. 3.4). As seen from Fig. 3.4(a,b), the superconducting gap at the SC/FI interface is not protected against disorder and is reduced by increasing disorder strength. Interestingly, the disorder-averaged LDOS for strong disorder is found to vanish at zero energy. This suggests that level repulsion from the MZM prevents the extra subgap states from approaching precise zero-energy which is consistent with conclusions from random matrix theory [89, 63, 90]. In Fig. 3.4(c,d) we show the disorder-averaged gap in the TI/SC edge away from the SC/FI interface. In contrast to the gap near SC/FI interface, we find that the TI/SC gap is immune to disorder as expected since TRS
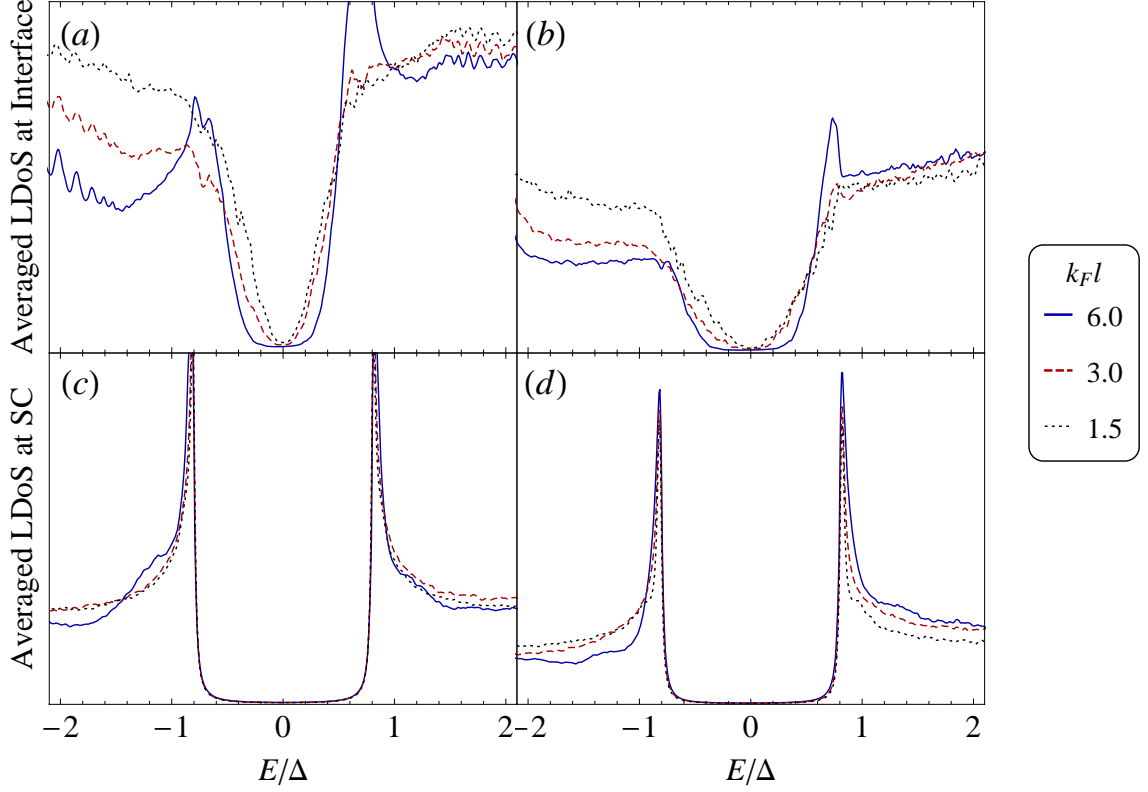
Figure 3.4: (a,b) LDOS at the SC/FI interface, averaged over 5000 realizations of non-magnetic disorder, for a 5-channel and 3-channel TI edge respectively. The three curves show the results for different strengths of disorder, and the MZMs have been removed for clarity (c,d) Their corresponding averaged LDOS deep in the SC region.

is respected there and Anderson's theorem applies. It is instructive to note that the LDOS at the interface [Fig. 3.4(a),(d)] shows precisely the same soft gap behavior widely observed in the SMC/SC nanowire hybrid systems [58, 55].

3.4 Discussion and Conclusion

The additional subgap states may have consequences for detecting and manipulating MZMs at finite temperatures. One of the simplest signatures of an MZM is the ZBCP. The voltage resolution of a tunneling conductance measurement, which

directly probes the LDOS, is limited by the finite tunneling rate and temperature. Low-energy subgap states as in Fig. 3.3 and Fig. 3.4 would contribute to tunneling if the energy of the subgap states is lower than either the temperature or the tunneling-induced broadening. However, since there is a repulsion of these states from zero energy [Fig. 3.4(a,b)], the likelihood for the states to influence the zero-bias conductance is small unless the temperature is high and the number of channels is large. Thus, the zero-bias effective MZM tunneling conductance peak may survive the existence of fermionic subgap states. For utilizing the MZM for topological quantum computation, it is known that extra localized states do not affect the phase of manipulation [91]. However, the additional subgap levels could have an influence for the readout schemes that rely on measuring single-particle spectra [92], because this requires eliminating the TR-breaking region to hybridize the two MZMs to finite energies. In spite of this, the TI/SC structure has an advantage in regards to robustness against disorder, since disorder cannot degrade the SC gap deep in the SC region (if this happens, the two MZMs at the ends would hybridize and becomes regular Fermionic mode). Also, the potential-fluctuation-induced subgap states show a repulsion from zero energy, without any complications arising from weak antilocalization [44, 45].

Experimentally, the conductance of a TI edge was measured as $2e^2/h$ [85], which might appear to contradict our assumption of multiple edge channels. However, the simple relation $N_{\mathrm{ch}} = \frac{G}{(2e^2/h)}$ between conductance G and the number of channels N_{ch} is valid in the clean limit only. With disorder, the conductance should be analyzed using random matrix theory of the edge transmission matrix

[93]. Since the multi-channel TI edge belongs to the symplectic class with an odd number of channels, only one channel remains delocalized [94]. A conductance measurement with a length scale greater than the localization length would then produce $G = 2e^2/h$ even if many channels are present. Therefore, the conductance measurement alone cannot rule out the presence of multiple channels.

To conclude this chapter, we have studied the effects of multiple channels and disorder near an SC/FI interface on the edge of a 2D TI in the context of MZM in the system. We find that a number of localized states, equal to the number of channels, appears at the SC/FI interface. One of these states is the zero-energy MZM while the energies of the other states depend on the specific details of the system. Adding disorder in the SC region leads to a distribution in the energies of these extra localized states, potentially reaching the subgap regime. However their effect is less detrimental than those in the SMC/SC nanowire structures since they are repelled from zero energy and are localized at the boundary.

Chapter 4

Soft superconducting gap in semiconductor Majorana nanowires

An ubiquitous feature of all Majorana experiments involving proximity-induced superconductivity has remained ignored in the literature despite a great deal of activity in the field: the measured $G(V)$ is extremely "soft" in both the high-field topological phase (where the ZBP exists) and in the zero-field or the low-field trivial phase (where there is no ZBP). In fact, the soft gap feature, which is clearly a property of the SMC-SC hybrids quite independent of the MZM physics, is prominent in the data with the subgap conductance being typically only a factor of 2-3 lower than the above-gap conductance, implying the existence of rather large amount of subgap states whose origin remains unclear. We believe that without a thorough understanding of this ubiquitous soft gap, our knowledge of the whole subject remains incomplete.

In this Chapter, we develop a minimal theoretical model that may generally explain the soft gap that is observed ubiquitously in the current Majorana experiments [7, 51, 52, 54]. We systematically consider the effects due to: (a) non-magnetic and (b) magnetic disorder in the nanowire; (c) temperature; (d) dissipative quasiparticle broadening arising due to various pair-breaking mechanisms such as poisoning,

coupling to other degrees of freedom (e.g. phonons or normal electrons in the leads) or due to electron-electron interactions; and (e) inhomogeneities at the SC-nanowire interface due to imperfections (e.g. roughness and barrier fluctuations) that may arise during device fabrication. Since the soft gap occurs universally in the experiment at all parameter values, we consider only the non-topological zero-magnetic field situation here because this is where the gap should be the largest and the hardest. We solve our model numerically by exact diagonalization of the Hamiltonian, and complement the study using the Abrikosov-Gor'kov formalism [95] for a simplified model of a SMC nanowire with a spatially-fluctuating pairing potential.

Our results point to the inhomogeneities at the SMC-SC interface [i.e. mechanism (e)] as the main physical mechanism producing the soft gap. This indicates that improving the quality of the SC-SMC interface should result in a harder induced gap and in a simpler physical interpretation of the Majorana experiment. However, our conclusions are not restricted to Majorana nanowires and might be useful for a correct interpretation of the experimental results in many SMC-SC hybrid systems.

4.1   Theoretical Model

We consider a 1D SMC nanowire of length L_x placed along the x-axis and subjected to SOC, Zeeman field along its axis, and proximity-induced s-wave pairing due to a proximate bulk SC.

Discretization of the Hamiltonian in the continuum results in a tight-binding

model defined on a N_x-site lattice [96],

$$\hat{H}_w = -t \sum_{\langle ij \rangle, s} c_{is}^{\dagger} c_{js} + i\alpha \sum_{i,ss'} \left[c_{is}^{\dagger} \sigma_{ss'}^y (c_{i+1s'} - c_{i-1s'}) \right]$$

$$- \sum_{i,ss'} c_{is}^{\dagger} \left[\mu_i - B_Z \sigma^x - \boldsymbol{b}_i \cdot \boldsymbol{\sigma} \right] c_{is'} + \sum_i \left[\Delta_i c_{i\uparrow}^{\dagger} c_{i\downarrow}^{\dagger} + \text{h.c.} \right]. \quad (4.1)$$

Here, $c_{is}^{\dagger}$ creates an electron with spin $s = \uparrow, \downarrow$ at site i, $\alpha = \alpha_R/2a = \sqrt{E_{so}t}$ parametrizes the Rashba SOC strength, where $E_{so} = m_e^* \alpha_R^2/2$ is the SOC energy scale, α_R is the Rashba velocity and a is the lattice constant. B_Z is the Zeeman energy, and $\boldsymbol{\sigma} = (\sigma_x, \sigma_y, \sigma_z)$ is the vector of Pauli matrices. We use for the nanowire $L_x = N_x a = 2\mu\text{m}$, $m_e^* = 0.015 m_e$, $E_{so} = 50\mu\text{eV}$, and temperature $T = 70\text{mK}$ [7]. We assume a one-band model with $N_x = 500$, $t = 676\mu\text{eV}$, and $\alpha = 0.07t$.

Static non-magnetic disorder in the nanowire is included through a fluctuating chemical potential $\mu_i = \mu_0 + \delta\mu_i$ around the average value μ_0. Static magnetic disorder may be present in the sample due to contamination with magnetic atoms or due to the presence of regions in the nanowire acting as quantum dots with an odd number of electrons. Here, we neglect the quantum dynamics of the impurity spins and model its effect as a randomly oriented inhomogeneous magnetic field $\boldsymbol{b}_i$ [97].

The effects of the proximate bulk SC on the nanowire are modeled in Eq. (4.1) by an effective *locally*-induced *hard* gap Δ_i. The locality of the induced pairing interaction is justified because the coherence length of the bulk SC is typically much shorter ($\xi_{\text{SC}} \approx 3\text{nm}$ in NbTiN alloys) than the Fermi wavelength of the SMC

nanowire ($\lambda_F \approx 10^2$nm). The assumption of an induced hard gap is justified if the SC-nanowire interface is in the tunneling regime. This seems to be a reasonable assumption since the experimentally reported induced gaps are much smaller than the parent bulk SC gaps [7, 51, 52], a fact that typically occurs in low-transmittance interfaces [98, 99, 96] (As a word of caution, the experimental evidence for this identification is still limited and other explanations cannot be completely ruled out). In the tunneling regime, the quantity $\gamma_i = \rho_0 t_{\perp,i}^2 \ll \Delta_{\mathrm{SC}}$, where ρ_0 is the LDOS of electrons in the nanowire at the Fermi energy in the normal phase, $t_{\perp,i}$ is the local tunneling matrix element at the nanowire-SC interface at site i, and Δ_{SC} the bulk parent gap in the SC. Then, the bulk SC is known to induce a hard gap in the nanowire, $\Delta_i \approx \gamma_i$ [98, 96]. A more general treatment of the SC-nanowire interface that takes into account higher orders in $t_{\perp,i}$ (i.e., highly transparent interfaces) is outside the scope of this thesis, and we refer the reader to the well-known bibliography on the subject [100, 101, 102].

Inhomogeneities at SMC-SC interfaces are known to occur generically due to sample fabrication procedures, and their effects have been extensively studied (see e.g. Refs. [103, 101]). In our model, we take into account these inhomogeneities through local spatial fluctuations in $t_{\perp,i}$, which effectively give rise to spatial fluctuations in the induced s-wave SC pairing Δ_i in Eq. (4.1). We assume $t_{\perp,i} = t_\perp^0 e^{-\kappa \delta d_i}$, where δd_i denotes the fluctuation in the width of the nanowire-SC barrier and κ is a phenomenological constant with units of inverse length that parametrizes the energy barrier of the nanowire-SC interface. Such a functional form is expected due to fluctuations in the overlap of evanescent wavefunctions. Then, the induced SC pairing

is $\Delta_i = \Delta_0 e^{-2\delta\beta_i}$, where the dimensionless parameter $\delta\beta_i = \kappa\delta d_i$ characterizes the roughness of the interface, and Δ_0 is the induced SC pairing in the absence of the interface inhomogeneity (we take the value $\Delta_0 = 250\mu eV$ from Ref. [7]). Note that our model for interface fluctuations is generic and only incorporates the inevitable presence of potential fluctuations at the interface separating the SC metal and the nanowire.

The different disorder mechanisms are taken into account by introducing Gaussian-distributed random variables $\delta\mu_i$, $\boldsymbol{b}_i = (b_i^x, b_i^y, b_i^z)$, and $\delta\beta_i$ with zero means and variances given by $\langle\delta\mu_i\delta\mu_j\rangle = W_\mu^2\delta_{ij}$, $\langle b_i^p b_j^q\rangle = W_b^2\delta_{ij}\delta_{pq}$, and $\langle\delta\beta_i\delta\beta_j\rangle = W_\beta^2\delta_{ij}$, respectively. To model the interface inhomogeneity, we coarse-grain the interface in patches of length $5a$ and assume that $\delta\beta_i$ is uniform within each patch, but varies randomly from patch to patch with a standard deviation of W_β. Note that assuming a Gaussian distribution in $\delta\beta_i$ results in a different probability distribution function for Δ_i

$$P(\Delta_i) = \frac{1}{2\Delta_i\sqrt{2\pi}W_\beta}\exp\left[-\frac{1}{8W_\beta^2}\ln^2\left(\frac{\Delta_i}{\Delta_0}\right)\right]. \tag{4.2}$$

The relevant experimental quantity is the tunneling differential conductance $G(V)$ at an end of the nanowire, which is related to the LDOS [7, 51, 52, 104]. We calculate $G(V)$ using the tunneling formalism by coupling the nanowire to a contact lead [105, 13, 41]. The Hamiltonian of the combined system is $\hat{H} = \hat{H}_w + \hat{H}_L + \hat{H}_t$, where $\hat{H}_L = \sum_{ks}\varepsilon_k d_{ks}^\dagger d_{ks}$ is the Hamiltonian describing the lead and $\hat{H}_t = t_L\sum_{ks}d_{ks}^\dagger c_{1s} + \text{h.c.}$ is the tunneling Hamiltonian coupling site $i = 1$ of the nanowire to the lead via a tunneling matrix element t_L. The tunneling conductance

at site $i = 1$ reads

$$G\left(V, T\right) = -2\pi e^2 t_L^2 \rho_L \int_{-\infty}^{\infty} d\omega \rho_1^w\left(\omega\right) f'\left(\omega - eV\right),\tag{4.3}$$

where $f\left(x\right)$ is the Fermi distribution function, ρ_L is the lead density of states at the Fermi energy, and V is the voltage at which the lead is biased with respect to μ_0. Here, $\rho_1^w\left(\omega\right)$ is the LDOS in the nanowire (including both spin projections) at site $i = 1$ in the presence of the lead, which we calculate as $\rho_i^w\left(\omega\right) = -\frac{1}{\pi}\text{Im}\, g_{ii}^w\left(\omega\right)$. Here $g_{ij}^w\left(\omega\right)$ is the retarded Green's function of the nanowire in real-space representation, which in the limit $t_L \to 0$ becomes

$$g_{ij}^w\left(\omega\right) = \sum_{ns} \frac{u_{is,n}^{(0)*} u_{js,n}^{(0)}}{\omega - E_n^{(0)} + i\gamma_{L,n}} + \frac{v_{is,n}^{(0)*} v_{js,n}^{(0)}}{\omega + E_n^{(0)} + i\gamma_{L,n}},\tag{4.4}$$

with $E_n^{(0)}$ and $\{u_{is,n}^{(0)}, v_{is,n}^{(0)}\}$ being, respectively, the eigenvalues and eigenvectors resulting from the diagonalization of the BdG Hamiltonian corresponding to Eq. (4.1). To include the presence of the lead, we solve the equation of motion for $g_{ij}^w\left(z\right)$ in the presence of $\hat{H}_t$ [106]. The term $\gamma_{L,n}$ is the self-energy, which in the limit $t_L \to 0$ becomes $\gamma_{L,n} = -i\pi\rho_L t_L^2 \sum_s \left(|u_{1s,n}^{(0)}|^2 + |v_{1s,n}^{(0)}|^2\right)$.

4.2   Numerical Results

We now present the numerical results for $G\left(V\right)$.   We use $\mu_0 = -338\mu\text{eV}$, and set the temperature to $T = 70\text{mK}$ [7] unless otherwise stated. In Fig. 4.1(a) we present the effect of static disorder on $G(V)$. We take $W_\mu = 0$ (blue curve) to
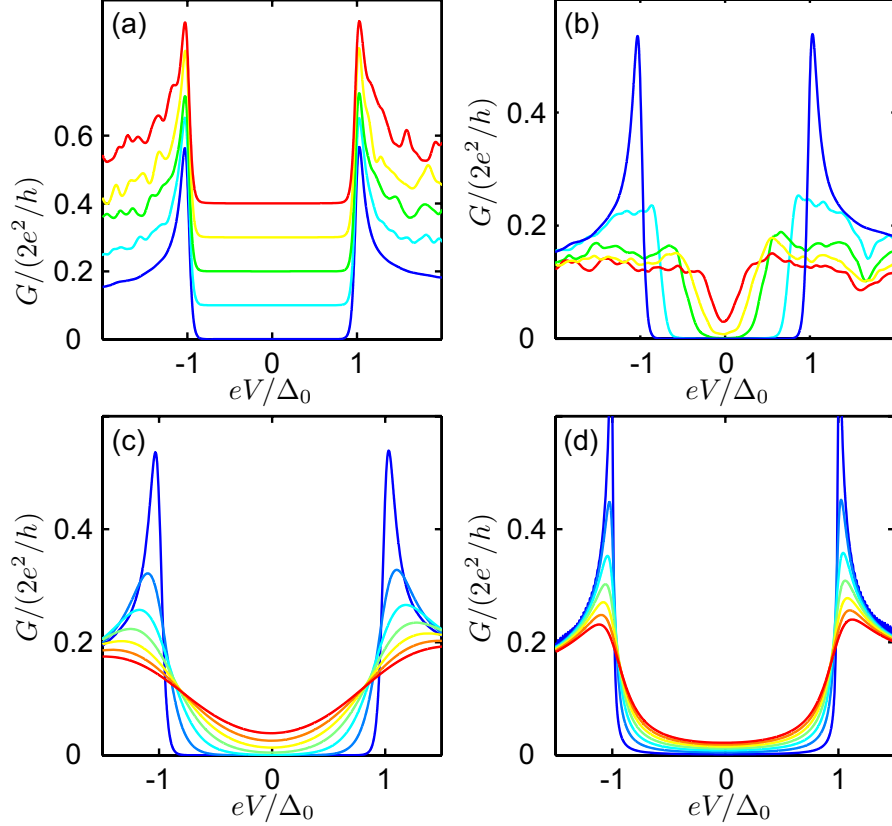
Figure 4.1: Differential conductance for electron tunneling into an end of the SMC nanowire for $B_Z = 0$. Various pair-breaking mechanisms are considered: (a) static disorder, (b) magnetic disorder, (c) temperature and (d) quasiparticle broadening.

$W_\mu = 0.8\Delta_0$ (red curve) in equal steps of $0.2\Delta_0$. The plots are offset in steps of 0.1 for clarity. As expected from Anderson's theorem [79, 97], our results show that the subgap density of states is not affected by the presence of static non-magnetic disorder, thus rendering this an unlikely mechanism for the observed subgap conductance. We note as an aside that in our numerical results for the topological phase, which are not shown here, the effect of non-magnetic disorder is stronger than in the zero magnetic field non-topological phase since Anderson's theorem does not apply in the topological phase. In fact, the non-magnetic disorder in the topological phase behaves very similarly to the magnetic disorder in the non-topological phase

discussed below.

The effect of magnetic disorder is shown in Fig. 4.1(b). We have taken $W_b = 0$, $0.27\Delta_0$, $0.54\Delta_0$, $0.68\Delta_0$ and $0.81\Delta_0$ (blue to red curves). In this case, we find a substantial modification in the subgap conductance. In particular, a soft superconducting gap, similar to the one observed in Ref. [7], is obtained for $W_b = 0.81\Delta_0$ (red curve). According to the Abrikosov-Gor'kov theory [95, 97], the amount of magnetic disorder needed to produce a soft gap is $\Delta_0 \tau_b \sim 1$, where $\tau_b = 2t^2(1 - (\mu/2t)^2)/3v_F W_b^2$ is estimated from our tight binding parameters. Such a large amount of magnetic disorder is unlikely to be present in the nanowire used in the experiments.

The thermal pair-breaking effect is considered in Fig. 4.1(c) [c.f. Eq. (4.3)]. We vary the temperature from $T = 0.027\Delta_0$ (blue curve) to $T = 0.35\Delta_0$ (red curve) in equal steps of $0.054\Delta_0$ [$0.027\Delta_0 \approx 78$mK]. Although a considerable amount of thermally-induced subgap conductance is obtained for $T = 0.35\Delta_0$ (red curve), this value is much larger than the reported experimental temperature $T_{\exp} = 70$ mK, and cannot by itself explain the experimental features. We note that the blue curve corresponds to $T = 78$mK $\gtrsim T_{\exp}$, for which there is no appreciable subgap conductance.

In Fig. 4.1(d), we consider the effect of a finite quasiparticle broadening by introducing a shift in the frequency $\omega \rightarrow \omega + i\gamma_N$ in Eq. (4.4), where γ_N is a phenomenological quasiparticle broadening. This broadening can in principle arise due to coupling of electrons in the nanowire to a source of dissipation, e.g. presence of (unconsidered) normal contacts, quasiparticle poisoning due to tunneling of normal
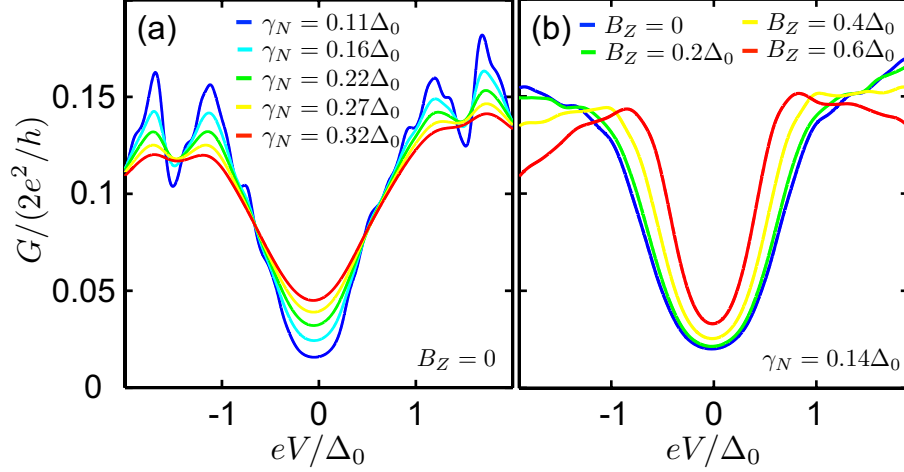
Figure 4.2: Differential tunneling conductance in the presence of SC-nanowire interface inhomogeneity and quasiparticle broadening. In (a), we use $W_\beta = 0.8$ and fix $B_Z = 0$. In (b), we vary B_Z while fixing γ_N, and model interface inhomogeneity via a spatially fluctuating $\Delta_i = \Delta_0 + \delta\Delta_i$, with a Gaussian-distributed random component obeying $\langle \delta\Delta_i \delta\Delta_j \rangle = W_\Delta^2 \delta_{ij}$ and $W_\Delta = 0.2t$. Disorder average is done over 50 and 500 samples in (a) and (b), respectively.

electrons into the nanowire, and scattering with phonons and/or other electrons. Quasiparticle lifetime effects were considered in a similar way in the context of BCS superconductors by introducing a phenomenologically broadened density of states $\rho(\omega, \gamma_N) = \mathrm{Re}\big[(|\omega| + i\gamma_N)/[(|\omega| + i\gamma_N)^2 + \Delta_0^2]^{1/2}\big]$ [107]. In Fig. 4.1(d) we vary γ_N from $\gamma_N = 0.027\Delta_0$ (blue curve) to $\gamma_N = 0.35\Delta_0$ (red curve) in equal steps of $0.054\Delta_0$. We see that even for the largest values of γ_N (i.e. $\gamma_N \sim 0.35\Delta_0$ corresponding to the red curve), a remnant of the hard SC gap is still present. Therefore, this effect alone is incapable of explaining the substantial gap softening observed in the experiments.

While all of the above-mentioned mechanisms are likely to be present to some extent in a realistic setup, our results indicate that it is unlikely that they can individually explain the experimentally observed soft gap. Moreover, even after

combining all the effects of non-magnetic and magnetic disorder, quasiparticle decay rate of order $0.1\Delta_0$, and temperature of 70mK, we found that obtaining a soft gap that qualitatively agrees with experiments requires magnetic disorder strength of $\Delta_0 \tau_b \sim \mathcal{O}(1)$, which seems to be unrealistic. This leads us finally to the effect of inhomogeneities at the nanowire-SC interface (see Fig. 4.2). We now argue that a reasonable amount of interface inhomogeneity, together with quasiparticle broadening, gives a soft gap that is in good qualitative and semi-quantitative agreement with the experimental findings, thus rendering the combination of these two effects as the most likely candidate for the soft gap. In Fig. 4.2(a), we take $W_\beta = 0.8$ while fixing $B_Z = 0$ and varying γ_N as indicated. We observe a large amount of subgap contributions, with a noticeable "v-shaped" tunneling conductance around $V = 0$. We see that $\gamma_N \sim 0.1\Delta_0$ is sufficient to obtain a soft gap reminiscent of the experimental findings [7, 51, 52, 54]. The v-shaped soft gap is obtained only in the presence of both the interface fluctuations and quasiparticle broadening, and an unrealistic magnitude for either of these pair-breaking mechanisms is needed to reproduce the soft gap in the absence of the other. In Fig. 4.2(b), we show the effect of finite magnetic fields (in the non-topological regime) at fixed $\gamma_N = 0.14\Delta_0$. Here, we model the interface inhomogeneity via a spatially fluctuating $\Delta_i = \Delta_0 + \delta\Delta_i$, with a Gaussian-distributed random component obeying $\langle \delta\Delta_i \delta\Delta_j \rangle = W_\Delta^2 \delta_{ij}$ and $W_\Delta = 0.2t$. Realistic experimental temperature of $T = 70$mK has almost no effect on the results of Fig. 4.2.

An order-of-magnitude estimate for the dimensionless parameter $\delta\beta_i$ can be obtained based on known experimental parameters. The width of the nanowires
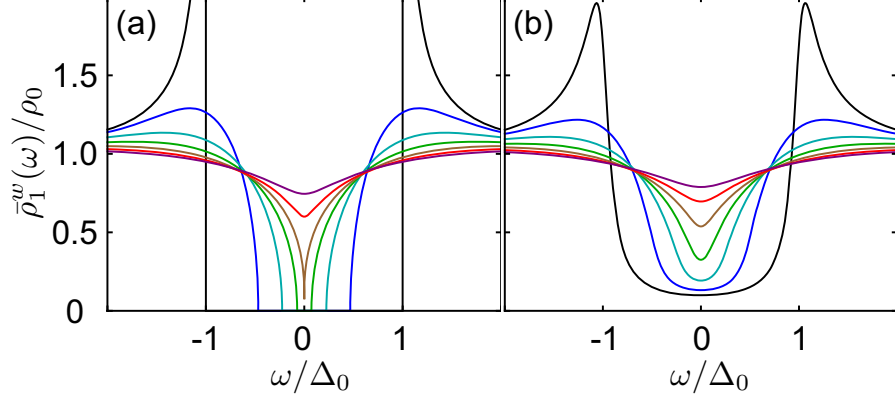
Figure 4.3: Analytical results for $\bar{\rho}_1^w(\omega)/\rho_0$, the averaged LDOS obtained from an Abrikosov-Gor'kov theory for various values of $\Delta_0\tau_\Delta$, and (a) $\gamma_N = 0$ and (b) $\gamma_N = 0.11\Delta_0$.

used in Ref. [7] was quoted as 100nm $\pm$ 10nm. Assuming that the fluctuations in the SC-nanowire barrier width is of order the wire width fluctuations, we take $\delta d_i \approx$ 5nm. The phenomenological barrier parameter κ can be estimated using the interface energy barrier U_0 via $\kappa \approx \sqrt{2m_e^* U_0}/\hbar$. Using an estimate for U_0 based on a Nb-InGaAs junction [108], we take $U_0 \approx 0.2$ eV. With an effective mass for the InSb wire, $m_e^* \approx 0.015 m_e$, we obtain $\delta\beta_i \sim 1$. This order of magnitude estimate is consistent with the standard deviation $W_\beta = 0.8$ used in this thesis.

4.3 Analytical Results

A minimal analytical model that provides an insight into the effects of a fluctuating SC pairing on $G(V)$ can be obtained from the continuum model corresponding to Eq. (4.1) in the absence SOC, Zeeman field and other types of disorder, and assuming the SC pairing *itself* to be a Gaussian variable $\Delta(x) = \Delta_0 + \delta\Delta(x)$ with variance $\langle \delta\Delta(x)\delta\Delta(x') \rangle = W_\Delta^2 \delta(x - x')$. We use the theoretical framework of the

Abrikosov-Gor'kov (AG) theory [95, 97] to obtain the *averaged* electron Green's function $\bar{g}_{ij}^w(\omega)$.

Let us consider the Dyson's equation for the Green function in the presence of fluctuating pairing potential:

$$
\begin{aligned}
G_{kk'} &= G_k^{(0)}\delta_{kk'} + \sum_p G_k^{(0)} V_{kk'} G_{k'}^{(0)} \\
&\quad + \sum_p G_k^{(0)} V_{kp} G_p^{(0)} V_{pk'} G_{k'}^{(0)} \tag{4.5} \\
&\quad + \sum_{pp'} G_k^{(0)} V_{kp} G_p^{(0)} V_{pp'} G_{p'}^{(0)} V_{p'k'} G_{k'}^{(0)} + \dots \tag{4.6}
\end{aligned}
$$

where $G_k^{(0)} = (z\tau_0 - \xi_k\tau_3 - \Delta_0\tau_1)^{-1}$ is the Green function for the superconducting wire with uniform Δ_0, and $V_{kp} = (\delta\Delta)_{k+p}\tau_1$ is the fluctuation in pairing potential. τ_i are the Pauli matrices acting on the particle-hole space. If we consider a Gaussian white noise for Δ_0:

$$
\langle \delta\Delta_k \rangle = 0 \tag{4.7}
$$

$$
\langle \delta\Delta_k \delta\Delta_{k'} \rangle = W_\Delta^2 \delta_{k,-k'} \tag{4.8}
$$

then the fluctuation-averaged Green function can be evaluated with cumulant expansion:

$$
\begin{aligned}
\bar{G}_k \delta_{kk'} &= G_k^{(0)}\delta_{kk'} + \sum_p G_k^{(0)} \tau_1 G_p^{(0)} \tau_1 G_{k'}^{(0)} \langle \delta\Delta_{kp} \delta\Delta_{pk'} \rangle \\
&\quad + \sum_{pp'} G_k^{(0)} \tau_1 G_p^{(0)} \tau_1 G_{p'}^{(0)} \tau_1 G_{p'}^{(0)} \tau_1 G_{k'}^{(0)} \\
&\quad \times \langle \delta\Delta_{kp} \delta\Delta_{pp'} \delta\Delta_{p'p''} \delta\Delta_{p''k'} \rangle + \dots \tag{4.9}
\end{aligned}
$$

$$
\begin{aligned}
\bar{G}_k &= G_k^{(0)} + W_\Delta^2 G_k^{(0)} \tau_1 \left(\sum_p G_p^{(0)} \right) \tau_1 G_{k'}^{(0)} \\
&\quad + W_\Delta^4 G_k^{(0)} \tau_1 \left(\sum_p G_p^{(0)} \right) \tau_1 G_k^{(0)} \tau_1 \left(\sum_p G_p^{(0)} \right) \tau_1 G_{k'}^{(0)} \\
&\quad + W_\Delta^4 G_k^{(0)} \tau_1 \left(\sum_{pp'} G_{k-p}^{(0)} \tau_1 G_{k-p-p'}^{(0)} \tau_1 G_{k-p}^{(0)} \right) \tau_1 G_k^{(0)} \\
&\quad + W_\Delta^4 G_k^{(0)} \tau_1 \left(\sum_{pp'} G_{k-p}^{(0)} \tau_1 G_{k-p-p'}^{(0)} \tau_1 G_{k-p'}^{(0)} \right) \tau_1 G_k^{(0)} \\
&\quad + \ldots \\
&\equiv G_k^{(0)} + G_k^{(0)} \Sigma_k \bar{G}_k \tag{4.10}
\end{aligned}
$$

Note that this expression is formally exact, provided we include all higher order processes. We now consider the following approximation for the self-energy: $\Sigma_k = W_\Delta^2 \int \frac{dp}{2\pi} \tau_1 \bar{G}_p \tau_1$. This corresponds to the "non-crossing approximation" where terms like $\left(\sum_{pp'} G_{k-p}^{(0)} \tau_1 G_{k-p-p'}^{(0)} \tau_1 G_{k-p'}^{(0)} \right)$ are ignored. This is a good approximation if $k_F v_F \tau_\Delta \gg 1$, where $\tau_\Delta^{-1} = \pi W_\Delta^2 \rho_0$ is the scattering rate and ρ_0 is the density of states at the Fermi point for the wire with uniform Δ.

For notational convenience we rewrite the fluctuation-averaged Green function as

$$
\begin{aligned}
\bar{G}_k &= \left(z\tau_0 - \xi_k \tau_3 - \Delta_0 \tau_1 - \Sigma \right)^{-1} \\
&= \left(\tilde{z}\tau_0 - \tilde{\xi}_k \tau_3 - \tilde{\Delta}\tau_1 \right)^{-1} \tag{4.11}
\end{aligned}
$$

where $\tilde{z} = z - \Sigma_0$, $\tilde{\xi}_k = \xi_k + \Sigma_3$ and $\tilde{\Delta} = \Delta_0 + \Sigma_1$. Here the self energy is split

into its components: $\Sigma = \Sigma_0 \tau_0 + \Sigma_3 \tau_3 + \Sigma_1 \tau_1$.

The self-energy can be readily evaluated as

$$
\begin{aligned}
\Sigma_k &= W_\Delta^2 \int \frac{dp}{2\pi} \frac{\tilde{z} + \tilde{\Delta}\tau_1}{\tilde{z}^2 - \xi_p^2 - \tilde{\Delta}^2} \\
&= \frac{-1}{2\tau_\Delta} \frac{\tilde{z} + \tilde{\Delta}\tau_1}{\sqrt{\tilde{\Delta}^2 - \tilde{z}^2}}
\end{aligned}
\tag{4.12}
$$

Substituting this expression into Eq. (4.11) yields the renormalization of the energy and pairing potential:

$$
\tilde{z} = z + \frac{1}{2\tau_\Delta} \frac{\tilde{z}}{\sqrt{\tilde{\Delta}^2 - \tilde{z}^2}}
\tag{4.13}
$$

$$
\tilde{\Delta} = \Delta_0 - \frac{1}{2\tau_\Delta} \frac{\tilde{\Delta}}{\sqrt{\tilde{\Delta}^2 - \tilde{z}^2}}
\tag{4.14}
$$

The density of states in the presence of pairing potential fluctuation is obtained by

$$
\begin{aligned}
\rho(\epsilon) &= \frac{-1}{\pi} \mathrm{Im} \int \frac{dk}{2\pi} \mathrm{Tr}\bar{G}(z \to \epsilon + i0) \\
&\approx \rho_0 \mathrm{Im} \frac{u}{\sqrt{1 - u^2}} \\
&= \rho_0 \left(\Delta_0 \tau_\Delta \right) \mathrm{Im}\, u
\end{aligned}
\tag{4.15}
$$

where we have defined $u \equiv \tilde{z}/\tilde{\Delta}$ and the relation $\frac{z}{\Delta_0} = u \left(1 - \frac{(\Delta_0 \tau_\Delta)^{-1}}{(1-u^2)^{1/2}} \right)$ is used in

the last step. The gap in the quasiparticle spectrum is the smallest ω at which u

acquires an imaginary part. For the function $z(u)$ for real u, the maximum value of

z, beyond which u becomes complex, is [75]:

$$E_{\text{gap}} = \theta \left[\Delta_0 \tau_\Delta - 1 \right] \Delta \left(1 - \left(\Delta_0 \tau_\Delta \right)^{-2/3} \right)^{3/2} \tag{4.16}$$

To compute the LDOS near the end of a semi-infinite wire, we introduce an impurity $V_{\text{imp}} = U \delta(r) \tau_3$ at $r = 0$ of a infinite wire. Taking the limit $U \to \infty$ will cut the wire into two halves. Consider now the Dyson's equation for the fluctuation-averaged Green function in the presence of the impurity:

$$\begin{aligned}
\bar{G}_{\text{imp}}(r, r) &= \bar{G}(r, r) + \bar{G}(0, r) U \tau_3 \bar{G}_{\text{imp}}(0, r) \\
\bar{G}_{\text{imp}}(0, r) &= \bar{G}(0, r) + \bar{G}(0, 0) U \tau_3 \bar{G}_{\text{imp}}(0, r) \\
&= \left[1 - \bar{G}(0, 0) U \tau_3 \right]^{-1} \bar{G}(0, r) \\
\therefore \bar{G}_{\text{imp}}(r, r) &= \bar{G}(0) + \bar{G}(r) \tau_3 \left[U^{-1} - \bar{G}(0) \tau_3 \right]^{-1} \bar{G}(-r)
\end{aligned}$$

where $\bar{G}(r) = \int \frac{dk}{2\pi} e^{ikr} \bar{G}_k$. Hence the Green function in the presence of a boundary is $\bar{G}_{\text{b}}(r, r) = \bar{G}_{\text{imp}}(r, r) \big|_{U \to \infty} = \bar{G}(0) - \bar{G}(r) G^{(0)}(0)^{-1} \bar{G}(-r)$. The LDOS at r is then $\frac{-1}{\pi} \text{Im} \text{Tr} \bar{G}_{\text{b}}(r, r)$.

Despite the mathematical similarity of the formalism to the (more usual) case of scattering induced by magnetic impurities in s-wave SCs, here we are only considering SC pairing fluctuations as the pair-breaking mechanism. In Fig. 4.3(a), we show the results for $\bar{\rho}_1^w(\omega) / \rho_0$, the averaged LDOS at the end of the nanowire, which is the main quantity determining $G(V)$ at $T = 0$ [cf. Eq. (4.3)]. In each plot, the black to purple curves correspond to $(\Delta_0 \tau_\Delta)^{-1} = 0$ to 1.5 in equal steps of 0.25.

Here, $\tau_\Delta^{-1} \equiv \pi W_\Delta^2 \rho_0$ is the scattering rate induced by SC pairing fluctuations.

For $\Delta_0 \tau_\Delta \leq 1$, the quasiparticle gap vanishes (brown curve). To make contact with our numerical results in Fig. 4.2, in Fig. 4.3(b) we consider a finite $\gamma_N = 0.11\Delta_0$, for the same values of $\Delta_0 \tau_\Delta$ as in Fig. 4.3(a). The quasiparticle decay rate γ_N has the effect of broadening the sharp edge features present in the LDOS when $\gamma_N = 0$. Again, we see that fluctuations in the induced SC pairing together with quasiparticle broadening gives the characteristic v-shaped LDOS in the subgap regime (e.g. cyan and green curves). Our AG theory shows that interface inhomogeneity, encoded in the quantity τ_Δ, can directly explain a soft gap and, therefore, provides a reasonable microscopic origin for the "spin-flip" term in the Usadel equation. A similar gap softening in SC-metal junctions was described using the framework of the Usadel equation with a phenomenological spin-flip term in Ref. [109].

We note that pairing fluctuations in the parent SC may also play a role here since they will also induce pairing fluctuations inside the nanowire [110]. However, given the universality of the soft gap behavior in SMC-SC hybrid structures, which appears independently of the material being used for the parent SC, and under the reasonable assumption of an average low-transparency SC-nanowire interface (i.e. $\gamma_i \ll \Delta_{SC}$), we believe that the soft gap behavior is mainly caused by the interface fluctuations.

4.4 Summary

To summarize, we have studied the effect of different pair-breaking mechanisms likely present in SMC-SC Majorana nanowires, and systematically analyzed their influence on the subgap tunneling conductance in order to explain the experimentally observed soft gap behavior. While we cannot completely rule out some of these mechanisms (i.e. magnetic scattering, thermal and dissipative broadening), quantitative considerations point to the interface fluctuations at the SMC-SC contact leading to inhomogeneous pairing amplitude along the wire as the primary physical mechanism causing the ubiquitous soft gap behavior. Our finding indicates that materials improvement leading to optimized SMC-SC interfaces should considerably ameliorate the proximity gap in the hybrid structures.

Despite the simplicity of our analytical model, the Abrikosov-Gor'kov theory qualitatively explains the results of our numerical simulations and provides useful insight into the physics involved.

Chapter 5

Majoranas in ferromagnetic chains on spin-orbit-coupled superconductors: Weak inter-atomic coupling limit

Apart from the "soft gap" issue which we have studied in details in the previous chapter, a common feature of the experimental realizations [7, 51, 52, 53, 54] of the nanowire proposal is that the conductance can only be measured from the end of the wire. While the ZBCP indicative of the MZM could be picked up by the measurement, it cannot confirm that the MZM is localized at the end of the wire, since the LDOS at the middle of the wire is not measured.

Much attention has recently been directed at an alternative proposal, where a topological band arises from the overlapping Yu-Shiba-Rusinov states [17, 18, 19], or Shiba states for short, in a chain of magnetic impurities with helical spin order on the surface of a superconductor [15, 20, 33, 21, 22, 23, 24, 111, 25, 112, 113]. The helical spin texture plays a critical role combining the effect of the SOC and external field in the nanowire proposal. Topological states are similarly predicted in metallic systems with coexisting superconductivity and helical magnetic order [16, 31, 114]. A significant advantage of the Shiba chain proposal is that it is possible to unam-

biguously image the MZMs using scanning tunneling microscopy (STM), which can be positioned at anywhere along the wire, in contrast to relying on the end transport measurements of nanowire systems. Although critical to ensuring a topological state, the helical order also represents the main experimental difficulty since it is impossible to control externally. The helical order is stable when the magnetic ions are placed on a quasi-1D substrate [21, 22, 23], but for the physically-relevant case of a planar surface, the chain is generically unstable towards a ferromagnetic or antiferromagnetic configuration [26]. A pair-breaking effect in the superconducting state might nevertheless restore the stability of the helical order [112], but disorder effects may still turn out to be a strong detrimental factor [26].

The prospect of unambiguously verifying the existence of MZMs in a Shiba chain motivates the search for a way to realize a topological state in this system without relying upon an intrinsic helical ordering of the impurity spins. There has been a spurt in the activity [28, 115, 116] on topological superconductivity and emergent MZMs in ferromagnetic chains fabricated on the surface of bulk superconductors. In particular, a report of impressive STM experiments [28] has just appeared claiming the generic observation of MZMs at the ends of Fe chains on superconducting Pb. It should be stressed, however, that the connection of this experimental work with the aforementioned Shiba chain proposals is not apparent, since the inter-atomic hopping strength between the Fe atoms could be much stronger than the hybridization energies between the induced Shiba states.

We now attempt to develop a theoretical understanding of such systems, taking the weak and strong inter-atomic hoppings between the Fe atoms in the current

and the following chapter, respectively. In this chapter, where the inter-atomic hoppings are weak (compared with the hybridization energy among the Shiba states), the dynamics of electrons take place mostly within the Shiba states. It is then appropriate to "integrate-out" the Fe atoms, yielding SC with induced Zeeman terms on its surface. A second important feature to note is that the bulk SOC in the SC, together with the local inversion-symmetry breaking on its surface, lead to a Rashba-like SOC term for its surface Hamiltonian. To model this system, we consider a 2D Rashba-coupled SC with a chain of local Zeeman terms. We analytically construct a tight-binding model for the Shiba states valid in the limit of "deep" impurities, when the impurity band lies close to the middle of the superconducting gap. Although the SOC does not affect the Shiba states for an isolated impurity, it dramatically alters the results for the chain. Specifically, spin-flip correlations in the bulk superconductor, induced by the antisymmetric SOC, mix the two branches of the impurity band when the polarization of the impurity spins is transverse to the SOC along the chain. This can be interpreted as a triplet pairing amplitude in a Kitaev-like model, and is thus responsible for the topologically nontrivial state. A magnetic polarization parallel to the SOC, on the other hand, produces no such mixing but instead results in an asymmetric dispersion with trivial topology. We construct a phase diagram, demonstrating that a topological state is possible for infinitesimal SOC strength. The analysis below closely follows that of [24], where a similar tight-binding model for the impurity band was obtained for a chain with spiral magnetic texture embedded in a 3D superconductor.

5.1 Model

A bulk 2D singlet *s*-wave superconductor with Rashba SOC is described by the Hamiltonian $H = \sum_{\mathbf{k}} \Psi_{\mathbf{k}}^{\dagger} \check{H}_{\mathbf{k}} \Psi_{\mathbf{k}}$ where

$$\check{H}_{\mathbf{k}} = \hat{\tau}_z \otimes (\xi_{\mathbf{k}} \hat{\sigma}_0 + \mathbf{l_k} \cdot \hat{\boldsymbol{\sigma}}) + \Delta \hat{\tau}_x \otimes \hat{\sigma}_0 \,. \tag{5.1}$$

Here $\hat{\tau}_{\mu}$ ($\hat{\sigma}_{\mu}$) are the Pauli matrices in Nambu (spin) space, and $\Psi_{\mathbf{k}} = (c_{\mathbf{k},\uparrow}, c_{\mathbf{k},\downarrow}, c_{-\mathbf{k},\downarrow}^{\dagger}, -c_{-\mathbf{k},\uparrow}^{\dagger})^T$ is the spinor of creation and annihilation operators. We have adopted the notation that $\hat{.}$ and $\check{.}$ indicate 2×2 and 4×4 matrices, respectively. The non-interacting dispersion is given by $\xi_{\mathbf{k}} = \hbar^2 \mathbf{k}^2 / 2m - \mu$ where m is the effective mass and μ the chemical potential, the Rashba SOC is parametrized by $\mathbf{l_k} = \lambda(k_y \mathbf{e}_x - k_x \mathbf{e}_y) = \lambda k (\sin\theta \mathbf{e}_x - \cos\theta \mathbf{e}_y)$ where λ is the SOC strength, and Δ is the superconducting gap.

The SOC lifts the spin degeneracy in the normal state, resulting in the dispersions $\xi_{\mathbf{k},\pm} = \xi_{\mathbf{k}} \pm |\mathbf{l_k}|$, where the plus (minus) sign corresponds to the positive (negative) helicity band. As time-reversal symmetry remains intact, however, in the superconducting phase there is only pairing between states in the same helicity band. The bulk Green's function can then be written as $\check{G}_{\mathbf{k}}(\omega) = \frac{1}{2}\{\check{G}_{\mathbf{k}}^{+}(\omega) + \check{G}_{\mathbf{k}}^{-}(\omega)\}$, where

$$\begin{aligned}
\check{G}_{\mathbf{k}}^{\pm}(\omega) &= (\omega \hat{\tau}_0 + \xi_{\pm} \hat{\tau}_z + \Delta \hat{\tau}_x) \otimes (\hat{\sigma}_0 \pm \sin\theta \hat{\sigma}_x \mp \cos\theta \hat{\sigma}_y) \\
&\quad \times \left(\omega^2 - \xi_{\pm}^2 - \Delta^2 \right)^{-1},
\end{aligned} \tag{5.2}$$

is the Green's function in each helicity sector. Note that the SOC produces normal spin-flip and triplet pairing terms in the Green's function. [117] For clarity we suppress the momentum index in the dispersion of the helical bands, i.e. $\xi_{\mathbf{k},\pm} \equiv \xi_\pm$.

5.2 Single impurity

We first consider a single (classical) magnetic impurity with spin $\mathbf{S}$ at the origin, interacting with the electron states with exchange strength $-J$. We include this in our model by adding $H_{\text{imp}} = -J\mathbf{S}\cdot[\Psi^\dagger(\mathbf{0})\hat{\tau}_0\otimes\hat{\boldsymbol{\sigma}}\Psi(\mathbf{0})]$ to the bulk Hamiltonian, where $\Psi(\mathbf{r}) = \int \frac{d^2k}{(2\pi)^2}\Psi_{\mathbf{k}}e^{i\mathbf{k}\cdot\mathbf{r}}$. We aim to solve the Bogoliubov-de Gennes equation $(H + H_{\text{imp}})\psi(\mathbf{r}) = \omega\psi(\mathbf{r})$ for the impurity bound states, i.e. for energy $|\omega| < \Delta$. By straightforward manipulation, [24] the spinor of the bound state at the impurity $\psi(\mathbf{0})$ satisfies the equation

$$\left\{\check{1} + \int \frac{d^2k}{(2\pi)^2}\check{G}_{\mathbf{k}}(\omega)J\mathbf{S}\cdot(\hat{\tau}_0\otimes\hat{\boldsymbol{\sigma}})\right\}\psi(\mathbf{0}) = 0\,. \tag{5.3}$$

To evaluate this equation, we split the Green's function into positive and negative helicity components and then convert the integral over the momentum to an integral over the appropriate dispersion $\xi_\pm$ and the angle θ

$$\int \frac{d^2k}{(2\pi)^2}\check{G}_{\mathbf{k}}^{\pm}(\omega) \approx \frac{\mathcal{N}_\pm}{2\pi}\int_{-D}^{D}d\xi_\pm \int_0^{2\pi}d\theta\check{G}_{\mathbf{k}}^{\pm}(\omega)\,, \tag{5.4}$$

where $\mathcal{N}_\nu = (m/2\pi\hbar^2)[1\mp\widetilde{\lambda}/(1+\widetilde{\lambda}^2)^{1/2}]$ is the density of states of the $\nu = \pm$ helicity band at the Fermi level, $\widetilde{\lambda} = \lambda m/\hbar^2 k_F$ is the ratio of SOC splitting to the

96

Fermi energy and gives a dimensionless measure of the SOC strength, k_F the Fermi wavevector in the absence of SOC, and $D \to \infty$ is a cutoff. The symmetric cutoff in Eq. (5.4) is used for simplicity; Although it implies particle-hole symmetry of the normal dispersion, relaxing this assumption does not qualitatively change our results. The resulting integral is

$$\int \frac{d^2 k}{(2\pi)^2} \check{G}_{\mathbf{k}}^{\pm}(\omega) \approx -\frac{\pi \mathcal{N}_\nu}{\sqrt{\Delta^2 - \omega^2}} \left(\omega \hat{\tau}_0 \otimes \hat{\sigma}_0 + \Delta \hat{\tau}_x \otimes \hat{\sigma}_0 \right) \tag{5.5}$$

Due to the isotropic δ-function structure of the potential, the integrals involving the spin-flip and triplet pairing terms in the Green's function vanish, and Eq. (5.3) therefore has exactly the same form as a magnetic impurity in an s-wave superconductor without SOC, [17, 18, 19, 24] specifically

$$\left\{ \check{1} - \frac{\alpha}{\sqrt{\Delta^2 - \omega^2}} \left[\omega \hat{\tau}_0 + \Delta \hat{\tau}_x \right] \otimes (\mathbf{e_S} \cdot \hat{\boldsymbol{\sigma}}) \right\} \psi(\mathbf{0}) = 0 \,, \tag{5.6}$$

where $\alpha = \frac{\pi}{2}(\mathcal{N}_+ + \mathcal{N}_-) J S$, $S = |\mathbf{S}|$, and $\mathbf{e_S} = \mathbf{S}/S$. The solutions of this equation occur at $\omega = \pm \epsilon_0$, where $\epsilon_0 = \Delta(1 - \alpha^2)/(1 + \alpha^2)$. The form of the corresponding spinors $\psi_{\pm}(\mathbf{0})$ is dictated by the orientation of the impurity spin. Parametrizing $\mathbf{S} = S(\cos\eta \sin\zeta, \sin\eta \sin\zeta, \cos\zeta)$, these spinors can then be written [24] up to unimportant normalization constant as

$$\psi_+(\mathbf{0}) = \begin{pmatrix} \chi_\uparrow \\ \chi_\uparrow \end{pmatrix}, \qquad \psi_-(\mathbf{0}) = \begin{pmatrix} \chi_\downarrow \\ -\chi_\downarrow \end{pmatrix}, \tag{5.7}$$

where

$$\chi_\uparrow = \begin{pmatrix} \cos \zeta/2, & e^{i\eta} \sin \zeta/2 \end{pmatrix}^T, \tag{5.8}$$

$$\chi_\downarrow = \begin{pmatrix} e^{-i\eta} \sin \zeta/2, & -\cos \zeta/2 \end{pmatrix}^T. \tag{5.9}$$

5.3 Ferromagnetic chain

The above analysis can be extended to a chain of ferromagnetically-aligned impurity spins, with the impurity Hamiltonian now written as

$$\mathcal{H}_{\mathrm{imp}} = -J \sum_j \mathbf{S} \cdot [\Psi^\dagger(\mathbf{r}_j)\hat{\tau}_0 \otimes \hat{\boldsymbol{\sigma}} \Psi(\mathbf{r}_j)], \tag{5.10}$$

where $\mathbf{r}_j$ is the position of the jth impurity. We have suppressed the site index of the spins since they all point in the same direction. Without loss of generality, we assume that the chain runs along the x-axis, and so $\mathbf{r}_j = x_j \mathbf{e}_x$. After similar manipulations as in the single impurity problem, the BdG equations for the subgap Shiba states on the chain can be written

$$\left\{ \check{1} - \frac{\alpha}{\sqrt{\Delta^2 - \omega^2}} \left[\omega\hat{\tau}_0 + \Delta\hat{\tau}_x\right] \otimes (\mathbf{e_S} \cdot \hat{\boldsymbol{\sigma}}) \right\} \psi(x_i)$$

$$= -\sum_{j \neq i} \check{J}(x_{ij}) \mathbf{e_S} \cdot (\hat{\tau}_0 \otimes \hat{\boldsymbol{\sigma}}) \psi(x_j) \quad (5.11)$$

where $x_{ij} = x_i - x_j$ and the matrix $\check{J}(x_{ij})$ is defined

98

$$
\begin{aligned}
\check{J}(x_{ij}) &= JS \int \frac{d^2k}{(2\pi)^2} \check{G}_{\mathbf{k}}(\omega)e^{ik_x x_{ij}} \\
&= \frac{JS}{2} \left\{ [I_1^-(x_{ij}) + I_1^+(x_{ij})]\hat{\tau}_z \otimes \hat{\sigma}_0 + \omega[I_3^-(x_{ij}) + I_3^+(x_{ij})]\hat{\tau}_0 \otimes \hat{\sigma}_0 \right. \\
&\quad + \Delta[I_3^-(x_{ij}) + I_3^+(x_{ij})]\hat{\tau}_x \otimes \hat{\sigma}_0 + [I_2^-(x_{ij}) - I_2^+(x_{ij})]\hat{\tau}_z \otimes \hat{\sigma}_y \\
&\quad \left. + \omega[I_4^-(x_{ij}) - I_4^+(x_{ij})]\hat{\tau}_0 \otimes \hat{\sigma}_y + \Delta[I_4^-(x_{ij}) - I_4^+(x_{ij})]\hat{\tau}_x \otimes \hat{\sigma}_y \right\} \quad (5.12)
\end{aligned}
$$

We have expressed this in terms of the integrals

$$
I_1^\nu(x) = \frac{\mathcal{N}_\nu}{2\pi} \int_{-D}^{D} d\xi \int_0^{2\pi} d\theta \frac{\xi e^{ik_\nu(\xi)x\cos\theta}}{\omega^2 - \xi^2 - \Delta^2} , \tag{5.13a}
$$

$$
I_2^\nu(x) = \frac{\mathcal{N}_\nu}{2\pi} \int_{-D}^{D} d\xi \int_0^{2\pi} d\theta \frac{\xi e^{i\theta} e^{ik_\nu(\xi)x\cos\theta}}{\omega^2 - \xi^2 - \Delta^2} , \tag{5.13b}
$$

$$
I_3^\nu(x) = \frac{\mathcal{N}_\nu}{2\pi} \int_{-D}^{D} d\xi \int_0^{2\pi} d\theta \frac{e^{ik_\nu(\xi)x\cos\theta}}{\omega^2 - \xi^2 - \Delta^2} , \tag{5.13c}
$$

$$
I_4^\nu(x) = \frac{\mathcal{N}_\nu}{2\pi} \int_{-D}^{D} d\xi \int_0^{2\pi} d\theta \frac{e^{i\theta} e^{ik_\nu(\xi)x\cos\theta}}{\omega^2 - \xi^2 - \Delta^2} , \tag{5.13d}
$$

where $k_\nu(\xi) = k_{F,\nu} + \xi/\hbar v_{F,\nu}$, while $k_{F,\nu} = k_F[(1+\widetilde{\lambda}^2)^{1/2} - \nu\widetilde{\lambda}]$ and $v_{F,\nu} = (\hbar k_F/m)(1 + \widetilde{\lambda}^2)^{1/2}$ are the Fermi vector and velocity for the ν helicity band, respectively. In the limit of $D \to \infty$, these integrals evaluate to

$$
I_1^\nu(x) = \pi\mathcal{N}_\nu \text{Im} \left\{ J_0((k_{F,\nu} + i\xi_\nu^{-1})|x|) + iH_0((k_{F,\nu} + i\xi_\nu^{-1})|x|) \right\} , \tag{5.14}
$$

$$
I_2^\nu(x) = -i\pi\mathcal{N}_\nu \,\text{sgn}(x)\text{Re} \left\{ iJ_1((k_{F,\nu} + i\xi_\nu^{-1})|x|) + H_{-1}((k_{F,\nu} + i\xi_\nu^{-1})|x|) \right\} , \tag{5.15}
$$

$$
I_3^\nu(x) = -\frac{\pi\mathcal{N}_\nu}{\sqrt{\Delta^2 - \omega^2}} \text{Re} \left\{ J_0((k_{F,\nu} + i\xi_\nu^{-1})|x|) + iH_0((k_{F,\nu} + i\xi_\nu^{-1})|x|) \right\} , \tag{5.16}
$$

$$
I_4^\nu(x) = -\text{sgn}(x)\frac{i\pi\mathcal{N}_\nu}{\sqrt{\Delta^2 - \omega^2}} \text{Im} \left\{ iJ_1((k_{F,\nu} + i\xi_\nu^{-1})|x|) + H_{-1}((k_{F,\nu} + i\xi_\nu^{-1})|x|) \right\} \tag{5.17}
$$

where $J_n(z)$ and $H_n(z)$ are Bessel and Struve functions of order n, respectively, and $\xi_\nu = \hbar v_{F,\nu}/\sqrt{\Delta^2 - \omega^2}$. Note that $I_1^\nu(x)$ and $I_3^\nu(x)$ are even functions of x, whereas $I_2^\nu(x)$ and $I_4^\nu(x)$ are odd. In the limit of $k_{F,\nu}|x| \gg 1$, we can use asymptotic forms valid for large values of the argument close to the positive real axis, giving

$$I_1^\nu(x) \approx \pi \mathcal{N}_\nu \sqrt{\frac{2}{\pi k_{F,\nu}|x|}} \sin\left(k_{F,\nu}|x| - \tfrac{\pi}{4}\right) e^{-|x|/\xi_\nu} + \frac{2\mathcal{N}_\nu}{k_{F,\nu}|x|}, \tag{5.18}$$

$$I_2^\nu(x) \approx i\pi\mathcal{N}_\nu \operatorname{sgn}(x) \sqrt{\frac{2}{\pi k_{F,\nu}|x|}} \sin\left(k_{F,\nu}|x| - \tfrac{3\pi}{4}\right) e^{-|x|/\xi_\nu} + \operatorname{sgn}(x)\frac{2i\mathcal{N}_\nu}{(k_{F,\nu}x)^2} \tag{5.19}$$

$$I_3^\nu(x) \approx -\frac{\pi\mathcal{N}_\nu}{\sqrt{\Delta^2 - \omega^2}} \sqrt{\frac{2}{\pi k_{F,\nu}|x|}} \cos\left(k_{F,\nu}|x| - \tfrac{\pi}{4}\right) e^{-|x|/\xi_\nu}, \tag{5.20}$$

$$I_4^\nu(x) \approx -\operatorname{sgn}(x)\frac{i\pi\mathcal{N}_\nu}{\sqrt{\Delta^2 - \omega^2}} \sqrt{\frac{2}{\pi k_{F,\nu}|x|}} \cos\left(k_{F,\nu}|x| - \tfrac{3\pi}{4}\right) e^{-|x|/\xi_\nu}. \tag{5.21}$$

The non-oscillating component is valid up to $\mathcal{O}((k_{F,\nu}|x|)^{-3})$.

In contrast to the single-impurity system considered above, the presence of SOC makes a significant difference to the BdG equations for the multi-impurity problem: while the first line of Eq. (5.12) is identical to the result found in [24], the second line is only present for nonzero SOC. This line contains explicitly magnetic terms $\propto \hat{\sigma}_y$, reflecting the orientation of the SOC vector $\mathbf{l_k}||\mathbf{e}_y$ for $\mathbf{k}$ pointing along the magnetic chain.

5.4 Tight-binding model

We do not attempt a general solution of Eq. (5.11), but instead consider the analytically-tractable limit of dilute "deep" impurities, as discussed in [24]. Specifi-

cally, we assume that $\alpha \approx 1$, so that the energy ϵ_0 of the isolated Shiba state lies close to the center of the gap, and that the spacing a between impurities is sufficiently large that the impurity band formed from the hybridized Shiba states lies entirely within the superconducting gap. Linearizing the BdG equations Eq. (5.11) in the energy ω and the coupling between impurity sites, we obtain after straightforward manipulation

$$\Delta \left[\mathbf{e_S} \cdot (\hat{\tau}_0 \otimes \hat{\boldsymbol{\sigma}}) - \alpha \hat{\tau}_x \otimes \hat{\sigma}_0 \right] \psi(x_i) + \Delta \sum_{j \neq i} \mathbf{e_S} \cdot (\hat{\tau}_0 \otimes \hat{\boldsymbol{\sigma}}) \lim_{\omega \to 0} \check{J}(x_{ij}) \mathbf{e_S} \cdot (\hat{\tau}_0 \otimes \hat{\boldsymbol{\sigma}}) \psi(x_j)$$

$$= \omega \psi(x_i) \quad (5.22)$$

This equation is now projected into the Shiba states [Eq. (5.7)] at each site, to obtain a BdG-type equation for the impurity band

$$\widetilde{H}(i,j)\phi_j = \omega \phi_i \quad (5.23)$$

where $\phi_i = (u_{i,+}, u_{i,-})^T$ is the vector of the wavefunctions for the $+$ and $-$ Shiba states at site i and

$$\widetilde{H}(i,j) = \begin{pmatrix} A_{ij} + B_{ij} & C_{ij} \\ C_{ji}^* & -A_{ij} + B_{ij} \end{pmatrix} \quad (5.24)$$

where

$$A_{ij} = \epsilon_0 \delta_{ij} + \frac{1}{2} JS\Delta^2 \lim_{\omega \to 0} \left[I_3^+(x_{ij}) + I_3^-(x_{ij}) \right] , \tag{5.25}$$

$$B_{ij} = \frac{1}{2} JS\Delta^2 \sin\eta \sin\zeta \lim_{\omega \to 0} \left[I_4^-(x_{ij}) - I_4^+(x_{ij}) \right] , \tag{5.26}$$

$$C_{ij} = -\frac{i}{2} JS\Delta \left(\cos^2 \tfrac{\zeta}{2} + \sin^2 \tfrac{\zeta}{2} e^{-2i\eta} \right)$$

$$\times \lim_{\omega \to 0} \left[I_2^-(x_{ij}) - I_2^+(x_{ij}) \right] . \tag{5.27}$$

Note that the integrals in these expressions are to be regarded as vanishing for $i = j$.

The effective tight-binding Hamiltonian Eq. (5.24) is the central result of this chapter. Due to the antisymmetry of the integrals $I_2^\nu(x)$ in the off-diagonal terms, it can be interpreted as describing superconducting spinless fermions, recalling the Kitaev model, [4] albeit with long-range hopping and pairing terms. The properties of this system depend crucially on the SOC in the bulk superconductor and the polarization of the impurity spins. Specifically, the pairing term C_{ij} is only present for non-vanishing SOC, and when the polarization of the ferromagnetic chain has a component perpendicular to the y-axis. Examining Eq. (5.12), we observe that the pairing term originates from the spin-flip correlations in the host superconductor induced by the SOC. A polarization component along the y-axis contributes an antisymmetric hopping B_{ij} in the presence of SOC. This echoes the asymmetric dispersion of a SOC electron gas in the direction of an applied magnetic field, and its appearance here is due to the triplet pairing correlations in the bulk Green's function Eq. (5.2).

A similar tight-binding model was derived in [24], but there the odd-parity

pairing term arose from the spiral magnetic texture of the impurity chain. This mechanism for generating a pairing term is still valid in the presence of the SOC considered here. Examining the interplay of spiral spin texture and SOC is an interesting topic which we leave to later work.

5.5 Topological properties

To conclude we examine the topology of the impurity band. For an infinite chain with uniform spacing a of the impurities, we define the Fourier transform of the Hamiltonian Eq. (5.24)

$$\widetilde{H}(k) = \begin{pmatrix} A(k) + B(k) & C(k) \\ C^*(k) & -A(k) + B(k) \end{pmatrix} \tag{5.28}$$

where $A(k) = \sum_j A_{0j} e^{ikja}$, etc. Using the asymptotic forms for the integrals, the analytical expressions for these quantities in the limit $k_{F,\nu}a \gg 1$ are obtained as

$$
\begin{aligned}
I_2^\nu(k) &= \mathcal{N}_\nu \sqrt{\frac{\pi}{2k_{F,\nu}a}} \left\{ e^{-3\pi i/4} \mathrm{Li}_{\frac{1}{2}}\left(e^{i(k_{F,\nu}a+ka)-a/\xi_\nu}\right) - e^{3\pi i/4} \mathrm{Li}_{\frac{1}{2}}\left(e^{i(-k_{F,\nu}a+ka)-a/\xi_\nu}\right) \right. \\
&\quad \left. - e^{-3\pi i/4} \mathrm{Li}_{\frac{1}{2}}\left(e^{i(k_{F,\nu}a-ka)-a/\xi_\nu}\right) - e^{3\pi i/4} \mathrm{Li}_{\frac{1}{2}}\left(e^{i(-k_{F,\nu}a-ka)-a/\xi_\nu}\right) \right\} \\
&\quad + \frac{2i\mathcal{N}_\nu}{(k_{F,\nu}a)^2}\left\{ \mathrm{Li}_2\left(e^{ika}\right) - \mathrm{Li}_2\left(e^{-ika}\right) \right\} , \tag{5.29}
\end{aligned}
$$

$$
\begin{aligned}
I_3^\nu(k) &= -\frac{\mathcal{N}_\nu}{\sqrt{\Delta^2 - \omega^2}} \sqrt{\frac{\pi}{2k_{F,\nu}a}} \left\{ e^{-\pi i/4} \mathrm{Li}_{\frac{1}{2}}\left(e^{i(k_{F,\nu}a+ka)-a/\xi_\nu}\right) \right. \\
&\quad + e^{\pi i/4} \mathrm{Li}_{\frac{1}{2}}\left(e^{i(-k_{F,\nu}a+ka)-a/\xi_\nu}\right) + e^{-\pi i/4} \mathrm{Li}_{\frac{1}{2}}\left(e^{i(k_{F,\nu}a-ka)-a/\xi_\nu}\right) \\
&\quad \left. + e^{\pi i/4} \mathrm{Li}_{\frac{1}{2}}\left(e^{i(-k_{F,\nu}a-ka)-a/\xi_\nu}\right) \right\} , \tag{5.30}
\end{aligned}
$$

$$
\begin{aligned}
I_4^\nu(k) &= -\frac{i\mathcal{N}_\nu}{\sqrt{\Delta^2 - \omega^2}} \sqrt{\frac{\pi}{2k_{F,\nu}a}} \left\{ e^{-3\pi i/4} \mathrm{Li}_{\frac{1}{2}}\left(e^{i(k_{F,\nu}a+ka)-a/\xi_\nu}\right) \right. \\
&\quad + e^{3\pi i/4} \mathrm{Li}_{\frac{1}{2}}\left(e^{i(-k_{F,\nu}a+ka)-a/\xi_\nu}\right) - e^{-3\pi i/4} \mathrm{Li}_{\frac{1}{2}}\left(e^{i(k_{F,\nu}a-ka)-a/\xi_\nu}\right) \\
&\quad \left. - e^{3\pi i/4} \mathrm{Li}_{\frac{1}{2}}\left(e^{i(-k_{F,\nu}a-ka)-a/\xi_\nu}\right) \right\} , \tag{5.31}
\end{aligned}
$$

where $\mathrm{Li}_s(z)$ is the polylogarithm of order s. The Hamiltonian Eq. (5.28) is in Altland-Zirnbauer symmetry class D, and for a fully-gapped system it is therefore characterized by the $\mathbb{Z}_2$ topological invariant [4]

$$
Q = \mathrm{sgn}\{A(0)A(\pi/a)\} . \tag{5.32}
$$

The system is topologically nontrivial for $Q = -1$; conversely, $Q = 1$ indicates a trivial state.

To demonstrate that our model supports a topologically nontrivial state, in Fig. (5.1)
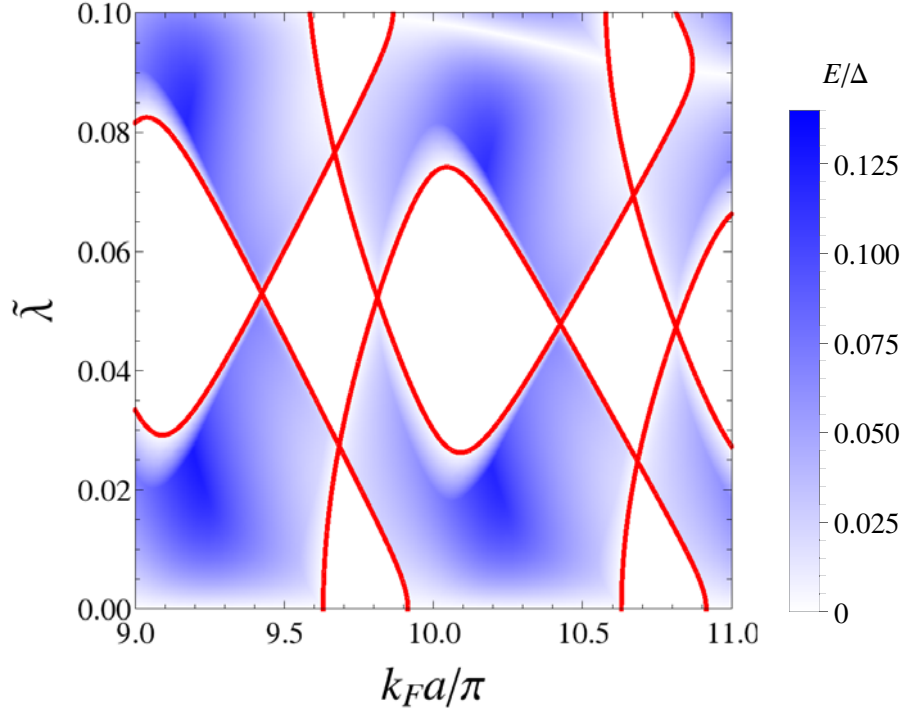
Figure 5.1: Topological phase diagram for the effective model as a function of $k_F a$ and $\widetilde{\lambda}$. The topological regions are shaded according to the magnitude of the gap, while the non-topological regions are left blank. Red lines indicate the boundary between topological and non-topological phases. We have chosen $\epsilon_0 = 0$ for the isolated impurity level and $\xi_0 = 5a$ for the superconducting coherence length at $\widetilde{\lambda} = 0$, which ensures that the impurity band remains within the superconducting gap. The impurity spins point in the x-z plane. The large values of $k_F a$ allow us to utilize the asymptotic expressions for the entries in Eq. (5.28).

we present a phase diagram as a function of the dimensionless SOC $\widetilde{\lambda}$ and the parameter $k_F a$, which gives a measure of the Fermi surface volume or alternatively the spacing of the chain. We consider only a polarization in the x-z plane. In the topologically non-trivial regions, we plot the minimum gap magnitude, demonstrating the existence of a fully gapped state; the non-topological regions are left white. The most important aspect of this phase diagram is that a topological state is revealed to be possible even for infinitesimal SOC. Remarkably, the excitation spectrum can display a substantial gap even for very small SOC strength $\widetilde{\lambda} \ll 1$. We emphasize that our analysis is only valid for ϵ_0 sufficiently close to zero, and so other methods are required to comprehensively survey the phase diagram.

5.6   Summary

In this chapter we have studied the appearance of a topological impurity band when a ferromagnetic chain of classical spins are embedded in a 2D singlet s-wave superconductor with Rashba SOC. To this end, we have derived an effective tight-binding model for the overlapping Shiba states of the impurities. When the spins are polarized perpendicular to the SOC along the chain, an odd-parity pairing term is induced in the effective Hamiltonian, thus realizing a Kitaev-like model with generically non-trivial topology. This is an alternative route to a topological Shiba chain which do not rely upon helical spin texture. [15, 20, 33, 21, 22, 23, 24, 111, 25, 112, 113] This is a significant result, as the stability of the helical spin texture is debated. [112, 26] In contrast, the SOC mechanism examined here is intrinsic to

the superconductor surface. This implies that topological phases are possible for a much wider variety of impurity spin configurations than hitherto realized, which grants the Shiba chain proposal additional robustness and lends strong theoretical support to experimental efforts to detect MZMs in such a setting. As revealed by our calculated quantum phase diagram Fig. (5.1), however, the topological phase in the ferromagnetic Shiba chain system is not generic. Some fine-tuning of the system is therefore required in order to observe topological MZMs through the measurement, for example, of ZBCPs in tunneling spectroscopy experiments.

Although we have confined ourselves to the analytically-tractable limit of a dilute chain of deep impurities, we expect that our results are of more general validity since they rely only upon the low-energy form of the Green's function. We have also neglected complicating factors such as particle-hole asymmetry in the normal state dispersion, the suppression of the superconducting gap close to the impurity spins, and the 3D nature of the superconducting host. These issues must certainly be accounted for when modeling a realistic system, but can only be addressed using large-scale computer simulations. Nevertheless, none of these effects should invalidate the mechanism giving rise to the topological state of our basic model which arises simply from the interplay between ferromagnetism, superconductivity, and SOC.

Chapter 6

Majoranas in ferromagnetic chains on spin-orbit-coupled superconductors: Strong inter-atomic coupling limit

In this chapter we continue on our theoretical exploration of the system considered in the previous chapter, with ferromagnetic chains of atoms (Fe) on SOC SC (Pb). We now focus on the other limit where the hoppings between the Fe atoms are much stronger than the hybridization energies between the Shiba states. In this case, the dynamics of the itinerant electrons happen at the ferromagnetic chains, and there it is more appropriate to "integrate-out" the SC, focusing on the chains instead of the SC (as was done in the previous chapter). Another difference is that now we will not use an effective Rashba-coupled surface Hamiltonian like the one we had used in the previous chapter. Instead, we shall develop a phenomenological model in which the the *bulk* SOC in the SC, together with the local inversion-symmetry breaking due to the surface of the SC, leads to additional terms in the effective Hamiltonian of the chain of atoms.

Before developing our model, we first review the classification of topological superconductors [118, 119, 120, 121]. In a 1D class-D topological superconductor,

e.g., the nanowire proposal [5, 6], if a pair of MZMs are spatially superimposed on each other, they would mix and split to finite energies, becoming low-energy fermionic subgap states [122]. In this class of topological superconducting systems, therefore, the number of MZMs (n) can be either zero or one. This results in a greatly reduced parameter space in which to look for experimental signatures of MZMs. In the nanowire heterostructure, for example, ZBCPs are expected only when the number of bands crossing the Fermi energy is odd [123, 124], a condition difficult to control experimentally. Similarly, previous proposals for realizing a MZM in ferromagnet-superconductor heterostructures [125, 126] have the stringent requirement that only one of the spin-split bands in the ferromagnet has a Fermi surface. In the system we explore in this chapter, as we shall show below, the system is in class BDI due to the presence of a chiral symmetry. The number of MZMs in this class can be any positive integer, which results in a greatly enhanced parameter space in which MZMs are realized. Although only when n is odd does the Majorana multiplet follow non-Abelian braiding statistics, a robust ZBCP in STM experiments should occur generically for any value of n. Of course, for the purpose of establishing topologically protected degenerate states that may be used to establish non-Abelian braiding [3], it is necessary for the Majorana to be non-degenerate i.e. $n = 1$, and therefore the generic ZBCP signature here cannot necessarily be identified with a non-Abelian Majorana "particle". Our conceptual new finding that robust MZMs may reside generically (i.e. without fine-tuning) in superconductor-ferromagnet heterostructures, protected by a chiral symmetry, is the important new result.
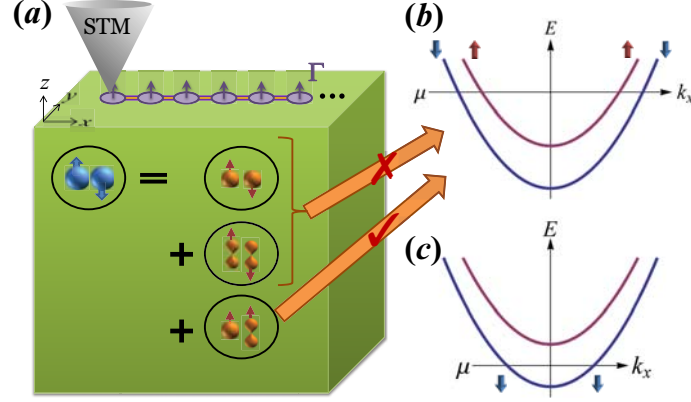
Figure 6.1: (a) Schematic diagram of our device. A ferromagnetic chain is placed on the surface of an s-wave superconductor, in which strong SOC and mixing of orbitals of opposite parity produce a pairing state with intra-orbital spin-singlet Cooper pairs and inter-orbital spin-triplet pairs. Tunneling of these pairs into the chain generates effective spin-singlet and spin-triplet pairing potentials, respectively, as shown in (b). For a ferromagnetic chain with spin-splitting that exceeds the spin-singlet pairing potential, only the induced triplet pairing potential can gap the spectrum. In this case the system is in a topologically nontrivial state characterized by two unhybridized MZMs at each end, which can be imaged by STM. When the ferromagnetic chain is in the half-metal regime as shown in panel (c), however, only a non-Abelian single MZM is realized at each end. If the spin-splitting of the chain states is much smaller than their bandwidth, however, the situation (b) dominates the parameter space.

6.1   The System

A ferromagnetic chain (e.g. Fe), which is a single atom in width, is placed on the surface of a bulk s-wave superconductor, as shown schematically in Fig. 6.1. We emphasize that, in contrast to arrays of magnetic atoms on the surface of a superconductor, the ferromagnetic chain is expected to have a bandwidth that is orders of magnitude larger than the superconducting pairing potential. We ignore the SOC within the ferromagnetic chain, but instead account for the existence of strong inversion-symmetric SOC in the bulk of the host superconductor. By inte-

grating out the bulk superconductor we show that the effective Hamiltonian of the ferromagnetic chain [Eq. (6.31) below] is in the chiral BDI class with an integer invariant, allowing an integer number n of MZMs localized at the chain ends. If the ferromagnetic chain has only one pair of spin-split sub-bands, n can be equal to zero, one, or two, but for *any* non-zero n (a condition that is realized in most of the parameter space (Fig. 6.2)) STM measurements at the chain ends should reveal a pronounced ZBCP. The ZBCP is in fact generic in our model, occurring in a wide region of the experimentally-accessible parameter space as shown in Fig. 6.2 and 6.3. No such peak is expected from the regions of the chain away from the ends where the MZMs are localized. In practice the effective chiral symmetry in the ferromagnetic chain should only be approximate, resulting in a finite energy width of the ZBCPs for $n > 1$.

6.2   Effective Hamiltonian of the chain.

6.2.1   Pseudospin Basis

The superconductor used in our device must satisfy two key conditions: (i) there is strong SOC [26], although inversion symmetry is not necessarily broken in the bulk, and (ii) orbitals of different parity both make a significant contribution to the states near the Fermi surface. The requirement that the orbitals have opposite parity can be relaxed, but this condition makes the following argument more transparent. The first condition implies that spin is not a good quantum number in the superconductor, but the presence of time-reversal ($\mathcal{T}$) and inversion

($\mathcal{I}$) symmetry means that the doubly-degenerate eigenstates at each momentum $\mathbf{k}$ can be labeled by a pseudospin index $\varsigma = \pm$, such that $\mathcal{T}|\mathbf{k}, \varsigma\rangle = \varsigma| - \mathbf{k}, -\varsigma\rangle$ and $\mathcal{I}|\mathbf{k}, \varsigma\rangle = | - \mathbf{k}, \varsigma\rangle$. A conventional s-wave superconducting gap then corresponds to a pseudospin-singlet pairing state. To satisfy the second condition, we assume that the states near the Fermi surface are composed from two orbitals, say s and $p \equiv p_z$, which are symmetric and antisymmetric under inversion, respectively. The general form of the pseudospin state is then

$$|\boldsymbol{k}, \varsigma\rangle = \sum_{\sigma=\uparrow,\downarrow} \left[B_{s,\varsigma\sigma}\left(\boldsymbol{k}\right) |s, \boldsymbol{k}, \sigma\rangle + B_{p,\varsigma\sigma}\left(\boldsymbol{k}\right) |p, \boldsymbol{k}, \sigma\rangle \right], \qquad (6.1)$$

where $B_{s,\varsigma\sigma}\left(\boldsymbol{k}\right)$ and $B_{p,\varsigma\sigma}\left(\boldsymbol{k}\right)$ are the coefficients of the s- and p-wave orbitals, respectively. Regarding the coefficients in Eq. (6.1) as 2×2 matrices in $\varsigma - \sigma$ space, one can derive a number of conditions. First, the normalization of the states in Eq. (6.1) requires that

$$\hat{s}_0 = B_s^*\left(\boldsymbol{k}\right) B_s^T\left(\boldsymbol{k}\right) + B_p^*\left(\boldsymbol{k}\right) B_p^T\left(\boldsymbol{k}\right). \qquad (6.2)$$

The pseudospin index $\varsigma = \pm$ transforms as a spin under time-reversal ($\mathcal{T}$) and inversion ($\mathcal{I}$) symmetries. From

$$\mathcal{T}|\mathbf{k}, \varsigma\rangle = \sigma| - \mathbf{k}, -\varsigma\rangle, \qquad \mathcal{I}|\mathbf{k}, \varsigma\rangle = | - \mathbf{k}, \varsigma\rangle, \qquad (6.3)$$

$$\mathcal{T}|s, \mathbf{k}, \sigma\rangle = \sigma|s, -\mathbf{k}, -\sigma\rangle, \qquad \mathcal{I}|s, \mathbf{k}, \sigma\rangle = |s, -\mathbf{k}, \sigma\rangle, \qquad (6.4)$$

$$\mathcal{T}|p, \mathbf{k}, \sigma\rangle = \sigma|p, -\mathbf{k}, -\sigma\rangle, \qquad \mathcal{I}|p, \mathbf{k}, \sigma\rangle = -|p, -\mathbf{k}, \sigma\rangle, \qquad (6.5)$$

we deduce the relations obeyed by the coefficients

$$B_s(\boldsymbol{k}) = B_s(-\boldsymbol{k}) = \hat{s}_y B_s^*(-\boldsymbol{k})\,\hat{s}_y\,, \qquad (6.6a)$$

$$B_p(\boldsymbol{k}) = -B_p(-\boldsymbol{k}) = \hat{s}_y B_p^*(-\boldsymbol{k})\,\hat{s}_y\,. \qquad (6.6b)$$

In these equations $\hat{s}_\mu$ are Pauli matrices in the $\varsigma - \sigma$ space. We additionally require that the pseudospin index behaves like a spin under mirror reflection in the planes perpendicular to the three Cartesian axes:

$$\mathcal{M}_x\,|\boldsymbol{k},\varsigma\rangle = |\mathcal{M}_x\boldsymbol{k},-\varsigma\rangle\,, \qquad \mathcal{M}_y\,|\boldsymbol{k},\varsigma\rangle = i\varsigma\,|\mathcal{M}_y\boldsymbol{k},-\varsigma\rangle\,, \qquad (6.7)$$

$$\mathcal{M}_z\,|\boldsymbol{k},\varsigma\rangle = \varsigma\,|\mathcal{M}_z\boldsymbol{k},\varsigma\rangle\,,$$

$$\mathcal{M}_x\,|s,\boldsymbol{k},\sigma\rangle = |s,\mathcal{M}_x\boldsymbol{k},-\sigma\rangle\,, \quad \mathcal{M}_y\,|s,\boldsymbol{k},\sigma\rangle = i\sigma\,|s,\mathcal{M}_y\boldsymbol{k},-\sigma\rangle\,, \qquad (6.8)$$

$$\mathcal{M}_z\,|s,\boldsymbol{k},\sigma\rangle = \sigma\,|s,\mathcal{M}_z\boldsymbol{k},\sigma\rangle\,,$$

$$\mathcal{M}_x\,|p,\boldsymbol{k},\sigma\rangle = |p,\mathcal{M}_x\boldsymbol{k},-\sigma\rangle\,, \quad \mathcal{M}_y\,|p,\boldsymbol{k},\sigma\rangle = i\sigma\,|p,\mathcal{M}_y\boldsymbol{k},-\sigma\rangle\,, \qquad (6.9)$$

$$\mathcal{M}_z\,|s,\boldsymbol{k},\sigma\rangle = -\sigma\,|p,\mathcal{M}_z\boldsymbol{k},\sigma\rangle\,,$$

from which we can derive

$$B_s(\boldsymbol{k}) = \hat{s}_\mu B_s(\mathcal{M}_\mu\boldsymbol{k})\,\hat{s}_\mu\,, \quad \mu = x,y,z\,, \qquad (6.10a)$$

$$B_p(\boldsymbol{k}) = \begin{cases} \hat{s}_\mu B_p(\mathcal{M}_\mu\boldsymbol{k})\,\hat{s}_\mu & \mu = x,y \\[2mm] -\hat{s}_\mu B_p(\mathcal{M}_\mu\boldsymbol{k})\,\hat{s}_\mu & \mu = z \end{cases} \qquad (6.10b)$$

where $\mathcal{M}_\mu$ are reflection operators for the plane perpendicular to the μ-axis.

6.2.2 Green's function in orbital-spin basis

Expressed in the basis $\Psi_{\text{pseudo}}(\mathbf{k}) = (c_{\mathbf{k},+}, c_{\mathbf{k},-}, c_{\mathbf{k},-}^\dagger, -c_{\mathbf{k},+}^\dagger)^T$, where $c_{\mathbf{k},\varsigma}$ is the annihilation operator for the state with momentum $\mathbf{k}$ and pseudospin ς, the pseudospin Green's function of the bulk superconductor is the 4×4 matrix

$$G_{\text{pseudo}}(\mathbf{k}, \omega) = \frac{\omega \hat{\tau}_0 + \xi_{\mathbf{k}} \hat{\tau}_z + \Delta_0 \hat{\tau}_x}{\omega^2 - \xi_{\mathbf{k}}^2 - \Delta_0^2} \tag{6.11}$$

where $\xi_{\mathbf{k}}$ is the normal state dispersion, Δ_0 is the superconducting gap, and $\hat{\tau}_\mu$ are the Pauli matrices in Nambu space. From Eq. (6.1) we have the relation

$$\Psi_{\text{pseudo}}(\mathbf{k}) = \begin{pmatrix} \check{B}_{\mathbf{k}}^* & 0 \\ 0 & \check{B}_{\mathbf{k}}^* \end{pmatrix} \Psi_{\text{orb}}(\mathbf{k}) \tag{6.12}$$

where

$$\Psi_{\text{orb}}(\mathbf{k}) = \left(s_{\mathbf{k},\uparrow}, s_{\mathbf{k},\downarrow}, p_{\mathbf{k},\uparrow}, p_{\mathbf{k},\downarrow}, s_{-\mathbf{k},\downarrow}^\dagger, -s_{-\mathbf{k},\uparrow}^\dagger, p_{-\mathbf{k},\downarrow}^\dagger, -p_{-\mathbf{k},\uparrow}^\dagger \right)^T \tag{6.13}$$

is the spinor of creation and annihilation operators in the orbital-spin basis, where $s_{\mathbf{k},\sigma}$ $(p_{\mathbf{k},\sigma})$ destroys an electron with momentum $\mathbf{k}$ and spin σ in the s (p) orbital, and

$$\check{B}_{\mathbf{k}} = \begin{pmatrix} \hat{B}^s(\mathbf{k}) & \hat{B}^p(\mathbf{k}) \end{pmatrix} \tag{6.14}$$

is a 2×4 matrix, with $\hat{B}^s(\mathbf{k})$ and $\hat{B}^p(\mathbf{k})$ as defined above. Using equation (6.12), we express the Green's function in the orbital basis as

$$G_{\mathrm{orb}}(\mathbf{k}, \omega) = \begin{pmatrix} \check{B}_{\mathbf{k}}^T & 0 \\ 0 & \check{B}_{\mathbf{k}}^T \end{pmatrix} G_{\mathrm{pseudo}}(\mathbf{k}, \omega) \begin{pmatrix} \check{B}_{\mathbf{k}}^* & 0 \\ 0 & \check{B}_{\mathbf{k}}^* \end{pmatrix}, \qquad (6.15)$$

where $G_{\mathrm{orb}}(\mathbf{k}, \omega)$ is an 8×8 matrix. It is important to note that since this Green's function is obtained from the pseudospin Green's function $G_{\mathrm{pseudo}}(\mathbf{k}, \omega)$, it is only valid close to the Fermi energy. The full orbital-spin Green's function contains terms from the additional band composed from the s and p orbitals, but since this band is assumed to lie far away from the Fermi surface we ignore them.

6.2.3 Proximity-Induced Self-energy

The chain is placed on the (001) surface of the superconductor. The tunneling between the chain and the superconductor is assumed to be local and independent of spin, and is therefore most transparently formulated in terms of tunneling between the chain atoms and the adjacent orbitals of the superconductor. We assume the form

$$H_{\mathrm{tun}} = \sum_{\mathbf{r} \in \mathrm{chain}} \sum_{\sigma} \left\{ f_{\mathbf{r},\sigma}^\dagger [t_s s_{\mathbf{r},\sigma} + t_p p_{\mathbf{r},\sigma}] + \mathrm{H.c.} \right\} \qquad (6.16)$$

where t_s and t_p are the tunneling matrix elements for the two orbitals, assumed real, and $f_{\mathbf{r},\sigma}$, $s_{\mathbf{r},\sigma}$ and $p_{\mathbf{r},\sigma}$ are the annihilation operators for the site $\mathbf{r}$ in the chain and in the superconductor's s and p orbitals, respectively. The tunneling Hamiltonian implicitly accounts for the surface inversion-symmetry breaking: if the odd-parity

orbital is odd with respect to mirror reflection in the surface plane, then tunneling from the chain sites into both the even- and odd-parity orbitals of the underlying superconductor can have a local component (see Fig. (6.1)). Since we are interested in the physics of the chain, our strategy is now to "trace out" the superconductor from the description of the problem.

The proximity effect in the chain due to the superconductor is fully accounted-for by the self-energy

$$\Sigma(x, x'; \omega) = \mathbf{T}G_{\text{orb}}(x, x'; \omega)\mathbf{T}^{\dagger}, \tag{6.17}$$

where the 4×8 matrix $\mathbf{T}$ describes the tunneling between the orbital-spin states of the superconductor and the ferromagnetic chain

$$\mathbf{T} = \begin{pmatrix} t_s\hat{1} & t_p\hat{1} & 0 & 0 \\ 0 & 0 & -t_s\hat{1} & -t_p\hat{1} \end{pmatrix}. \tag{6.18}$$

For simplicity, we approximate the Green's function of the superconductor at the surface by the bulk Green's function equation (6.15). This is a reasonable approximation for the conventional superconductors considered here. We hence obtain

$$\begin{aligned} \Sigma(x, x'; \omega) &= \int \frac{d^3k}{(2\pi)^3} \mathbf{T}G_{\text{orb}}(\mathbf{k}, \omega)\mathbf{T}^{\dagger}e^{ik_x(x-x')} \\ &= \int \frac{d^3k}{(2\pi)^3} \Sigma(\mathbf{k}, \omega)e^{ik_x(x-x')} \end{aligned} \tag{6.19}$$

After straightforward manipulation, we find

$$\Sigma\left(\omega; \boldsymbol{r}, \boldsymbol{r}'\right) = \int \frac{d^3k}{(2\pi)^3} e^{i\boldsymbol{k}\cdot(\boldsymbol{r}-\boldsymbol{r}')} T\left(\boldsymbol{k}\right) G_{SC}\left(\omega; \boldsymbol{k}\right) T\left(\boldsymbol{k}\right)^{\dagger}$$

$$= \left(1 - Z\right)\omega + Zt\tau_z + Z\boldsymbol{\lambda}\cdot\boldsymbol{\sigma}\tau_z$$

$$+ Z\Delta\tau_x + Z\boldsymbol{\Delta}^{(t)}\cdot\boldsymbol{\sigma}\tau_x, \tag{6.20}$$

where Z, t, $\boldsymbol{\lambda}$, Δ and $\boldsymbol{\Delta}^{(t)}$ are functions of ω and $\boldsymbol{r} - \boldsymbol{r}'$:

$$Z = 1 - \int \frac{d^3k}{(2\pi)^3} \frac{1}{\omega^2 - \xi_{\boldsymbol{k}}^2 - \Delta_{SC}^2} M_1, \tag{6.21}$$

$$Zt_{\boldsymbol{r},\boldsymbol{r}'} = \int \frac{d^3k}{(2\pi)^3} e^{i\boldsymbol{k}\cdot(\boldsymbol{r}-\boldsymbol{r}')} \frac{\xi_{\boldsymbol{k}}}{\omega^2 - \xi_{\boldsymbol{k}}^2 - \Delta_{SC}^2} M_1, \tag{6.22}$$

$$Z\boldsymbol{\lambda}_{\boldsymbol{r},\boldsymbol{r}'}\cdot\boldsymbol{\sigma} = \int \frac{d^3k}{(2\pi)^3} e^{i\boldsymbol{k}\cdot(\boldsymbol{r}-\boldsymbol{r}')} \frac{\xi_{\boldsymbol{k}}}{\omega^2 - \xi_{\boldsymbol{k}}^2 - \Delta_{SC}^2} M_2, \tag{6.23}$$

$$Z\Delta_{\boldsymbol{r},\boldsymbol{r}'} = -\int \frac{d^3k}{(2\pi)^3} e^{i\boldsymbol{k}\cdot(\boldsymbol{r}-\boldsymbol{r}')} \frac{\Delta_{SC}}{\omega^2 - \xi_{\boldsymbol{k}}^2 - \Delta_{SC}^2} M_1, \tag{6.24}$$

$$Z\boldsymbol{\Delta}_{\boldsymbol{r},\boldsymbol{r}'}\cdot\boldsymbol{\sigma} = -\int \frac{d^3k}{(2\pi)^3} e^{i\boldsymbol{k}\cdot(\boldsymbol{r}-\boldsymbol{r}')} \frac{\Delta_{SC}}{\omega^2 - \xi_{\boldsymbol{k}}^2 - \Delta_{SC}^2} M_2, \tag{6.25}$$

where $M_1 \equiv t_s^2 B_s^T B_s^* + t_p^2 B_p^T B_p^*$ and $M_2 \equiv t_s^2 B_s^T B_p^* + t_p^2 B_p^T B_s^*$. The terms in M_1 describe tunneling processes involving only one of the orbitals in the superconductor, while the terms in M_2 arise from tunneling processes involving both orbitals. It is seen from Eq. (6.20) that terms involving M_1 modifies the dispersion and introduces singlet pairing correlations, while terms involving M_2 introduce spin-triplet pairing correlations into the ferromagnetic chain. We therefore generally expect that there will be triplet Cooper pairs with spin parallel to the magnetization, and so a gap appears in the spin-split states of the ferromagnetic chain, see Fig. 6.1(b). By contrast,

the spin-singlet pairing due to tunneling of intra-orbital Cooper pairs is unable to overcome the large exchange splitting. The proximity effect also renormalizes the bare dispersion and produces a SOC, but these effects are small and will be ignored.

6.2.4 Effective Hamiltonian

We now consider the self-energy of the ferromagnetic nanowire in more detail. Assuming that the nanowire lies along the x-axis, in the absence of the superconductor it can be modeled by the tight-binding Hamiltonian

$$
\begin{aligned}
H &= t_{\text{int}} \sum_{n\sigma} \left(a_{n\sigma}^{\dagger} a_{n+1,\sigma} + \text{h.c.} \right) \\
&\quad - \mu \sum_{n\sigma} a_{n\sigma}^{\dagger} a_{n\sigma} + B \sum_{n\sigma} \sigma a_{n\sigma}^{\dagger} a_{n\sigma} \,.
\end{aligned}
\tag{6.26}
$$

where t_{int} is the hopping intrinsic to the nanowire (*not* mediated by the superconductor), μ is the chemical potential, and B is the (spontaneous) ferromagnetic exchange field (written out as an intrinsic magnetic field, rather than as an exchange splitting, in order to maintain the explicit analogy to the SMC nanowire platforms where B is an extrinsic magnetic field).

Including the self-energy due to the proximate superconductor, the eigenenergies of the nanowire are given by the poles of the Green function

$$
G_{\text{wire}}(\omega) = \frac{1}{\omega - H_{\text{BdG}} - \Sigma(\omega)} = \frac{Z^{-1}}{\omega - H_{\text{eff}}(\omega)}
\tag{6.27}
$$

where H_{BdG} is the BdG Hamiltonian of the bare nanowire Eq. (6.26), and in the

second equality we have rearranged terms such that the effect of frequency renormalization is captured by Z, and H_{eff} contains no terms proportional to $\omega\hat{\tau}_0$. Explicitly,

$$
\begin{aligned}
H_{\text{eff}}\left(\omega; x_m, x_n\right) \;=\;\; & Z^{-1}t_{\text{int}}\left(\delta_{m,n+1} + \delta_{m,n-1}\right)\hat{\tau}_z \\
& -Z^{-1}\mu\delta_{m,n}\hat{\tau}_z + Z^{-1}B\delta_{m,n}\hat{\sigma}_z \\
& +t_{m-n}\hat{\tau}_z + \boldsymbol{\lambda}_{m-n}\cdot\boldsymbol{\sigma}\hat{\tau}_z \\
& +\Delta_{m-n}\hat{\tau}_x + \boldsymbol{\Delta}^{(t)}_{m-n}\cdot\boldsymbol{\sigma}\hat{\tau}_x.
\end{aligned}
\tag{6.28}
$$

The subscript $m-n$ indicates that the quantities in Eq. (6.20) are evaluated at nanowire sites with relative coordinates $\boldsymbol{r} - \boldsymbol{r}' = \left(x_m - x_n\right)\boldsymbol{e}_x$.

In general, the physics of the nanowire is extracted from the Green function $G_{\text{wire}}\left(\omega\right)$ including the frequency-dependent self-energy. Since we are interested only in the zero-energy Majorana mode and energy scales $\omega \ll \Delta_0$, however, we may take $H_{\text{eff}}\left(\omega = 0\right)$ as our effective BdG Hamiltonian with no loss of generality.

To make further analytical progress we need to assume specific forms of B_s and B_p. We take

$$
B_s\left(\boldsymbol{k}\right) \;=\;\; \cos\theta\,\hat{s}_0,
\tag{6.29a}
$$

$$
B_p\left(\boldsymbol{k}\right) \;=\;\; \sin\theta\,\boldsymbol{e_k}\cdot\left(\hat{s}_y, -\hat{s}_x, i\hat{s}_0\right),
\tag{6.29b}
$$

where $\boldsymbol{e_k} = \boldsymbol{k}/|\boldsymbol{k}|$. This choice is consistent with the symmetries of the pseudospin states Eq. (6.1), and leads to an analytically tractable result which captures the essential physics we wish to explore. Other choices lead to qualitatively similar

results.

Using Eq. (6.29) we calculate the full frequency-dependent forms of Z, t, $\boldsymbol{\lambda}$, Δ and $\boldsymbol{\Delta}^{(t)}$. At zero energy they take the relatively compact forms

$$Z = 1 + \frac{\Gamma}{\Delta_{SC}}, \tag{6.30a}$$

$$t_{n>0} = \frac{\Gamma}{Z} \frac{\cos n\tilde{a}}{n\tilde{a}} e^{-n/\tilde{\xi}}, \tag{6.30b}$$

$$\boldsymbol{\lambda}_{n>0} \cdot \boldsymbol{\sigma} = -i\sigma_y g \sin 2\theta \frac{\Gamma}{Z} \frac{\cos n\tilde{a} + n\tilde{a} \sin n\tilde{a}}{n^2 \tilde{a}^2} e^{-n/\tilde{\xi}} \tag{6.30c}$$

$$\Delta_n = \frac{\Gamma}{Z} \frac{\sin n\tilde{a}}{n\tilde{a}} e^{-n/\tilde{\xi}} \tag{6.30d}$$

$$\boldsymbol{\Delta}^{(t)}_{n>0} \cdot \boldsymbol{\sigma} = i\sigma_y g \sin 2\theta \frac{\Gamma}{Z} \frac{\sin n\tilde{a} - n\tilde{a} \cos n\tilde{a}}{n^2 \tilde{a}^2} e^{-n/\tilde{\xi}}, \tag{6.30e}$$

where we have introduced dimensionless variables $\Gamma = \pi\nu \left(t_s^2 \cos^2\theta + t_p^2 \sin^2\theta \right)$, $g = \pi\nu t_s t_p$, $\tilde{a} = k_F a_{\text{lat}}$, and $\tilde{\xi} = \xi/a_{\text{lat}}$, in which ν and ξ are respectively the Fermi-level density of states and the coherence length of the superconductor, and a_{lat} is the lattice constant of the tight-binding model of the nanowire [Eq. (6.26)].

Although these expressions are quite complicated, we can nevertheless make some generic observations. Firstly, we note that the renormalization of the dispersion and the singlet pairing potential arise only from the intra-orbital tunneling processes (i.e. only terms $\propto t_{s/p}^2$ appear). On the other hand, the inter-orbital processes are responsible for the SOC and the triplet gap. The opposite parity of the s and p orbitals is crucial in obtaining these terms; tunneling into orbitals of the same parity could only give even-parity contributions to the self-energy. Furthermore, we observe that the induced SOC vector is always parallel to the triplet $\mathbf{d}$ vector,

i.e. $\boldsymbol{\lambda}_n \parallel \boldsymbol{\Delta}_n^{(t)}$. We expect that the pairing terms are generally much larger than the normal-state corrections, however, due to the factor of $\xi_{\mathbf{k}}$ in the integrals of the latter. We henceforth ignore t_n and $\boldsymbol{\lambda}_n$ in constructing the effective Hamiltonian.

Neglecting corrections beyond nearest-neighbor pairing, we obtain the effective Hamiltonian of the chain

$$
\begin{aligned}
H_{\text{chain}}^{\text{eff}}(k_x) &= (-2t\cos k_x - \mu)\,\hat{\tau}_z + \boldsymbol{\Gamma}\cdot\hat{\boldsymbol{\sigma}} \\
&\quad + \left(\Delta + \tilde{\Delta}\cos k_x\right)\hat{\tau}_x + \tilde{\Delta}^{(t)}\sin k_x\hat{\sigma}_y\hat{\tau}_x\,,
\end{aligned}
\tag{6.31}
$$

where $\hat{\sigma}_\mu$ and $\hat{\tau}_\mu$ are the Pauli matrices in spin and Nambu space, respectively. The first line of the Hamiltonian describes the bare ferromagnetic chain with direct inter-atom hopping t, chemical potential μ, and a Zeeman splitting $\boldsymbol{\Gamma}\cdot\hat{\boldsymbol{\sigma}}$ due to ferromagnetism which is comparable to the Fermi energy in the wire. The last line gives the induced superconducting gaps with both singlet (Δ and $\tilde{\Delta}$) and triplet ($\tilde{\Delta}^{(t)}$) pairing potentials. The latter corresponds to a state where the triplet pairs have vanishing spin component along the y-axis which can gap the spin-split bands as long as $\boldsymbol{\Gamma}$ has a component in the x-z plane.

The key experimentally-relevant quantity is the LDOS, which can be directly measured using STM. The LDOS at position x is defined as

$$
\nu(x,\omega) = \frac{-1}{2\pi}\text{Im Tr}\left[\omega + i\delta - H_{\text{chain}}^{\text{eff}}(x,x)\right]^{-1}(1 + \hat{\tau}_z)\,.
\tag{6.32}
$$

Throughout this chapter we fix $t = 10\Delta$ and $\tilde{\Delta} = \tilde{\Delta}^{(t)} = 0.2\Delta$, and study how
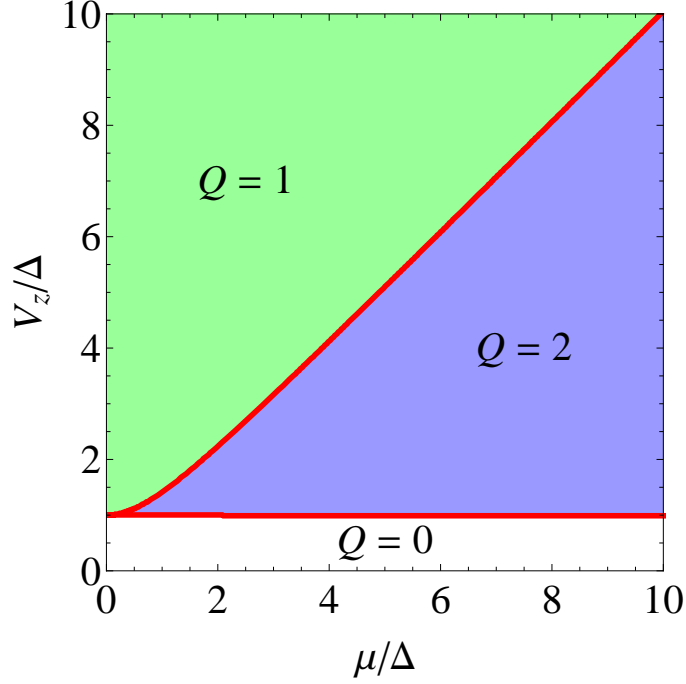
Figure 6.2: Topological phase diagram of the chain. The BDI topological index Q is defined in equation (6.34) calculated for $H_{\text{chain}}^{\text{eff}}$ as a function of the Zeeman splitting Γ_z and the chemical potential. The Green region (roughly $\Gamma_z > \tilde{\mu}/2$) has $Q = 1$ while the blue region (roughly $\Gamma_z < \tilde{\mu}/2$) has $Q = 2$, indicating the existence of one and two MZMs at each end of the chain, respectively.

the topology of the system varies as a function of μ and $\boldsymbol{\Gamma}$. We emphasize that our results are generic and qualitatively independent of the precise choice of these parameters.

6.3   Topological properties of the chain.

For obtaining the topological classification of $H_{\text{chain}}^{\text{eff}}$ we note that it satisfies the particle-hole symmetry $\left\{H_{\text{chain}}^{\text{eff}}, \hat{\bar{\Xi}}\right\} = 0$, where $\hat{\bar{\Xi}} = \sigma_y \tau_y K$ and K is the complex-conjugate operator. If we further assume that the y component of $\boldsymbol{\Gamma}$ is zero, $H_{\text{chain}}^{\text{eff}}$ is real and hence it has the chiral symmetry $\left\{H_{\text{chain}}^{\text{eff}}, \hat{\mathcal{C}}\right\} = 0$ where $\hat{\mathcal{C}} = \sigma_y \tau_y$. In this

case, $H_{\text{chain}}^{\text{eff}}$ belongs to the BDI topological class and is endowed with a topological index Q equal to the number of zero-energy MZM modes $(n = Q)$ localized at its ends. To compute Q, we first rotate $H_{\text{chain}}^{\text{eff}}$ to the basis in which $\hat{\mathcal{C}}$ is diagonal, by $\hat{U} = e^{-i\frac{\pi}{4}\tau_x \sigma_y}$, such that

$$\tilde{H}_{\text{chain}}^{\text{eff}} = \hat{U} H_{\text{chain}}^{\text{eff}} \hat{U}^\dagger = \begin{pmatrix} 0 & A_{k_x} \\ A_{-k_x}^T & 0 \end{pmatrix}, \tag{6.33}$$

whence Q is computed by

$$Q = \frac{1}{\pi} \int_0^\pi dk_x \frac{d\arg\left(\det A_{k_x}\right)}{dk_x}. \tag{6.34}$$

In Fig. 6.2 we plot Q against $\tilde{\mu}$ and Γ_z, where $\mathbf{\Gamma}$ is taken as $\mathbf{\Gamma} = \Gamma_z \mathbf{e}_z$ such that the chiral symmetry is respected (the chiral symmetry is respected as long as $\mathbf{\Gamma}$ is in the $(x\text{-}z)$ plane), and $\tilde{\mu} = \mu + 2t$ is defined from the bottom of the non-spin-split bands. Note that for approximately $\Delta < \Gamma_z < \tilde{\mu}/2$, we have $Q = 2$ while for $\Delta, \tilde{\mu}/2 < \Gamma_z$ we have $Q = 1$, indicating, in both cases, the existence of MZMs at the chain ends. This can be understood in the following way: in the large Zeeman spin-splitting ("half-metal") limit, the effects of the singlet pairing terms Δ and $\tilde{\Delta}$ on the Bogoliubov-de Gennes spectrum are suppressed due to a large Fermi momenta mismatch between the two spin species. Then, with the triplet pairing $\tilde{\Delta}^{(t)}$, the system becomes effectively an equal-spin-pairing triplet superconductor with non-zero $\Delta_{\uparrow\uparrow}$ and $\Delta_{\downarrow\downarrow}$, which can be viewed as two copies of the Kitaev p-wave chain spatially superimposed on each other [127]. If $\tilde{\mu}$ is such that both spin channels are

123
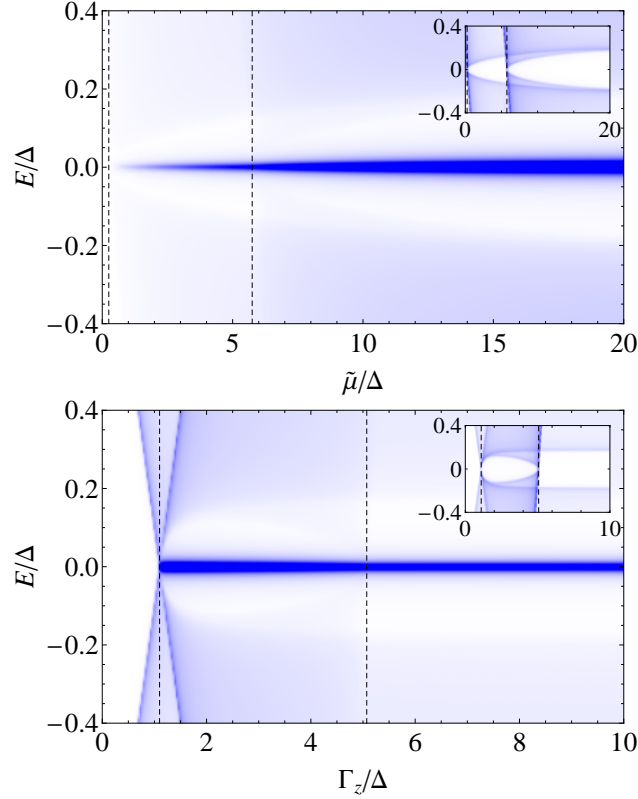
Figure 6.3: (a) The LDOS at the ends of the semi-infinite ferromagnetic chain as a function of the chemical potential $\tilde{\mu}$ from the bottom of the bands, for $\Gamma_z = 3\Delta$. The LDOS has a strong ZBP that for roughly $\tilde{\mu} < 2\Gamma_z$ indicates a single MZM from the chain ends, while for $\tilde{\mu} > 2\Gamma_z$ the ZBP implies a pair of MZMs localized at each ends protected by chiral symmetry. (b) the LDOS at the chain ends as a function of the Zeeman splitting for $\tilde{\mu} = 10\Delta$. For roughly $\Gamma_z < \tilde{\mu}/2$ ($\Gamma_z > \tilde{\mu}/2$) the ZBP in LDOS signifies two (one) MZMs at each end that can be accessed in STM experiments. The insets shows the LDOS at the middle of the chain, which has a spectral gap in the topological regions. We indicate the transitions between the different topological sectors by the vertical dashed lines, and use arbitrary units for the LDOS in these plots.

occupied, we get $Q = 2$ (two MZMs at each end of the chain), while if $\tilde{\mu}$ is such that only one channel is occupied, we get $Q = 1$ (an MZM at each end). Since most itinerant ferromagnets are not half metals, and the induced singlet gap Δ is likely much smaller than $\tilde{\mu}$, we expect that the $Q = 2$ phase is of greatest practical relevance.

In Fig. 6.3(a,b) we plot the LDOS at the ends of the semi-infinite ferromagnetic chain as a function of $\tilde{\mu}$ and Γ_z, respectively. It can be seen that the LDOS generically has a pronounced ZBP that can be accessed in STM measurements near the chain ends. For the Zeeman splitting $\tilde{\mu} > 2\Gamma_z$ the ZBP is due to a pair of MZMs localized at the same ends and protected from splitting by the topological chiral symmetry. For $\tilde{\mu} < 2\Gamma_z$ the ZBP implies a single MZM that should follow non-Abelian braiding statistics. No such ZBP is observed in LDOS calculated for the middle of the chain, although the superconducting gap in the chain closes at the topological transitions at which the integer Q (and thus the number of MZMs at the chain ends) changes, see the inset of Fig. 6.3(a,b).

6.4 Discussion and Conclusion

While the above results demonstrate that it is not necessary to fine-tune the chemical potential or Zeeman spin-splitting to generate a ZBP in LDOS (and consequently a ZBCP in STM measurements) at the ends of the ferromagnetic chain, a component of $\boldsymbol{\Gamma}$ perpendicular to the x-z plane breaks the chiral symmetry. To assess the effects of misalignment of the Zeeman splitting (which can, for example,

be generated by a suitably applied external magnetic field), we plot in Fig. 6.4 the LDOS against θ, where now we choose $\mathbf{\Gamma} = 3\Delta \left(\sin \theta \mathbf{e}_y + \cos \theta \mathbf{e}_z \right)$. The zero-energy LDOS peak at the end of the chain splits into two peaks at finite energy by a non-zero θ only in the phase $Q = 2$. As θ is tuned up, the magnitude of the splitting first increases, then decreases, and finally vanishes with a concomitant disappearance of the localized peak. This can be understood from the observation that the y-component of $\mathbf{\Gamma}$ has an additional effect of suppressing the spectral gap of the system, and since the splitting is bounded by the size of the spectral gap, the size of the splitting can never reach a large value. Therefore, the splitting of the zero-energy LDOS peak due to a misalignment of the Zeeman term is always small. No such splitting should be observable in the phase with $Q = 1$. This is because in these regions of the phase diagram, each end of the chain hosts a single MZM, and thus the ZBCP persists. Although the system is no longer in class BDI, it reduces to a class-D topological superconductor with zero or one MZM at each end.

In conclusion, we consider a ferromagnetic chain deposited on the surface of a bulk s-wave superconductor with strong SOC. We establish the generic existence of a ZBP in the LDOS at the ends of the chain in this system. The ZBP in the LDOS should be accessible in STM experiments which should reveal a pronounced ZBCP from the chain ends but not from the regions away from the ends. We show that the ZBCP is due to the existence of one (odd) or two (even) MZMs localized at the same end protected by a topological chiral symmetry. In this picture an STM experiment on the ends of a ferromagnetic chain deposited on the surface of a bulk superconductor (with strong SOC) will almost always show a pronounced ZBCP,

126
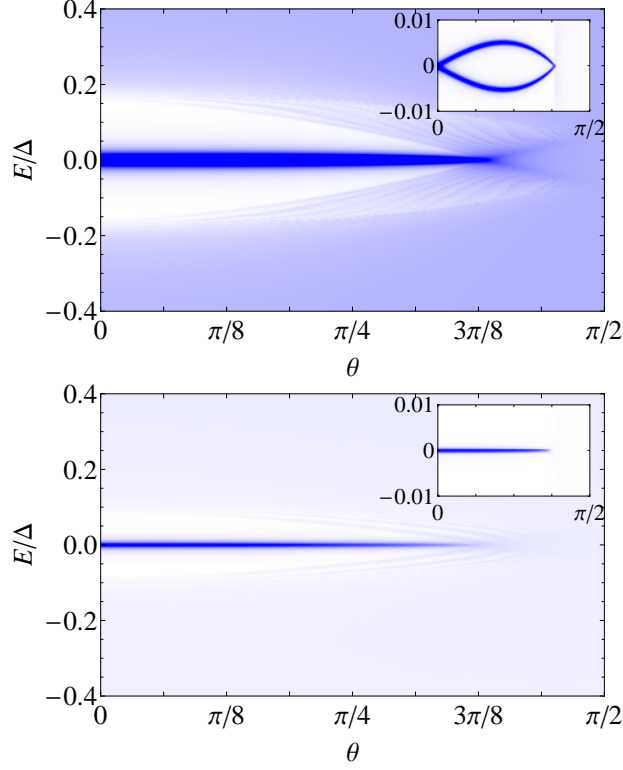
Figure 6.4: (a) LDOS at one end of the semi-infinite ferromagnetic chain as a function of θ in the phase $Q = 2$, where $\tilde{\mu} = 15\Delta$ and $\boldsymbol{\Gamma} = 3\Delta \left(\sin\theta \mathbf{e}_y + \cos\theta \mathbf{e}_z \right)$. Since the y-component of $\boldsymbol{\Gamma}$ breaks chiral symmetry, the pair of MZMs at each end mix and split for finite θ, but the splitting is small and visible only on a small energy scale shown in the inset. (b) The LDOS at the chain end plotted against θ for $Q = 1$ where $\tilde{\mu} = 2.5\Delta$ and $\boldsymbol{\Gamma}$ is the same as above. Since there is now a single MZM at each end the ZBP does not split. Although the system is no longer in class BDI, it is still a class-D topological superconductor with zero or one MZM at each end. We use arbitrary units for the LDOS in these plots.

indicating the existence of one or two MZMs at each end depending on the relative magnitudes of the ferromagnetic moment and the chemical potential.

Chapter 7

Substrate-induced Majorana renormalization in topological nanowires

In this chapter, we attempt to explain a peculiar feature observed in experimental setups [28] which might be described by our model in the previous chapter. More specifically, the observed localization length (or equivalently the SC coherence length ξ) of the purported MZMs in such system was extremely short (of the order of nm). On the other hand, it is often assumed to be of the order of the superconducting coherence length, $\xi \sim v_F/\Delta$, where v_F and Δ are respectively the Fermi velocity and the induced SC gap in the chain. Since the estimated SC gap in the Fe adatom chains on Pb substrates studied in Ref. [28] is very small ($\sim 0.1\,\mathrm{meV}$), this was expected to lead to a long coherence length of $\xi > 100\,\mathrm{nm}$ (assuming no substrate-induced renormalization) which would be much larger than the typical length of the adatom chains ($5 - 50\,\mathrm{nm}$) used in Ref. [28].

Ref. [128] studied this problem for a helical spin texture on the SC, and suggested that the substrate might greatly suppress the MZM localization length. This immediately brings up the question of whether such a phenomenon is also operational in the nanowire proposals, where we note that their experiments [7, 52, 129, 51, 53, 54] have so far been simply interpreted on the basis of the standard $\xi \sim v_F/\Delta$

formula with no substrate-induced coherence length suppression. One possible rec-

onciliation for this is simply by assuming that the ferromagnetic chain is strongly

tunnel-coupled to the substrate superconductor, while the SMC nanowire is not.

but we want to avoid such an *ad hoc* assumption.

In this chapter, to set a context, we start by discussing the localization length

of MZMs in the Kitaev chain [4] in various parameter regimes. Following this,

we consider the proximity effect of the bulk superconductor, which we show below

induces a self-energy on the wire. The local part of it has the form of

$$\Sigma\left(\omega; \boldsymbol{r}, \boldsymbol{r}\right) \sim -\frac{\Gamma\omega}{\Delta_{SC}}\hat{\tau}_0 + \Gamma\hat{\tau}_x, \tag{7.1}$$

where Γ is the parameter determining the strength of the proximity coupling. As

we argue in Sec. 7.4, the proximity parameter $\Gamma \sim (k_F R)^{-3} E_F$, where $k_F \sim 10\,\mathrm{nm}^{-1}$

and $E_F \sim 1\,\mathrm{eV}$ are respectively the Fermi wave-number and the Fermi energy in the

superconductor, and R is the radius of the nanowire. In mesoscopic SMC nanowire

geometries $R \sim 20\mathrm{nm}$ leading to $\Gamma \sim 0.1\mathrm{meV} \sim \Delta_{SC}$, and this fits into the simple

picture for the proximity effect where the frequency dependence can be ignored.

Atomistic ferromagnetic wires are qualitatively different since $R \sim 0.5\mathrm{nm}$ for these

wires and the estimated $\Gamma \sim 1\mathrm{eV}$. This clearly puts the analysis in the regime

$\Gamma \gg \Delta_{SC}$, which is the strongly renormalized limit [72]. Establishing this key

difference between the MZMs in SMC and atomistic nanowires is a main goal of this

chapter.

7.1 Majorana decay length in the Kitaev Chain

Let us first consider the prototypical and simplest model of a topological superconductor supporting MZMs, the Kitaev chain. This is a 1D tight-binding model of spinless fermions with p-wave pairing, described by the Hamiltonian

$$
\begin{aligned}
H_w = &-t \sum_j \left(a_j^\dagger a_{j+1} + \text{h.c.} \right) - \mu \sum_j a_j^\dagger a_j \\
&+ \Delta_p \sum_j \left(a_j a_{j+1} + \text{h.c.} \right),
\end{aligned}
\tag{7.2}
$$

where t is the hopping between lattice sites, μ the chemical potential, and Δ_p is the pairing potential. As shown by Kitaev [4], this model supports unpaired MZMs at its boundaries for $|\mu| < 2\,|t|$, with a MZM localization length that is given by

$$
\xi = \max_{\lambda = \pm 1} \left(\left| \log \left| \frac{\lambda \sqrt{\mu^2 - 4t^2 + 4\Delta_p^2} - \mu}{2\left(t + |\Delta_p|\right)} \right| \right| \right)^{-1}.
\tag{7.3}
$$

We plot the localization length in Fig. 7.1 as a function of the hopping amplitude for different values of μ. Note that ξ is defined only for $|t| > |\mu|\,/2$, where the system is in the topologically non-trivial regime with a MZM at each end. At $|t| = |\mu|\,/2$ the localization length diverges, indicating a topological phase transition into the topologically trivial regime at $|t| < |\mu|/2$.

There are two special limits of interest. At the special point $\mu = 0$ and $|t| = |\Delta_p|$, the localization length vanishes and the MZM is localized precisely at the end site of the chain [4]. We emphasize that in this fine-tuned case the localization of the
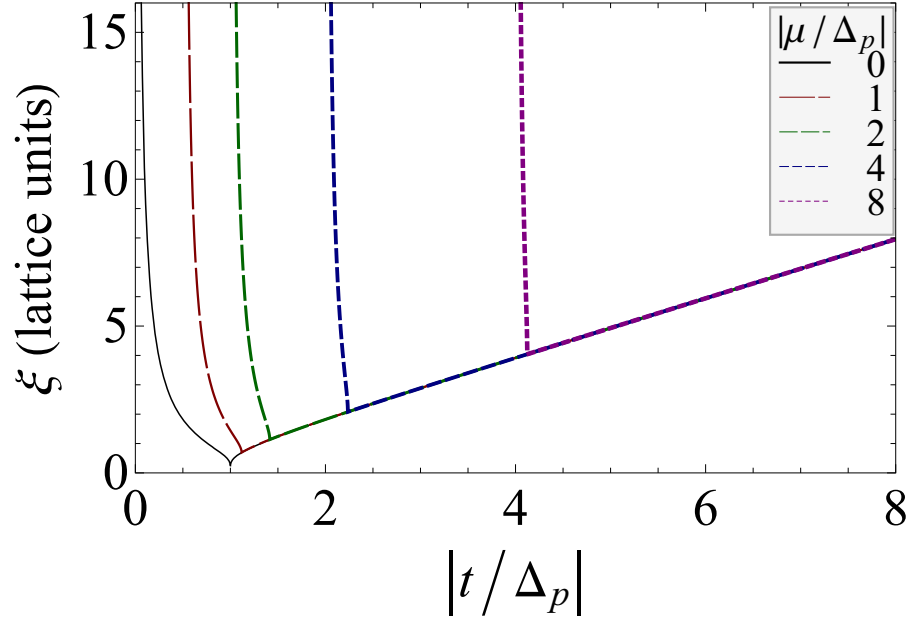
Figure 7.1: MZM localization length (ξ) given by Eq. (7.3) as a function of dimensionless hopping strength ($|t/\Delta_p|$) for various values of the chemical potential ($|\mu/\Delta_p|$). For $|t| < |\mu|/2$ the system is in the non-topological phase without MZMs, and ξ is undefined in this regime. ξ diverges at $|t| = |\mu|/2$, indicating the topological phase transition. For $|t| \gg |\mu|$, ξ is well-approximated by $|t/\Delta_p|$, which is the standard coherence length formula for superconductors.

MZM is completely independent of the size of the energy gap, providing a concrete example of a situation where a small gap could in principle also be associated with a small localization length. The other situation of interest is the physically realistic limit $|t| \gg |\Delta_p|$, where the bandwidth far exceeds the superconducting gap [38]. Here the localization length ξ, expressed to lowest order in Δ_p, reproduces the familiar form of a superconducting coherence length as discussed in the Introduction,

$$\xi = \left| \frac{t}{\Delta_p} \right| = \frac{v_F}{2E_{\mathrm{gap}}}, \tag{7.4}$$

where $E_{\mathrm{gap}} = |\Delta_p|(1 - \mu^2/4t^2)^{1/2}$ and $v_F = 2|t|(1 - \mu^2/4t^2)^{1/2}$ are the spectral gap and Fermi velocity, respectively. Since $|t| \gg |\Delta_p|$, the localization length $\xi \gg 1$ and the Majorana decay length is parametrically larger than the lattice constant (taken to be the unit of length here). On the other hand, it is clear that if for some reasons one can realize a Kitaev chain with $|t| \sim |\Delta_p|$, as has been proposed for a quantum dot array [29], then the MZM decay length is of order a few lattice sites only, qualitatively similar to the fine-tuned case.

7.2 Effective Kitaev models

In the previous chapter we have derived the effective Hamiltonian for the atomistic wire, given by

$$
\begin{aligned}
H_{\text{eff}}\left(\omega; x_m, x_n\right) &= Z^{-1} t_{\text{int}}\left(\delta_{m,n+1} + \delta_{m,n-1}\right)\hat{\tau}_z \\
&\quad - Z^{-1}\mu\delta_{m,n}\hat{\tau}_z + Z^{-1}B\delta_{m,n}\hat{\sigma}_z \\
&\quad + t_{m-n}\hat{\tau}_z + \boldsymbol{\lambda}_{m-n}\cdot\boldsymbol{\sigma}\hat{\tau}_z \\
&\quad + \Delta_{m-n}\hat{\tau}_x + \boldsymbol{\Delta}^{(t)}_{m-n}\cdot\boldsymbol{\sigma}\hat{\tau}_x.
\end{aligned} \tag{7.5}
$$

where

$$
Z = 1 + \frac{\Gamma}{\Delta_{SC}}, \tag{7.6a}
$$

$$
t_{n>0} = \frac{\Gamma}{Z}\frac{\cos n\tilde{a}}{n\tilde{a}}e^{-n/\tilde{\xi}}, \tag{7.6b}
$$

$$
\boldsymbol{\lambda}_{n>0}\cdot\boldsymbol{\sigma} = -i\sigma_y g\sin 2\theta\frac{\Gamma}{Z}\frac{\cos n\tilde{a} + n\tilde{a}\sin n\tilde{a}}{n^2\tilde{a}^2}e^{-n/\tilde{\xi}} \tag{7.6c}
$$

$$
\Delta_n = \frac{\Gamma}{Z}\frac{\sin n\tilde{a}}{n\tilde{a}}e^{-n/\tilde{\xi}} \tag{7.6d}
$$

$$
\boldsymbol{\Delta}^{(t)}_{n>0}\cdot\boldsymbol{\sigma} = i\sigma_y g\sin 2\theta\frac{\Gamma}{Z}\frac{\sin n\tilde{a} - n\tilde{a}\cos n\tilde{a}}{n^2\tilde{a}^2}e^{-n/\tilde{\xi}}, \tag{7.6e}
$$

where

$$
\Gamma = \pi\nu\left(t_s^2\cos^2\theta + t_p^2\sin^2\theta\right), \tag{7.7}
$$

$g = \pi\nu t_s t_p$, $\tilde{a} = k_F a_{\text{lat}}$, and $\tilde{\xi} = \xi/a_{\text{lat}}$, in which ν and ξ are respectively the Fermi-level density of states and the coherence length of the superconductor.

In the limit of large exchange field $\left(|B| \gg |\boldsymbol{\lambda}_n|,\ \text{and}\ |B| \gg |\boldsymbol{\Delta}_n|\right)$, the effects

of the SOC and *s*-wave pairing terms are suppressed. The model (7.5) thus reduces to two copies of the Kitaev model, albeit with long-range hopping. To make connections with Sec. 7.1, we first ignore the long-ranged part of the self-energy which is beyond nearest neighbors, yielding (second quantized) effective Hamiltonians for spin-up (+) and spin-down (−) species

$$
\begin{aligned}
H_0^{(\pm)} &= -\left(Z^{-1}t_{\text{int}} + t_1\right)\sum_j \left(a_j^\dagger a_{j+1} + \text{h.c.}\right) \\
&\quad -Z^{-1}\left(\mu \mp B\right)\sum_j a_j^\dagger a_j \\
&\quad \pm\Delta_1^{(t)}\sum_j \left(a_j a_{j+1} + \text{h.c.}\right).
\end{aligned}
\tag{7.8}
$$

The induced hopping integral and pairing potential are given by

$$
t_1 = \frac{\Gamma}{Z}\frac{\cos\tilde{a}}{\tilde{a}}e^{-1/\tilde{\xi}},
\tag{7.9}
$$

$$
\Delta_1^{(t)} = g\sin 2\theta\frac{\Gamma}{Z}\frac{\sin\tilde{a} - \tilde{a}\cos\tilde{a}}{\tilde{a}^2}e^{-1/\tilde{\xi}}.
\tag{7.10}
$$

From Eq. (7.4), the localization length for the MZMs in these Hamiltonians (valid in their topological phase) is thus

$$
\xi_{\text{wire}} = \frac{Z^{-1}t_{\text{int}} + t_1}{\Delta_1^{(t)}} = \frac{\tilde{v}_F^{(\pm)}}{2E_{\text{gap}}^{(\pm)}}
\tag{7.11}
$$

135

where the renormalized Fermi velocity and excitation gap are

$$\tilde{v}_F^{(\pm)} = 2\left(Z^{-1}t_{\text{int}} + t_1\right)\sqrt{1 - \frac{(\mu \mp B)^2}{4\left(t_{\text{int}} + Zt_1\right)^2}}\,, \tag{7.12}$$

$$E_{\text{gap}}^{(\pm)} = \Delta_1^{(t)}\sqrt{1 - \frac{(\mu \mp B)^2}{4\left(t_{\text{int}} + Zt_1\right)^2}}\,. \tag{7.13}$$

Note that the localization length is the same for the spin-up and -down sectors. From Eq. (7.11) we observe that if one ignores the renormalization of the Fermi velocity and uses instead its intrinsic value, $v_F^{(\pm)} = 2t_{\text{int}}[1 - (\mu \mp B)^2/4t_{\text{int}}^2]^{1/2}$, to estimate the localization length as $\xi = v_F^{(\pm)}/2E_{\text{gap}}^{(\pm)}$, the result would *overestimate* the true value by a factor of $v_F^{(\pm)}/\tilde{v}_F^{(\pm)} > 1$. If the coupling between the wire and the superconductor is weak (i.e. $\Gamma \ll \Delta_{SC}, t_{\text{int}}$), the velocity is only weakly renormalized and $\tilde{v}_F^{(\pm)} \approx v_F^{(\pm)}$. However, when Γ is comparable to Δ_{SC} or even t_{int}, the discrepancy between the renormalized and the bare Fermi velocity is huge. For large enough Γ and hence Z, the coherence length could be close to zero even though the induced triplet gap is small. Whether or not this strong velocity renormalization, leading to sharply-localized MZMs in the topological nanowire, is present in the experiment of Ref. [28] can only be determined empirically since the microscopic details about Γ are simply not known in the experimental system. What is clear, however, is that there is a well-defined physical mechanism, namely, a very strong tunnel-coupling between the superconductor and the nanowire, which would lead to a strong renormalization of the effective Fermi velocity and a concomitant suppression of the MZM localization length in the nanowire even if the induced topological gap is small. We note that the

existence of the strong renormalization effect has already been invoked for the Fe/Pb system by Peng *et al.* using a helical magnetic chain model for the nanowire [128].

7.3 Effects of non-local hopping and pairing

As we mentioned in the introduction, the substrate-induced enhancement of the Majorana localization length is accompanied by a power-law decay of the MZMs [24]. This power-law decay of the MZMs, if large, limits the validity of the enhanced exponential localization. To understand and estimate this effect we write the Hamiltonian in the large tunneling limit as

$$H = H_0 + \delta H \tag{7.14}$$

where H_0 is given in Eq. (7.8) and δH contains the hopping and pairing terms in Eq. (7.5) involving sites separated by two or more lattice spacings. Let ψ_0 denote the MZM that is localized at the end of the wire with a localization length given by Eq. (7.11). With the non-local perturbation $\delta H^{(\pm)}$ the state acquires a correction: $\psi_0 \to \tilde{\psi}_0 = \psi_0 + \delta\psi_0$ where

$$\delta\psi_0 = -\frac{1}{H_0}\mathcal{P}\delta H \left|\psi_0\right\rangle , \tag{7.15}$$

where $\mathcal{P} = 1 - \left|\psi_0\right\rangle\left\langle\psi_0\right|$. We can now qualitatively see the localization behavior of $\tilde{\psi}_0$ including the long-range self-energy correction: the unperturbed part $\psi_0 \sim e^{-x/\xi_{\text{wire}}}$ (where x is the distance measured from the boundary) is still localized with a length

ξ_{wire}, while the correction $\delta\psi_0$ has a long tail since δH scales as $\sim e^{-x/\xi}/x$ where ξ is the coherence length of the bulk superconductor. Therefore

$$\tilde{\psi}_0 \sim \alpha e^{-x/\xi_{\text{wire}}} + \beta \frac{e^{-x/\xi}}{k_F x}, \qquad (7.16)$$

where ψ_0 is approximated as $\alpha e^{-x/\xi_{\text{wire}}}$, α is a normalization constant, and β is a parameter determined from the perturbation theory. Strictly speaking, the localization length of $\tilde{\psi}_0$ is $\max\{\xi_{\text{wire}}, \xi\}$. However, the second term in Eq. (7.16) is now qualitatively similar to the wave-function of a Shiba state bound to magnetic impurities and appears in experiments to be localized on a scale of k_F^{-1} [130] instead of the true localization length ξ. In this case β is perturbatively small, further obscuring its signature in experiments. Thus the experimentally measured localization length would still be ξ_{wire} even with longer-range hopping in Eq. 7.5. Since for practical purposes the dominant localization length of the non-local part is essentially k_F^{-1} and is small, the non-local term δH can be safely ignored. We note, however, that independent of whether $\alpha \gg \beta$ or $\beta \gg \alpha$ in Eq. (7.16), the resultant Majorana wavefunction is strongly localized at the wire end $(x = 0)$ with either a strongly suppressed localization length ξ_{wire} or $1/k_F$, both of which are much smaller than the bare MZM localization length ξ without any substrate renormalization effect (provided, of course, one is in the strong tunnel coupling regime). In Ref. [116], Dumitrescu *et al.* recently took into account the second term in Eq. (7.16) as causing the suppressed MZM localization in ferromagnetic chain systems whereas Peng *et al.* [128] mostly considered the first term in discussing MZM localization in helical

magnetic chains. In principle, both terms could be important, but their qualitative effects are similar, both leading to a strongly suppressed MZM localization in the nanowire in the strong tunnel-coupled regime. But, the second term in Eq. (7.16), with its power law decay, may have implications for the non-Abelian braiding experiments, and may severely limit the usefulness of the resultant MZMs in carrying out topological quantum computation although for practical purposes the MZMs appear strongly spatially localized at the wire ends.

7.4   Relating quasi-1D models to 1D models

We have established above that as long as the nanowire is strongly tunnel-coupled to the superconductor (so that the condition $\Gamma > t_{\text{int}}, \Delta_{\text{SC}}$ applies), the MZM localization length would be strongly suppressed compared with the standard bare coherence length formula due to the Fermi velocity renormalization caused by the substrate. This renormalization effect appears to be independent of the nature of the nanowire and, therefore, should affect both ferromagnetic nanowires and SMC nanowires equally (as long as the tunnel coupling defined by Eq. (7.7) is large). We now show that this is not the case, and there is good reason to believe that the ferromagnetic chain system of Ref. [28] could be much more strongly renormalized by the substrate than the SMC nanowire systems [7, 52, 129, 51, 53, 54].

While we are assuming a strictly 1D limit for the nanowire, a more realistic model would treat the nanowire as quasi-1D and as a result the parameters such as t_s and t_p in the 1D model [for example, defining Γ in Eq. (7.7)] are really effective

parameters that have a strong dependence on the radius of the nanowire in a quasi-1D geometry. Since we are interested in understanding the scaling behavior with nanowire radius, we will assume a simple model of a 3D cylindrical lattice nanowire (with the wire transverse cross-sectional width being much smaller than the wire length). The 3D (i.e. quasi-1D) wave-functions and the strictly 1D wavefunctions $\psi_{wire,1D}$ are related by a transverse wavefunction factor as

$$\psi_{\text{wire},3D}\left(\rho, z, \phi\right) = \frac{a}{R} J_m \left(k_m \frac{\rho}{R+a}\right) e^{im\phi} \psi_{\text{wire},1D}\left(z\right) \tag{7.17}$$

where k_m is a zero of the Bessel function (J_m) so that the wave-function satisfies $\psi_{\text{wire},3D}(R + a, z, \phi) = 0$ and a is the lattice constant of the wire. Note that the boundary condition on the lattice is such that the wave-function at a distance a outside the wire vanishes. In the limit that $a \ll R$ the wave-function $\psi_{wire,3D}$ at the boundary is written as

$$\psi_{\text{wire},3D}\left(R, z, \phi\right) = \frac{a^2}{R^2} k_m J'_m\left(k_m\right) e^{im\phi} \sqrt{\frac{1}{\pi L}} \sin\left(\frac{n\pi z}{L}\right). \tag{7.18}$$

The 1D hopping matrix elements $t_{s,p}$ enter the formalism through the parameter Γ defined in Eq. 7.7. To simplify our analysis we split $\Gamma = \Gamma_s \cos\theta^2 + \Gamma_p \sin\theta^2$ where $\Gamma_s = \pi\nu t_s^2$ and $\Gamma_p = \pi\nu t_p^2$. The self-energy of these individual orbitals arise from microscopic 3D tunnelings $\tilde{t}_{s,p}$, which must be used together with the 3D density of states ν and the 3D wavefunction $\psi_{\text{wire},3D}\left(R, z, \phi\right)$. In addition, for the purpose of our estimate, we will make a simplifying assumption that the density of

states of the SC in the normal state ν is local at each site on the surface of the wire. With these assumptions, the 3D generalized form for $\Gamma_{s,p}$ is a similar form to Eq. 7.7, except for a sum over the surface of the wire. This sum can be approximated by an integral as

$$\Gamma_{s,p} = \int Ra^{-1}d\phi dz |\psi_{\text{wire,3D}}(R,z,\phi)|^2 \pi \tilde{t}_{s,p}^2 k_F a/E_F$$
$$= \kappa \pi \tilde{t}_s^2 k_F a^4/E_F R^3, \tag{7.19}$$

where κ is a dimensionless number resulting from the Bessel function. To obtain the above result we have used the lattice form for the LDOS in 3D $\nu \propto \pi a^3 k_F^3/E_F$. The hopping $\tilde{t}_{s,p}$, which is proportional to the bare hopping in the wire can be parametrized by a dimensionless parameter $\zeta_{s,p}$ and written as $\tilde{t}_{s,p} = \zeta_{s,p}\hbar^2/2m^*a^2$, where m^* is the effective mass. Using this parametrization we obtain the estimate for $\Gamma_{s,p}$ as

$$\Gamma_{s,p} = \kappa \zeta_{s,p}^2 \left(\frac{\lambda_F}{R}\right)^3 E_F. \tag{7.20}$$

Now we are in a position to compare the scale of Γ for the SMC nanowire and the ferromagnetic chain. Qualitatively speaking, on a ferromagnetic chain of atoms (as in Ref. [28]) where R is much smaller as compared with the SMC nanowire (as in Ref. [7]), Γ is expected to be much larger [note that the dependence on R is R^{-3} in Eq. (7.20)]. Quantitatively, assuming $R \sim \lambda_F$ would be of order $0.5\,\text{nm}$ for the ferromagnetic Fe chain in Ref. [28] we estimate $\Gamma \sim E_F \sim 1\text{eV}$ (if we ignore the factors of $\kappa \sim \zeta_{s,p} \sim 1$). On the other hand, for the same parameters for

the SMC nanowire except the mode confinement radius $R \sim 20$nm we expect the self-energy parameter Γ is of order 0.1meV in the SMC. This huge difference in Γ between the SMC nanowires used in [7] and the ferromagnetic chains used in [28] may explain why the MZM might be strongly localized (delocalized) in the ferromagnetic (SMC) nanowires even if both systems manifest the same induced superconducting gap ($\sim 100\,\mu$eV). This difference ultimately arises, keeping all the other parameters similar, from the difference in the transverse quantization size in the two 1D systems with the wire radius ratio being roughly a factor of 40 between the two, leading to a localization length difference which could in principle be as large as a factor of $40^3 \sim 64000$! In reality, this is an overestimate of the difference in the MZM localization in the two situations since the bare Fermi velocity in the SMC is typically a factor of 100 or so smaller than that in the ferromagnetic metallic chain, which leads to a factor of $64000/100 \sim 640$ difference in the MZM localization length between the SMC nanowire [7, 52, 129, 51, 53, 54] and the ferromagnetic wire [28] systems even if both systems have exactly the same induced superconducting gap ($\sim 0.1\,$meV). This roughly a factor of 500 difference is in quantitative agreement with the conclusion of Ref. 21 where the MZM localization length is inferred to be $< 1\,$nm whereas in the SMC nanowire case the MZM localization length is the same as the bare coherence length in the nanowire ($\sim 100\,$nm). Thus, the difference between MZM localization in the two systems arises entirely from the difference in the nanowire transverse confinement radius in SMC versus metals.

7.5 Conclusion

In summary, we have established that the nanowire-on-superconductor hybrid systems can potentially have very short Majorana localization length even when the induced topological superconducting gap is very small in the nanowire by virtue of the substrate-induced strong renormalization of the effective nanowire parameters (for example, the Fermi velocity and the gap) because of the strong frequency dependence of the relevant self-energy function determining the proximity-induced pair potential in the nanowire. We have shown that this renormalization goes as R^{-3}, where R is the effective nanowire confinement size in the transverse direction determining how 1D the system really is (with R going to zero limit being the true 1D nanowire limit). This provides an explanation for why the Majorana localization length could be very small in metallic nanowires on superconductors, while very large for the SMC nanowire: the metallic nanowire has $R \sim 0.5\,\mathrm{nm}$ while the SMC nanowire has $R \sim 20\,\mathrm{nm}$. The huge difference in the radii of the two systems leads to a large difference in the renormalization effect induced by the substrate. The substrate-induced suppression of the Majorana localization length may have implications for recent efforts [28] to observe localized MZMs in fairly short (1-10 nm) ferromagnetic Fe chains on superconducting Pb substrates using STM spectroscopy, providing a possible explanation [128] for how the MZM may be spatially highly localized on a sub-nm length scale near the ends of the Fe adatom chain in spite of a very small induced superconducting gap.

Chapter 8

Conclusion and Outlook

We now summarize our findings in this dissertation and discuss possible future directions.

In the first Chapter, we motivated the search for MZMs by demonstrating that they obey exotic braiding statistics. We reviewed some of the proposals for realizing such modes in chiral p-wave SCs, TI-based heterostructures, SMC-based heterostructures, and Shiba states.

In Chapter 2, we adapted the quasiclassical Eilenberger theory to analyze the effects of ensemble-averaged disorder on the MZMs at the ends of a chiral p-wave superconductor. The salient feature of our theory was that all short-length-scale fluctuations are retained, and the diffusive limit was not taken. We found that, within our formalism, the ZBP in the LDOS associated with MZMs still remain after the bulk gap is closed by disorder. This was attributed to the fact that Eilenberger theory could not handle localization physics.

In Chapter 3, we analyzed the effect of non-magnetic disorder on the MZMs induced at the SC/FI interface on a multi-channel 1D TI edge. We found that extra subgap states could be induced. We also analyzed the case where only a single channel is present, and found that in this case the robustness of the spectral gap

protecting the MZM is ensured by various symmetries in the system.

In Chapter 4, we investigated the issue of "soft gap" universally present in all experimental setups of the nanowire proposal. We looked into different positive causes (like magnetic scattering, thermal and dissipative broadening) and concluded that the most likely explanation was the interface fluctuations at the SMC-SC contact.

In Chapter 5-7, we considered a system with a chain of ferromagnetic atoms deposited on the surface of a SOC superconductor. This problem was addressed in two special limits. First, in Chapter 5, we assumed negligible inter-atomic hopping among the ferromagnetic atoms. The problem was then reduced to a chain of hybridized Shiba states on the surface of a Rashba-coupled 2D SC. The conditions for entering a topological phase was analytically derived, with a representative topological phase diagram computed. Then, in Chapter 6-7, we took the opposite limit where the inter-atomic hoppings among the ferromagnetic atoms are much larger than the hybridization energies between the induced Shiba states. In Chapter 6, with a two-orbital phenomenological model for the SOC SC, we demonstrated how the local inversion symmetry-breaking at its surface could induce SOC and triplet pairing terms in the ferromagnetic chain. The resultant topological phases for the effective Hamiltonian for the chain was discussed. Lastly, in Chapter 7, we emphasize that in the strong (chain-SC) coupling limit, a significant renormalization of length scales results in the chain. This was used to explain the observed extremely short localization length of MZMs in experiments [28] described by this model.

We now discuss possible future research directions. The experimental realiza-

tion of MZM is still at its primitive stage, and much experimental effort is required to improve the quality of experimental data. Our result can provide helpful guidance for such endeavors. For example, Ref. [131] has a setup with significantly improved SMC-SC interface resulting in a hard SC gap on the SMC. Theoretical analysis of their future experimental result with SOC and Zeeman terms put in to the wire is important. On the other hand for the Shiba-based proposal, a big problem is distinguishing between the MZMs and the Shiba states, both of which are zero-energy modes localized at the end of the chain [132]. A possible way for this is to utilized spin-polarized STM to probe for specific spinorial structure unique to MZMs.

List of Publications

Publications this thesis is based on:

1. Hoi-Yin Hui, Jay D. Sau and S. Das Sarma, *Generalized Eilenberger theory for Majorana zero-mode-carrying disordered p-wave superconductors*, Phys. Rev. B **90**, 064516 (2014)

2. Hoi-Yin Hui, Jay D. Sau and S. Das Sarma, *Disorder-induced subgap states and Majorana zero-energy edge modes in two-dimensional topological insulator-superconductor hybrid structures*, Phys. Rev. B **90**, 174206 (2014)

3. So Takei, Benjamin M. Fregoso, Hoi-Yin Hui, Alejandro M. Lobos, and S. Das Sarma, *Soft Superconducting Gap in Semiconductor Majorana Nanowires*, Phys. Rev. Lett. **110**, 186803 (2013)

4. P. M. R. Brydon, S. Das Sarma, Hoi-Yin Hui, and Jay D. Sau, *Topological Yu-Shiba-Rusinov chain from spin-orbit coupling*, Phys. Rev. B **91**, 064505 (2015)

5. Hoi-Yin Hui, P. M. R. Brydon, Jay D. Sau, S. Tewari, S. Das Sarma, *Majorana fermions in a ferromagnetic wire on the surface of a bulk spin-orbit coupled s-wave superconductor*, Sci. Rep. **5**, 8880 (2015)

6. S. Das Sarma, Hoi-Yin Hui, P. M. R. Brydon, and Jay D. Sau, *Substrate-induced Majorana renormalization in topological nanowires*, arXiv:1503.00594 (2015)

Other publications and preprints that I contributed to:

1. Hoi-Yin Hui, Alejandro M. Lobos, Jay D. Sau, and S. Das Sarma, *Proximity-induced superconductivity and Josephson critical current in quantum spin Hall systems*, Phys. Rev. B **90**, 224517 (2014)

2. P. M. R. Brydon, S. Das Sarma, Hoi-Yin Hui, and Jay D. Sau, *Odd-parity superconductivity from phonon-mediated pairing: Application to $Cu_xBi_2Se_3$*, Phys. Rev. B **90**, 184512 (2014)

3. F. Setiawan, Hoi-Yin Hui, J. P. Kestner, Xin Wang, and S. Das Sarma, *Robust two-qubit gates for exchange-coupled qubits*, Phys. Rev. B **89**, 085314 (2014)

4. Hoi-Yin Hui, Ryan Barnett, J. V. Porto, and S. Das Sarma, *Loop-structure stability of a double-well-lattice Bose-Einstein condensate*, Phys. Rev. A **86**, 063636 (2012)

5. Jay D. Sau, Chien Hung Lin, Hoi-Yin Hui, and S. Das Sarma, *Avoidance of Majorana Resonances in Periodic Topological Superconductor-Nanowire Structures*, Phys. Rev. Lett. **108**, 067001 (2012)

6. Hoi-Yin Hui, Ryan Barnett, Rajdeep Sensarma, and S. Das Sarma, *Instabilities of bosonic spin currents in optical lattices*, Phys. Rev. A **84**, 043615 (2011)

7. Ryan Barnett, Hoi-Yin Hui, Chien-Hung Lin, Jay D. Sau, and S. Das Sarma, *Quantum rotor theory of spinor condensates in tight traps*, Phys. Rev. A **83**, 023613 (2011)

Bibliography

[1] E. Fradkin, C. Nayak, A. Tsvelik, and F. Wilczek, Nucl. Phys. B **516**, 704 (1998).

[2] R. H. Morf, Phys. Rev. Lett. **80**, 1505 (1998).

[3] N. Read and D. Green, Phys. Rev. B **61**, 10267 (2000).

[4] A. Y. Kitaev, Phys. Usp. **44**, 131 (2001).

[5] R. M. Lutchyn, J. D. Sau, and S. Das Sarma, Phys. Rev. Lett. **105**, 077001 (2010).

[6] Y. Oreg, G. Refael, and F. von Oppen, Phys. Rev. Lett. **105**, 177002 (2010).

[7] V. Mourik *et al.*, Science **336**, 1003 (2012).

[8] E. Majorana, Nuovo Cimento **5**, 171 (1937).

[9] M. Leijnse and K. Flensberg, Semicond. Sci. Technol. **27**, 124003 (2012).

[10] J. Alicea, Rep. Prog. Phys. **75**, 076501 (2012).

[11] L. Fu and C. L. Kane, Phys. Rev. Lett. **100**, 096407 (2008).

[12] A. C. Potter and P. A. Lee, Phys. Rev. B **83**, 184520 (2011).

[13] J. D. Sau, S. Tewari, R. M. Lutchyn, T. D. Stanescu, and S. Das Sarma, Phys. Rev. B **82**, 214509 (2010).

[14] J. D. Sau, R. M. Lutchyn, S. Tewari, and S. Das Sarma, Phys. Rev. Lett. **104**, 040502 (2010).

[15] T.-P. Choy, J. M. Edge, A. R. Akhmerov, and C. W. J. Beenakker, Phys. Rev. B **84**, 195442 (2011).

[16] M. Kjaergaard, K. Wölms, and K. Flensberg, Phys. Rev. B **85**, 020503 (2012).

[17] L. Yu, Acta Phys. Sin. **21**, 75 (1965).

[18] H. Shiba, Prog. Theor. Phys. **40**, 435 (1968).

[19] A. I. Rusinov, Eksp. Teor. Fiz. Pisma. Red. **9**, 146 (1968), [JETP Lett. 9, 85 (1969)].

[20] S. Nadj-Perge, I. K. Drozdov, B. A. Bernevig, and A. Yazdani, Phys. Rev. B **88**, 020407 (2013).

[21] J. Klinovaja, P. Stano, A. Yazdani, and D. Loss, Phys. Rev. Lett. **111**, 186805 (2013).

[22] B. Braunecker and P. Simon, Phys. Rev. Lett. **111**, 147202 (2013).

[23] M. M. Vazifeh and M. Franz, Phys. Rev. Lett. **111**, 206802 (2013).

[24] F. Pientka, L. I. Glazman, and F. von Oppen, Phys. Rev. B **88**, 155420 (2013).

[25] F. Pientka, L. I. Glazman, and F. von Oppen, Phys. Rev. B **89**, 180505 (2014).

[26] Y. Kim, M. Cheng, B. Bauer, R. M. Lutchyn, and S. Das Sarma, Phys. Rev. B **90**, 060401 (2014).

[27] P. M. R. Brydon, S. Das Sarma, H.-Y. Hui, and J. D. Sau, Phys. Rev. B **91**, 064505 (2015).

[28] S. Nadj-Perge *et al.*, Science **346**, 602 (2014).

[29] J. D. Sau and S. Das Sarma, Nat. Commun. **3**, 964 (2012).

[30] I. C. Fulga, A. Haim, A. R. Akhmerov, and Y. Oreg, New J. Phys. **15**, 045020 (2013).

[31] I. Martin and A. F. Morpurgo, Phys. Rev. B **85**, 144505 (2012).

[32] J. Klinovaja, P. Stano, and D. Loss, Phys. Rev. Lett. **109**, 236801 (2012).

[33] S. Nakosai, Y. Tanaka, and N. Nagaosa, Phys. Rev. B **88**, 180503 (2013).

[34] C. W. J. Beenakker, Phys. Rev. Lett. **67**, 3836 (1991).

[35] J. D. Sau, E. Berg, and B. I. Halperin, arXiv:1206.4596 (2012).

[36] K. T. Law, P. A. Lee, and T. K. Ng, Phys. Rev. Lett. **103**, 237001 (2009).

[37] S. Kashiwaya, Y. Tanaka, M. Koyanagi, and K. Kajimura, Phys. Rev. B **53**, 2667 (1996).

[38] K. Sengupta, I. Žutić, H.-J. Kwon, V. M. Yakovenko, and S. Das Sarma, Phys. Rev. B **63**, 144531 (2001).

[39] C. J. Bolech and E. Demler, Phys. Rev. Lett. **98**, 237002 (2007).

[40] J. Nilsson, A. R. Akhmerov, and C. W. J. Beenakker, Phys. Rev. Lett. **101**, 120403 (2008).

[41] K. Flensberg, Phys. Rev. B **82**, 180516 (2010).

[42] M. Wimmer, A. R. Akhmerov, J. P. Dahlhaus, and C. W. J. Beenakker, New J. Phys. **13**, 053016 (2011).

[43] L. Fidkowski, J. Alicea, N. H. Lindner, R. M. Lutchyn, and M. P. A. Fisher, Phys. Rev. B **85**, 245121 (2012).

[44] D. I. Pikulin, J. P. Dahlhaus, M. Wimmer, H. Schomerus, and C. W. J. Beenakker, New J. Phys. **14**, 125011 (2012).

[45] J. D. Sau and S. Das Sarma, Phys. Rev. B **88**, 064506 (2013).

[46] J. Liu, A. C. Potter, K. T. Law, and P. A. Lee, Phys. Rev. Lett. **109**, 267002 (2012).

[47] F. Pientka, G. Kells, A. Romito, P. W. Brouwer, and F. von Oppen, Phys. Rev. Lett. **109**, 227006 (2012).

[48] P. Neven, D. Bagrets, and A. Altland, New J. Phys. **15**, 055019 (2013).

[49] P. W. Brouwer, M. Duckheim, A. Romito, and F. von Oppen, Phys. Rev. B **84**, 144526 (2011).

[50] I. Adagideli, M. Wimmer, and A. Teker, Phys. Rev. B **89**, 144506 (2014).

[51] A. Das *et al.*, Nat. Phys. **8**, 887 (2012).

[52] M. T. Deng *et al.*, Nano Lett. **12**, 6414 (2012).

[53] H. O. H. Churchill *et al.*, Phys. Rev. B **87**, 241401 (2013).

[54] A. D. K. Finck, D. J. Van Harlingen, P. K. Mohseni, K. Jung, and X. Li, Phys. Rev. Lett. **110**, 126406 (2013).

[55] T. D. Stanescu, R. M. Lutchyn, and S. Das Sarma, Phys. Rev. B **90**, 085302 (2014).

[56] H.-Y. Hui, J. D. Sau, and S. Das Sarma, Phys. Rev. B **90**, 064516 (2014).

[57] H.-Y. Hui, J. D. Sau, and S. Das Sarma, Phys. Rev. B **90**, 174206 (2014).

[58] S. Takei, B. M. Fregoso, H.-Y. Hui, A. M. Lobos, and S. Das Sarma, Phys. Rev. Lett. **110**, 186803 (2013).

[59] H.-Y. Hui, P. M. R. Brydon, J. D. Sau, S. Tewari, and S. Das Sarma, Sci. Rep. **5**, 8880 (2015).

[60] S. Das Sarma, H.-Y. Hui, P. M. R. Brydon, and J. D. Sau, arXiv:1503.00594 (2015).

[61] O. Motrunich, K. Damle, and D. A. Huse, Phys. Rev. B **63**, 224204 (2001).

[62] A. R. Akhmerov, J. P. Dahlhaus, F. Hassler, M. Wimmer, and C. W. J. Beenakker, Phys. Rev. Lett. **106**, 057001 (2011).

[63] D. Bagrets and A. Altland, Phys. Rev. Lett. **109**, 227005 (2012).

[64] P. W. Brouwer, M. Duckheim, A. Romito, and F. von Oppen, Phys. Rev. Lett. **107**, 196804 (2011).

[65] A. M. Lobos, R. M. Lutchyn, and S. Das Sarma, Phys. Rev. Lett. **109**, 146403 (2012).

[66] J. D. Sau, S. Tewari, and S. Das Sarma, Phys. Rev. B **85**, 064512 (2012).

[67] W. DeGottardi, M. Thakurathi, S. Vishveshwara, and D. Sen, Phys. Rev. B **88**, 165111 (2013).

[68] D. Rainis, L. Trifunovic, J. Klinovaja, and D. Loss, Phys. Rev. B **87**, 024515 (2013).

[69] G. Eilenberger, Z. Phys. **214**, 195 (1968).

[70] K. D. Usadel, Phys. Rev. Lett. **25**, 507 (1970).

[71] L. Fu and C. L. Kane, Phys. Rev. B **79**, 161408 (2009).

[72] J. D. Sau, R. M. Lutchyn, S. Tewari, and S. Das Sarma, Phys. Rev. B **82**, 094522 (2010).

[73] V. Stanev and V. Galitski, Phys. Rev. B **89**, 174521 (2014).

[74] A. V. Zaitsev, Zh. Eksp. Teor. Fiz **86**, 1742 (1984).

[75] R. D. Parks, *Superconductivity* (Marcel Dekker, 1969).

[76] Y. Tanaka and A. A. Golubov, Phys. Rev. Lett. **98**, 037003 (2007).

[77] Y. Asano and Y. Tanaka, Phys. Rev. B **87**, 104513 (2013).

[78] L. Fu and C. L. Kane, Phys. Rev. Lett. **102**, 216403 (2009).

[79] P. Anderson, J. Phys. Chem. Solids **11**, 26 (1959).

[80] G. Tkachov, Phys. Rev. B **87**, 245422 (2013).

[81] J. I. Väyrynen, M. Goldstein, and L. I. Glazman, Phys. Rev. Lett. **110**, 216402 (2013).

[82] M. Bianchi *et al.*, Nat. Commun. **1**, 128 (2010).

[83] M. S. Bahramy *et al.*, Nat. Commun. **3**, 1159 (2012).

[84] B. A. Bernevig, T. L. Hughes, and S.-C. Zhang, Science **314**, 1757 (2006).

[85] M. König *et al.*, Science **318**, 766 (2007).

[86] C. Kittel, *Introduction to Solid State Physics*, 8 ed. (John Wiley and Sons, New York, 2005).

[87] P. G. de Gennes, *Superconductivty of Metals and Alloys* (Addison-Wesley, Reading MA, 1989).

[88] F. Gygi and M. Schluter, Phys. Rev. B **41**, 822 (1990).

[89] D. A. Ivanov, J. Math. Phys. **43**, 126 (2002).

[90] P. A. Ioselevich, P. M. Ostrovsky, and M. V. Feigel'man, Phys. Rev. B **86**, 035441 (2012).

[91] A. R. Akhmerov, Phys. Rev. B **82**, 020509 (2010).

[92] K. Flensberg, Phys. Rev. Lett. **106**, 090503 (2011).

[93] C. W. J. Beenakker, Rev. Mod. Phys. **69**, 731 (1997).

[94] Y. Takane, J. Phys. Soc. Jpn. **73**, 2366 (2004).

[95] A. A. Abrikosov and L. P. Gor'kov, Zh. Eksp. Teor. Fiz. **39**, 1781 (1960).

[96] T. D. Stanescu, R. M. Lutchyn, and S. Das Sarma, Phys. Rev. B **84**, 144522 (2011).

[97] A. V. Balatsky, I. Vekhter, and J.-X. Zhu, Rev. Mod. Phys. **78**, 373 (2006).

[98] W. L. McMillan, Phys. Rev. **175**, 537 (1968).

[99] B. A. Aminov, A. A. Golubov, and M. Y. Kupriyanov, Phys. Rev. B **53**, 365 (1996).

[100] G. E. Blonder, M. Tinkham, and T. M. Klapwijk, Phys. Rev. B **25**, 4515 (1982).

[101] K. Neurohr *et al.*, Phys. Rev. B **54**, 17018 (1996).

[102] A. F. Volkov, A. V. Zaitsev, and T. M. Klapwijk, Physica C **210**, 21 (1993).

[103] W. M. van Huffelen, T. M. Klapwijk, D. R. Heslinga, M. J. de Boer, and N. van der Post, Phys. Rev. B **47**, 5170 (1993).

[104] W. Chang, V. E. Manucharyan, T. S. Jespersen, J. Nygård, and C. M. Marcus, Phys. Rev. Lett. **110**, 217005 (2013).

[105] Y. Meir and N. S. Wingreen, Phys. Rev. Lett. **68**, 2512 (1992).

[106] G. D. Mahan, *Many-Particle Physics* (Kluwer Academic/Plenum, New York, 2000).

[107] R. C. Dynes, V. Narayanamurti, and J. P. Garno, Phys. Rev. Lett. **41**, 1509 (1978).

[108] A. Kastalsky *et al.*, Phys. Rev. Lett. **67**, 3026 (1991).

[109] S. Guéron, H. Pothier, N. O. Birge, D. Esteve, and M. H. Devoret, Phys. Rev. Lett. **77**, 3025 (1996).

[110] E. F. C. Driessen, P. C. J. J. Coumou, R. R. Tromp, P. J. de Visser, and T. M. Klapwijk, Phys. Rev. Lett. **109**, 107003 (2012).

[111] K. Pöyhönen, A. Weststrom, J. Röntynen, and T. Ojanen, Phys. Rev. B **89**, 115109 (2014).

[112] I. Reis, D. J. J. Marchand, and M. Franz, Phys. Rev. B **90**, 085124 (2014).

[113] J. Röntynen and T. Ojanen, Phys. Rev. B **90**, 180503 (2014).

[114] P. Kotetes, New J. Phys. **15**, 105027 (2013).

[115] J. Li *et al.*, Phys. Rev. B **90**, 235433 (2014).

[116] E. Dumitrescu, B. Roberts, S. Tewari, J. D. Sau, and S. Das Sarma, Phys. Rev. B **91**, 094505 (2015).

[117] L. P. Gor'kov and E. I. Rashba, Phys. Rev. Lett. **87**, 037004 (2001).

[118] A. P. Schnyder, S. Ryu, A. Furusaki, and A. W. W. Ludwig, Phys. Rev. B **78**, 195125 (2008).

[119] A. Schnyder, S. Ryu, A. Furusaki, and A. Ludwig, AIP Conf. Proc. **1134**, 10 (2009).

[120] A. Kitaev, Periodic table for topological insulators and superconductors, in *AIP Conf. Proc.* Vol. 1134, 2009.

[121] S. Ryu, A. P. Schnyder, A. Furusaki, and A. W. W. Ludwig, New J. Phys. **12**, 065010 (2010).

[122] S. Das Sarma, J. D. Sau, and T. D. Stanescu, Phys. Rev. B **86**, 220506 (2012).

[123] R. M. Lutchyn, T. D. Stanescu, and S. Das Sarma, Phys. Rev. Lett. **106**, 127001 (2011).

[124] A. C. Potter and P. A. Lee, Phys. Rev. Lett. **105**, 227003 (2010).

[125] S. B. Chung, H.-J. Zhang, X.-L. Qi, and S.-C. Zhang, Phys. Rev. B **84**, 060510 (2011).

[126] M. Duckheim and P. W. Brouwer, Phys. Rev. B **83**, 054513 (2011).

[127] E. Dumitrescu and S. Tewari, Phys. Rev. B **88**, 220505 (2013).

[128] Y. Peng, F. Pientka, L. I. Glazman, and F. von Oppen, arXiv:1412.0151 (2014).

[129] L. P. Rokhinson, X. Liu, and J. K. Furdyna, Nat. Phys. **8**, 795 (2012).

[130] A. Yazdani, B. A. Jones, C. P. Lutz, M. F. Crommie, and D. M. Eigler, Science **275**, 1767 (1997).

[131] W. Chang *et al.*, Nat. Nanotech. **10**, 232 (2015).

[132] J. D. Sau and P. M. R. Brydon, arXiv:1501.03149 (2015).